

Measurement of the CKM angle γ using $B_s^0 \rightarrow D_s K \pi\pi$ decays

P. d'Argent¹, E. Gersabeck², M. Kecke¹, M. Schiller³

¹*Physikalisches Institut, Ruprecht-Karls-Universität Heidelberg, Heidelberg, Germany*

²*School of Physics and Astronomy, University of Manchester, Manchester, United Kingdom*

³*School of Physics and Astronomy, University of Glasgow, Glasgow, United Kingdom*

Abstract

We present the first measurement of the weak phase $\gamma - 2\beta_s$ obtained from a time-dependent (amplitude) analysis of $B_s^0 \rightarrow D_s K \pi\pi$ decays using proton-proton collision data corresponding to an integrated luminosity of 7 fb^{-1} recorded by the LHCb detector.

Change-log

- Version 1.0: First note draft circulated to the WG
- Version 2.0: Implemented first round of comments from Mark, Alessandro, Agnieszka
 - Minor text changes throughout the note
 - Changed D^0 bkg vetoes (Sec. 3.2.2)
 - Revisited some systematics
 - * Use uncertainty from fake rate instead of fixing misID yield to 0 or twice the value (Sec. 11.2)
 - * Use GLASS model instead of RBW as alternative to LASS model for $K\pi$ S-wave (Sec. 11.9)
 - * Instead of assuming pure phase space, recalculate running width of three-body resonances taking only the dominant $K\pi\pi$ decay mode into account (Sec. 11.9)
 - * Calculate RMS of lineshape variations instead of summing them up in quadrature (Sec. 11.9)
 - * Bug fix in evaluation of fixed lineshape parameters (mass, width, form-factor) systematic (Sec. 11.9)
 - Added tables with alternative amplitude models (Sec. 11.10)
 - Added comparison plots of 16 vs 17 data (Sec. I.2)

Contents

1	Introduction	1
2	Formalism	2
2.1	Decay rates and CP -observables	2
2.2	Amplitude model	4
2.2.1	Form Factors and Resonance Lineshapes	4
2.2.2	Spin Densities	6
2.3	Fit implementation	8
2.4	Validation	9
3	Data samples and event selection	12
3.1	Stripping and Trigger selection	12
3.2	Offline selection	12
3.2.1	Phase space region	13
3.2.2	Physics background vetoes	14
3.2.3	Training of multivariate classifier	17
3.2.4	Final selection	19
3.3	Simulation	22
4	Yields determination	23
4.1	Signal model	23
4.2	Background models	24
4.3	Results	25
5	Decay-time Resolution	27
5.1	Calibration for Run-I data	28
5.2	Calibration for Run-II data	29
6	Acceptance	32
6.1	MC corrections	32
6.1.1	Truth matching of simulated candidates	32
6.1.2	Correction of data-simulation differences	32
6.2	Decay-time acceptance	33
6.3	Phase space acceptance	38
7	Flavour Tagging	41
7.1	OS tagger combination	41
7.2	Tagging performance	43
8	Production and Detection Asymmetries	45
8.1	B_s Production Asymmetry	45
8.2	$K^-\pi^+$ Detection Asymmetry	46
9	Decay-time fit	49
9.1	Fit to $B_s^0 \rightarrow D_s\pi\pi\pi$ data	49
9.2	Fit to $B_s^0 \rightarrow D_sK\pi\pi$ data	50

10 Time-dependent amplitude fit	52
10.1 Signal Model Construction	52
10.2 Results	55
11 Systematic uncertainties	58
11.1 Fit bias	58
11.2 Background subtraction	58
11.3 Decay-time acceptance	59
11.4 Decay-time resolution and tagging	59
11.5 Production, detection asymmetries and mixing frequency	60
11.6 Multiple candidates	60
11.7 Length and momentum scales	60
11.8 Phase space acceptance	61
11.9 Resonance description	61
11.10 Alternative amplitude models	62
A Stripping and Trigger cuts	68
B Details of multivariate classifier	70
C Detailed mass fits	74
D Decay-time Resolution fits	78
E Comparison of time-acceptance in subsamples	81
F Spin Amplitudes	82
G Considered Decay Chains	83
H Data-simulation comparisson	84
I Data distributions	85
I.1 Comparison of signal and calibration channels	85
I.2 Comparison of data taken in 2016 and 2017	86
I.3 Comparison of Run-I and Run-II data	87
I.4 Comparison of D_s final states	87
I.5 Comparison of trigger categories	88
References	89

1 Introduction

This note presents the first measurement of the CKM angle $\gamma \equiv \arg[-(V_{ud}V_{ub}^*)/(V_{cd}V_{cb}^*)]$ using $B_s^0 \rightarrow D_s K\pi\pi$ decays, where the $K\pi\pi$ subsystem is dominated by excited kaon states such as the $K_1(1270)$ and $K_1(1400)$ resonances [1, 2]. In these decays, sensitivity to the weak phase results from the interference between $b \rightarrow c$ and $b \rightarrow u$ transitions achieved through $B_s^0 - \bar{B}_s^0$ mixing [3, 4]. The amplitudes for both processes are of the same order in the Wolfenstein parameters λ , $\mathcal{O}(\lambda^3)$, so that interference effects are expected to be large. The corresponding Feynman diagrams are shown in Fig. 1.1. Due to the interference between mixing and decay amplitudes, the physical CP violating observables in these decays are functions of a combination of γ and the mixing phase β_s , namely $\gamma - 2\beta_s$. To account for the non-constant strong phase across the phase space, one can either perform a time-dependent amplitude fit or select a suitable phase-space region and introduce a coherence factor as additional hadronic parameter to the decay-time fit. The topologically very similar yet flavour specific decay $B_s \rightarrow D_s \pi\pi\pi$ is used as calibration channel, not only to calibrate the tagging algorithms and determine the decay-time acceptance but also to constrain the $B_s^0 - \bar{B}_s^0$ mixing frequency. The branching ration of these decay modes was measured by LHCb to be $\frac{\mathcal{B}(B_s^0 \rightarrow D_s K\pi\pi)}{\mathcal{B}(B_s^0 \rightarrow D_s \pi\pi\pi)} = 0.052 \pm 0.005(\text{stat}) \pm 0.003(\text{syst})$ [1, 2].

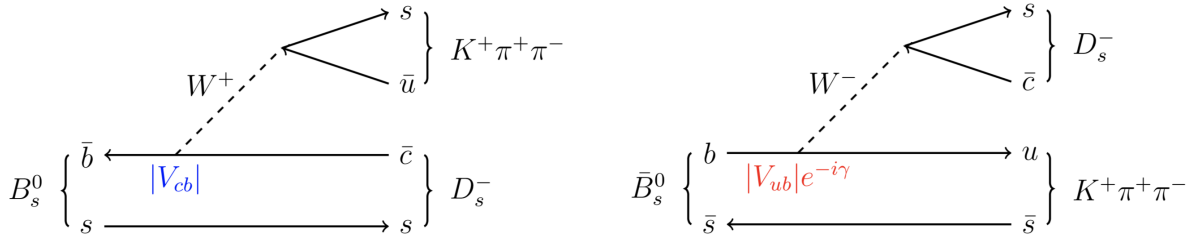


Figure 1.1: Feynman diagram for $B_s^0/\bar{B}_s^0 \rightarrow D_s^- K^+ \pi^+ \pi^-$ decays.

18 2 Formalism

19 2.1 Decay rates and *CP*-observables

20 The differential decay rate of B_s^0 or \bar{B}_s^0 decays to the final state $D_s^- K^+ \pi\pi$ or $D_s^+ K^- \pi\pi$ is
 21 given by:

$$\frac{d\Gamma(\mathbf{x}, t, q, f)}{e^{-\Gamma_s t} dt d\Phi_4} \propto (|\mathcal{A}_f^c(\mathbf{x})|^2 + |\mathcal{A}_f^u(\mathbf{x})|^2) \cosh\left(\frac{\Delta\Gamma_s t}{2}\right) \\ + q f (|\mathcal{A}_f^c(\mathbf{x})|^2 - |\mathcal{A}_f^u(\mathbf{x})|^2) \cos(\Delta m_s t) \\ - 2\text{Re}(\mathcal{A}_f^c(\mathbf{x})^* \mathcal{A}_f^u(\mathbf{x}) e^{-if(\gamma-2\beta_s)}) \sinh\left(\frac{\Delta\Gamma_s t}{2}\right) \\ - 2q f \text{Im}(\mathcal{A}_f^c(\mathbf{x})^* \mathcal{A}_f^u(\mathbf{x}) e^{-if(\gamma-2\beta_s)}) \sin(\Delta m_s t) \quad (2.1)$$

22 where $q = +1$ (-1) refers to an initially produced B_s^0 (\bar{B}_s^0) flavour eigenstate, $q = 0$ to an
 23 undetermined initial flavour, $f = +1$ or -1 denotes $D_s^- K^+ \pi\pi$ or $D_s^+ K^- \pi\pi$ final states and
 24 Γ_s , $\Delta\Gamma_s$ and Δm_s are the width average, the width difference and the mass difference of
 25 the two B_s mass eigenstates. We choose a convention in which $\Delta\Gamma_s < 0$ and $\Delta m_s > 0$.
 26 We further assume $|q/p| = 1$ for the complex coefficients p and q which relate the B_s
 27 meson mass eigenstates to the flavour eigenstates (no *CP* violation in the mixing). The
 28 CKM angle γ can be extracted from the *CP* violating phase associated to the interference
 29 between mixing and decay, $\gamma - 2\beta_s$, since the $B_s^0 - \bar{B}_s^0$ mixing phase, β_s , is well constrained
 30 from $B_s \rightarrow J/\psi \phi$ and related modes.

31 The static total decay amplitudes $\mathcal{A}_f^c(\mathbf{x})$ and $\mathcal{A}_f^u(\mathbf{x})$ are given by the coherent sum
 32 over all intermediate state amplitudes $A_i(\mathbf{x})$, each weighted by a complex coefficient to be
 33 determined from data,

$$\mathcal{A}(B_s^0 \rightarrow D_s^- K^+ \pi\pi) \equiv \mathcal{A}_f^c(\mathbf{x}) = \sum_i a_i^c A_i(\mathbf{x}) \quad (2.2)$$

$$\mathcal{A}(\bar{B}_s^0 \rightarrow D_s^- K^+ \pi\pi) \equiv \mathcal{A}_f^u(\mathbf{x}) = \sum_i a_i^u A_i(\mathbf{x}) \quad (2.3)$$

34 where the superscript c (u) indicates a $b \rightarrow c$ ($b \rightarrow u$) quark-level transition and \mathbf{x}
 35 represents a unique set of kinematic conditions within the five-dimensional phase space
 36 of the decay. Convenient choices for the kinematic observables include the invariant
 37 mass combinations of the final state particles or acoplanarity and helicity angles. In
 38 practice, we do not need to choose a particular five-dimensional basis, but use the full
 39 four-vectors of the decay in our analysis. The dimensionality is handled by the phase
 40 space element which can be written in terms of any set of five independent kinematic
 41 observables, $\mathbf{x} = (x_1, \dots, x_5)$, as

$$d\Phi_4 = \phi_4(\mathbf{x}) d^5 x, \quad (2.4)$$

42 where $\phi_4(\mathbf{x}) = \left| \frac{\partial\Phi_4}{\partial(x_1, \dots, x_5)} \right|$ is the phase space density. In contrast to three-body decays,
 43 the four-body phase space density function is not flat in the usual kinematic variables.
 44 Therefore, an analytic expression for ϕ_4 is taken from Ref. [5].

⁴⁵ Assuming there is no direct CP violation in the B_s decay implies for the CP conjugate
⁴⁶ transition amplitudes:

$$\mathcal{A}(\bar{B}_s^0 \rightarrow \bar{f}) = \mathcal{A}_f^c(\mathbf{x}) = \mathcal{A}_f^c(\bar{\mathbf{x}}) \quad (2.5)$$

$$\mathcal{A}(B_s^0 \rightarrow \bar{f}) = \mathcal{A}_f^u(\mathbf{x}) = \mathcal{A}_f^u(\bar{\mathbf{x}}) \quad (2.6)$$

⁴⁷ where the CP -conjugate phase space point $\bar{\mathbf{x}}$ is defined such that it is mapped onto \mathbf{x} by
⁴⁸ the interchange of final state charges, and the reversal of three-momenta.

⁴⁹ The phenomenological description of the intermediate state amplitudes is discussed
⁵⁰ in Sec. 2.2. For a model-independent measurement, the differential decay rate can be
⁵¹ integrated over the phase space:

$$\int \frac{d\Gamma(x, t, q, f)}{e^{-\Gamma_s t} dt d\Phi_4} d\Phi_4 \propto \cosh\left(\frac{\Delta\Gamma_s t}{2}\right) + q f C \cos(\Delta m_s t) \\ + D_f \sinh\left(\frac{\Delta\Gamma_s t}{2}\right) - q S_f \sin(\Delta m_s t) \quad (2.7)$$

⁵² where the same convention for the CP coefficients as for the $B_s \rightarrow D_s K$ analysis is used:

$$C = \frac{1 - r^2}{1 + r^2} \quad (2.8)$$

$$D_f = -\frac{2 r \kappa \cos(\delta - q_f (\gamma - 2\beta_s))}{1 + r^2} \quad (2.9)$$

$$S_f = f \frac{2 r \kappa \sin(\delta - q_f (\gamma - 2\beta_s))}{1 + r^2} \quad (2.10)$$

⁵³ The coherence factor κ , the strong phase difference δ and the ratio of the suppressed
⁵⁴ ($b \rightarrow u$) over favored ($b \rightarrow c$) decay mode, averaged over the phase space, are defined as:

$$\kappa e^{i\delta} \equiv \frac{\int \mathcal{A}_f^c(x)^* \mathcal{A}_f^u(x) d\Phi_4}{\sqrt{\int |\mathcal{A}_f^c(x)|^2 d\Phi_4} \sqrt{\int |\mathcal{A}_f^u(x)|^2 d\Phi_4}} \quad (2.11)$$

$$r \equiv \frac{\sqrt{\int |\mathcal{A}_f^u(x)|^2 d\Phi_4}}{\sqrt{\int |\mathcal{A}_f^c(x)|^2 d\Phi_4}}. \quad (2.12)$$

⁵⁵ The coherence factor dilutes the sensitivity to the weak phase γ due to the integration
⁵⁶ over the interfering amplitudes across the phase space. The value of κ is bounded between
⁵⁷ zero and unity. The latter corresponds to the limit of only one contributing intermediate
⁵⁸ state in which case the same sensitivity as in $B_s \rightarrow D_s K$ decays is reached, while $\kappa = 0$
⁵⁹ would result in no sensitivity to γ at all.

60 2.2 Amplitude model

61 To construct the intermediate state amplitudes $A_i(\mathbf{x})$, the isobar approach is used, which
 62 assumes that the decay process can be factorized into subsequent two-body decay am-
 63 plitudes [6–8]. This gives rise to two different decay topologies; quasi two-body decays
 64 $B_s \rightarrow (R_1 \rightarrow h_1 h_2) (R_2 \rightarrow h_3 h_4)$ or cascade decays $B_s \rightarrow h_1 [R_1 \rightarrow h_2 (R_2 \rightarrow h_3 h_4)]$. In
 65 either case, the intermediate state amplitude is parameterized as a product of orbital
 66 angular momentum, L , dependent form factors B_L , included for each vertex of the decay
 67 tree, Breit-Wigner propagators T_R , included for each resonance R , and an overall angular
 68 distribution represented by a spin factor S ,

$$A_i(\mathbf{x}) = B_{L_{B_s}}(\mathbf{x}) [B_{L_{R_1}}(\mathbf{x}) T_{R_1}(\mathbf{x})] [B_{L_{R_2}}(\mathbf{x}) T_{R_2}(\mathbf{x})] S_i(\mathbf{x}). \quad (2.13)$$

69 The following description of the individual components is adapted from Ref. [9] and
 70 only included for completeness.

71 2.2.1 Form Factors and Resonance Lineshapes

72 To account for the finite size of the decaying resonances, the Blatt-Weisskopf penetration
 73 factors, derived in Ref. [10] by assuming a square well interaction potential with radius
 74 r_{BW} , are used as form factors, B_L . They depend on the breakup momentum q , which is
 75 defined as the magnitude of the three-momentum of one of the daughters in the rest frame
 76 of the decaying resonance and the orbital angular momentum L , between the resonance
 77 daughters. Their explicit expressions are

$$\begin{aligned} B_0(q) &= 1, \\ B_1(q) &= 1/\sqrt{1 + (q r_{\text{BW}})^2}, \\ B_2(q) &= 1/\sqrt{9 + 3 (q r_{\text{BW}})^2 + (q r_{\text{BW}})^4}. \end{aligned} \quad (2.14)$$

78 Resonance lineshapes are described as function of the energy-squared, s , by Breit-Wigner
 79 propagators

$$T(s) = \frac{1}{m_0^2 - s - i m_0 \Gamma(s)}, \quad (2.15)$$

80 where the total width, $\Gamma(s)$, is normalized to give the nominal width, Γ_0 , when evaluated
 81 at the nominal mass m_0 .

82 For a decay into two stable particles $R \rightarrow AB$, the energy dependence of the decay
 83 width can be described by

$$\Gamma_{R \rightarrow AB}^{(2)}(s) = \Gamma_0 \frac{m_0}{\sqrt{s}} \left(\frac{q}{q_0} \right)^{2L+1} \frac{B_L(q)^2}{B_L(q_0)^2}, \quad (2.16)$$

84 where q_0 is the value of the breakup momentum at the resonance pole [11].

85 The energy-dependent width for a three-body decay $R \rightarrow ABC$, on the other hand, is
 86 considerably more complicated and has no analytic expression in general. However, it can
 87 be obtained numerically by integrating the transition amplitude-squared over the phase
 88 space,

$$\Gamma_{R \rightarrow ABC}^{(3)}(s) = \frac{1}{2\sqrt{s}} \int |A_{R \rightarrow ABC}|^2 d\Phi_3, \quad (2.17)$$

and therefore requires knowledge of the resonant substructure. The three-body amplitude $A_{R \rightarrow ABC}$ can be parameterized similarly to the four-body amplitude in Eq. (2.13). In particular, it includes form factors and propagators of intermediate two-body resonances.

Both Eq. (2.16) and Eq. (2.17) give only the partial width for the decay into a specific channel. To obtain the total width, a sum over all possible decay channels has to be performed,

$$\Gamma(s) = \sum_i g_i \Gamma_i(s), \quad (2.18)$$

where the coupling strength to channel i , is given by g_i .

The treatment of the lineshape for various resonances considered in this analysis is described in what follows. The nominal masses and widths of the resonances are taken from the PDG [12] with the exceptions described below.

For the broad scalar resonance σ , the model from Bugg is used [13]. We use the Gounaris-Sakurai parametrization for the $\rho(770)^0 \rightarrow \pi\pi$ propagator [14]. For the decay chain $K_1(1270) \rightarrow \rho(770)K$, we include $\rho-\omega$ mixing with the relative magnitude and phase between ρ and ω fixed to the values determined in Ref. [15]. The energy-dependent width of the $f_0(980)$ resonance is given by the sum of the partial widths into the $\pi\pi$ and KK channels (*i.e.* the Flatté lineshape [16]), where the coupling constants as well as the mass and width are taken from a measurement performed by the BES Collaboration [17]. For the $f_2(1270)$ and the $f_0(1370)$ mesons we use the total decay widths calculated in Ref. [9] which take the channels $\pi\pi$, KK , $\eta\eta$ and $\pi\pi\pi\pi$ into account. The Lass parameterization is used to model the $K\pi$ S -wave contribution. It consists of the $K_0^*(1430)$ resonance together with an effective range non-resonant component [18–20]:

$$T_{Lass}(s) = \frac{\sqrt{s}}{q \cot \delta_L - iq} + e^{2i\delta_L} \frac{m_0 \Gamma_0 \frac{m_0}{q_0}}{m_0^2 - s - i m_0 \Gamma_0 \frac{m_0}{\sqrt{s}} \frac{q}{q_0}} \quad (2.19)$$

with $\cot \delta_L = \frac{1}{aq} + \frac{1}{2}rq$. We use the values for the scattering length a and effective range parameter r from Ref. [18, 19]. Equation (2.16) is used for all other resonances decaying into a two-body final state.

For the resonances $K_1(1270)$ and $K(1460)$, the energy-dependent widths as well as the nominal mass and width are taken from Ref. [21]. We further use the energy-dependent widths for the $K_1(1400)$, $K^*(1410)$ and $K^*(1680)$ mesons from Ref. [9]. For all other resonances decaying into a three-body final state, an energy-dependent width distribution is derived from Equation 2.17 assuming an uniform phase space population.

Some particles may not originate from a resonance but are in a state of relative orbital angular momentum. We denote such non-resonant states by surrounding the particle system with brackets and indicate the partial wave state with an subscript; for example $(\pi\pi)_S$ refers to a non-resonant di-pion S -wave. The lineshape for non-resonant states is set to unity.

124 2.2.2 Spin Densities

125 The spin amplitudes are phenomenological descriptions of decay processes that are required
 126 to be Lorentz invariant, compatible with angular momentum conservation and, where
 127 appropriate, parity conservation. They are constructed in the covariant Zemach (Rarita-
 128 Schwinger) tensor formalism [22–24]. At this point, we briefly introduce the fundamental
 129 objects of the covariant tensor formalism which connect the particle’s four-momenta to
 130 the spin dynamics of the reaction and give a general recipe to calculate the spin factors
 131 for arbitrary decay trees. Further details can be found in Refs. [25, 26].

132 A spin- S particle with four-momentum p , and spin projection λ , is represented by the
 133 polarization tensor $\epsilon_{(S)}(p, \lambda)$, which is symmetric, traceless and orthogonal to p . These
 134 so-called Rarita-Schwinger conditions reduce the a priori 4^S elements of the rank- S tensor
 135 to $2S + 1$ independent elements in accordance with the number of degrees of freedom of a
 136 spin- S state [23, 27].

137 The spin projection operator $P_{(S)}^{\mu_1 \dots \mu_S \nu_1 \dots \nu_S}(p_R)$, for a resonance R , with spin $S =$
 138 $\{0, 1, 2\}$, and four-momentum p_R , is given by [26]:

$$\begin{aligned} P_{(0)}^{\mu\nu}(p_R) &= 1 \\ P_{(1)}^{\mu\nu}(p_R) &= -g^{\mu\nu} + \frac{p_R^\mu p_R^\nu}{p_R^2} \\ P_{(2)}^{\mu\nu\alpha\beta}(p_R) &= \frac{1}{2} \left[P_{(1)}^{\mu\alpha}(p_R) P_{(1)}^{\nu\beta}(p_R) + P_{(1)}^{\mu\beta}(p_R) P_{(1)}^{\nu\alpha}(p_R) \right] - \frac{1}{3} P_{(1)}^{\mu\nu}(p_R) P_{(1)}^{\alpha\beta}(p_R), \end{aligned} \quad (2.20)$$

139 where $g^{\mu\nu}$ is the Minkowski metric. Contracted with an arbitrary tensor, the projection
 140 operator selects the part of the tensor which satisfies the Rarita-Schwinger conditions.

141 For a decay process $R \rightarrow AB$, with relative orbital angular momentum L , between
 142 particle A and B , the angular momentum tensor is obtained by projecting the rank- L
 143 tensor $q_R^{\nu_1} q_R^{\nu_2} \dots q_R^{\nu_L}$, constructed from the relative momenta $q_R = p_A - p_B$, onto the spin- L
 144 subspace,

$$L_{(L)\mu_1 \dots \mu_L}(p_R, q_R) = (-1)^L P_{(L)\mu_1 \dots \mu_L \nu_1 \dots \nu_L}(p_R) q_R^{\nu_1} \dots q_R^{\nu_L}. \quad (2.21)$$

145 Their $|\vec{q}_R|^L$ dependence accounts for the influence of the centrifugal barrier on the transition
 146 amplitudes. For the sake of brevity, the following notation is introduced,

$$\begin{aligned} \varepsilon_{(S)}(R) &\equiv \varepsilon_{(S)}(p_R, \lambda_R), \\ P_{(S)}(R) &\equiv P_{(S)}(p_R), \\ L_{(L)}(R) &\equiv L_{(L)}(p_R, q_R). \end{aligned} \quad (2.22)$$

147 Following the isobar approach, a four-body decay amplitude is described as a product
 148 of two-body decay amplitudes. Each sequential two-body decay $R \rightarrow A B$, with relative
 149 orbital angular momentum L_{AB} , and total intrinsic spin S_{AB} , contributes a term to the
 150 overall spin factor given by

$$\begin{aligned} S_{R \rightarrow AB}(\mathbf{x}|L_{AB}, S_{AB}; \lambda_R, \lambda_A, \lambda_B) &= \varepsilon_{(S_R)}(R) X(S_R, L_{AB}, S_{AB}) L_{(L_{AB})}(R) \\ &\times \Phi(\mathbf{x}|S_{AB}; \lambda_A, \lambda_B), \end{aligned} \quad (2.23)$$

151 where

$$\Phi(\mathbf{x}|S_{AB}; \lambda_A, \lambda_B) = P_{(S_{AB})}(R) X(S_{AB}, S_A, S_B) \varepsilon_{(S_A)}^*(A) \varepsilon_{(S_B)}^*(B). \quad (2.24)$$

152 Here, a polarization vector is assigned to the decaying particle and the complex conjugate
 153 vectors for each decay product. The spin and orbital angular momentum couplings are
 154 described by the tensors $P_{(S_{AB})}(R)$ and $L_{(L_{AB})}(R)$, respectively. Firstly, the two spins S_A
 155 and S_B , are coupled to a total spin- S_{AB} state, $\Phi(\mathbf{x}|S_{AB})$, by projecting the corresponding
 156 polarization vectors onto the spin- S_{AB} subspace transverse to the momentum of the
 157 decaying particle. Afterwards, the spin and orbital angular momentum tensors are
 158 properly contracted with the polarization vector of the decaying particle to give a Lorentz
 159 scalar. This requires in some cases to include the tensor $\varepsilon_{\alpha\beta\gamma\delta} p_R^\delta$ via

$$X(j_a, j_b, j_c) = \begin{cases} 1 & \text{if } j_a + j_b + j_c \text{ even} \\ \varepsilon_{\alpha\beta\gamma\delta} p_R^\delta & \text{if } j_a + j_b + j_c \text{ odd} \end{cases}, \quad (2.25)$$

160 where $\varepsilon_{\alpha\beta\gamma\delta}$ is the Levi-Civita symbol and j refers to the arguments of X defined in
 161 Eqs. 2.23 and 2.24. Its antisymmetric nature ensures the correct parity transformation
 162 behavior of the amplitude. The spin factor for a whole decay chain, for example $R \rightarrow$
 163 $(R_1 \rightarrow AB)(R_2 \rightarrow CD)$, is obtained by combining the two-body terms and performing a
 164 sum over all unobservable, intermediary spin projections

$$\sum_{\lambda_{R_1}, \lambda_{R_2}} S_{R \rightarrow R_1 R_2}(\mathbf{x}|L_{R_1 R_2}; \lambda_{R_1}, \lambda_{R_2}) S_{R_1 \rightarrow AB}(\mathbf{x}|L_{AB}; \lambda_{R_1}) S_{R_2 \rightarrow CD}(\mathbf{x}|L_{CD}; \lambda_{R_2}), \quad (2.26)$$

165 where $\lambda_R = \lambda_A = \lambda_B = \lambda_C = \lambda_D = 0$, $S_{AB} = S_{CD} = 0$ and $S_{R_1 R_2} = L_{R_1 R_2}$, as only
 166 pseudoscalar initial/final states are involved.

167 The spin factors for all decay topologies considered in this analysis are explicitly given
 168 in Appendix F.

169 2.3 Fit implementation

170 The hadronic amplitudes are renormalized prior to the amplitude fit such that

$$\int |A_i(\mathbf{x})|^2 d\Phi_4 = 1. \quad (2.27)$$

171 This allows us to set more intuitive starting values as the amplitude coefficients are all on
 172 a comparable scale. Moreover, the total amplitudes $\mathcal{A}_f^{c(u)}(\mathbf{x})$ are renormalized on-the-fly
 173 (*i.e.* at each minimization step) such that

$$\begin{aligned} & \int \left| \mathcal{A}_f^{c(u)}(\mathbf{x}) \right|^2 d\Phi_4 = 1 \\ & \arg \left(\int \mathcal{A}_f^c(\mathbf{x})^* \mathcal{A}_f^u(\mathbf{x}) d\Phi_4 \right) = 0. \end{aligned} \quad (2.28)$$

174 As a result, the average amplitude ratio and strong phase difference between the $b \rightarrow u$ and
 175 $b \rightarrow c$ transitions can be introduced as direct fit parameters instead of derived quantities
 176 that have to be calculated from Equation 2.11 after the fit. For the differential decay rate
 177 follows:

$$\begin{aligned} \frac{d\Gamma(\mathbf{x}, t, q, f)}{e^{-\Gamma_s t} dt d\Phi_4} \propto & \left(|\mathcal{A}_f^c(\mathbf{x})|^2 + r^2 |\mathcal{A}_f^u(\mathbf{x})|^2 \right) \cosh \left(\frac{\Delta\Gamma_s t}{2} \right) \\ & + q f \left(|\mathcal{A}_f^c(\mathbf{x})|^2 - r^2 |\mathcal{A}_f^u(\mathbf{x})|^2 \right) \cos (\Delta m_s t) \\ & - 2 r \text{Re} \left(\mathcal{A}_f^c(\mathbf{x})^* \mathcal{A}_f^u(\mathbf{x}) e^{i\delta - if(\gamma - 2\beta_s)} \right) \sinh \left(\frac{\Delta\Gamma_s t}{2} \right) \\ & - 2 q f r \text{Im} \left(\mathcal{A}_f^c(\mathbf{x})^* \mathcal{A}_f^u(\mathbf{x}) e^{i\delta - if(\gamma - 2\beta_s)} \right) \sin (\Delta m_s t) \end{aligned} \quad (2.29)$$

178 This renormalization procedure was found to be crucial for the fit stability since it reduces
 179 the correlation between the a_i^c and a_i^u amplitude coefficients significantly. Due to the
 180 overall normalization, one of the complex amplitude coefficients a_i^c can be fixed to unity
 181 and since r and δ are included as fit parameters one of the complex amplitude coefficient
 182 a_i^u can be additionally fixed to unity.

183 We force strong decays in the cascade topology to have the same pattern in $b \rightarrow c$
 184 and $b \rightarrow u$ transitions by the sharing of couplings between related quasi-two-body final
 185 states. For example, given the two a_i^c parameters required for $B_s \rightarrow D_s^- K_1(1270)^+$
 186 with $K_1(1270)^+ \rightarrow \rho(770)^0 \pi^+$ and $K_1(1270)^+ \rightarrow K^*(892) \pi^+$, the amplitude $\bar{B}_s \rightarrow$
 187 $D_s^- K_1(1270)^+$ with $K_1(1270)^+ \rightarrow \rho(770)^0 \pi^+$ and $K_1(1270)^+ \rightarrow K^*(892) \pi^+$ only requires
 188 one additional global complex parameter to represent the different production processes
 189 of $B_s \rightarrow D_s^- K_1(1270)^+$ and $\bar{B}_s \rightarrow D_s^- K_1(1270)^+$, while the relative magnitude and phase
 190 of $K_1(1270)^+ \rightarrow \rho(770)^0 \pi^+$ and $K_1(1270)^+ \rightarrow K^*(892) \pi^+$ are the same regardless of
 191 the production mechanism. For this purpose, multiple decay amplitudes of a three-body
 192 resonance are defined relative to a given reference channel.

193 2.4 Validation

194 The amplitude fit is performed by using the amplitude analysis tool **MINT2**. It was
 195 previously applied to analyze $D^0 \rightarrow 4\pi$ and $D^0 \rightarrow KK\pi\pi$ decays [9] which have an
 196 identical general spin structure (*i.e.* scalar to four scalar decay) to $B_s \rightarrow D_s K\pi\pi$ decays.
 197 In the course of the $D^0 \rightarrow hhhh$ analysis, the implementation of the amplitudes were
 198 extensively cross-checked against other available tools such as **qft++** [28], **AmpGen** [21]
 199 and where possible **EVTGEN** [29]. Since no additional line shapes or spin factors are
 200 needed for this analysis, we consider the amplitude calculation as fully validated.

201 This does, however, not apply to the full time-dependent amplitude pdf which is
 202 newly implemented for this analysis. To cross-check it, we use **EVTGEN** to generate
 203 toy events with time-dependent CP violation according to the **SSD_Cp** event model [29].
 204 Since this event model does not allow for multiple interfering resonances, we generate
 205 only the decay chain $B_s \rightarrow D_s(K_1(1400) \rightarrow K^*(892)\pi)$. Table 2.1 lists the generated
 206 input parameters. The toy data set is fitted with our **MINT2** implementation of the full
 207 time-dependent amplitude pdf and the phasespace-integrated pdf. Flat decay-time and
 208 phase-space acceptances are used. The true ID of the B_s meson is used to tag the initial
 209 flavor (*i.e.* perfect tagging). For technical reasons (the extreme case of perfect resolution
 210 is currently not implemented in our fitter) we smeared the generated decay-times with a
 211 Gaussian of width 45 fs. We use a Gaussian of the same width to convolute the pdf for
 212 fitting. More details of the fit procedures are given in Secs. 9 and 10. The fit projections
 213 are shown in Figs. 2.1 and 2.2.

214 The CP coefficients $C, D, \bar{D}, S, \bar{S}$ are the fit parameters in case of the phasespace-
 215 integrated pdf, which are converted after to the fit to the physical observables r, κ, δ and γ
 216 using the **GammaCombo** package [30]. The obtained 1-CL contours are shown in Fig. 2.3.
 217 The full pdf determines r, δ and γ directly. As shown in Tab. 2.2 and 2.3, the fit results
 218 are in excellent agreement with the generated input values. The phasespace-integrated fit
 219 is, in addition, performed with the **B2DX** fitter used for the $B_s \rightarrow D_s K$ analysis yielding
 220 identical results. Note though that some parts of the **B2DX** fitter have been taken over to
 221 our **MINT2** fitter, such that the implementations are not fully independent.

Table 2.1: Input values used to generate **EVTGEN** toy events according to the **SSD_Cp** event model.

τ	1.5 ps
$\Delta\Gamma$	-0.1 ps^{-1}
Δm_s	17.757 ps^{-1}
r	0.37
κ	1
δ	10.0°
γ	71.1°
β_s	0.0°

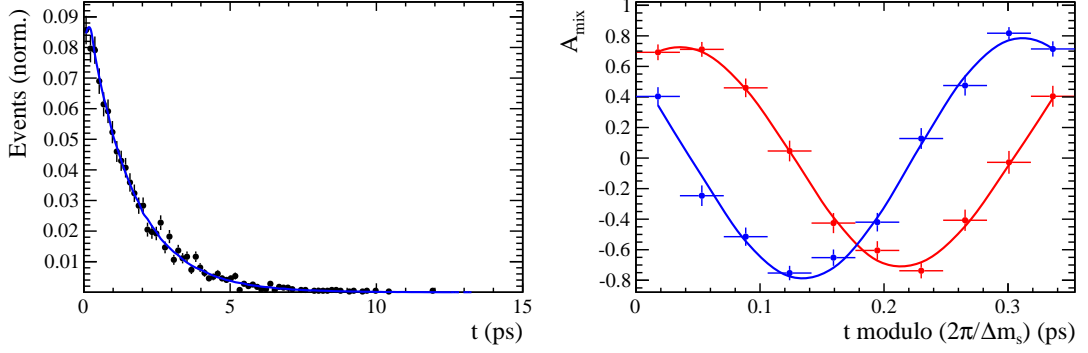


Figure 2.1: Left: Time distribution of $B_s \rightarrow D_s K \pi \pi$ events generated with EVTGEN (points with error bars) and MINT2 fit projections (solid line). Right: Time-dependent asymmetry between mixed and unmixed events folded into one oscillation period for $D_s^- K^+ \pi \pi$ (red) and $D_s^+ K^- \pi \pi$ (blue) final states. The data points show events generated with EVTGEN, while the solid lines show the MINT2 fit projections.

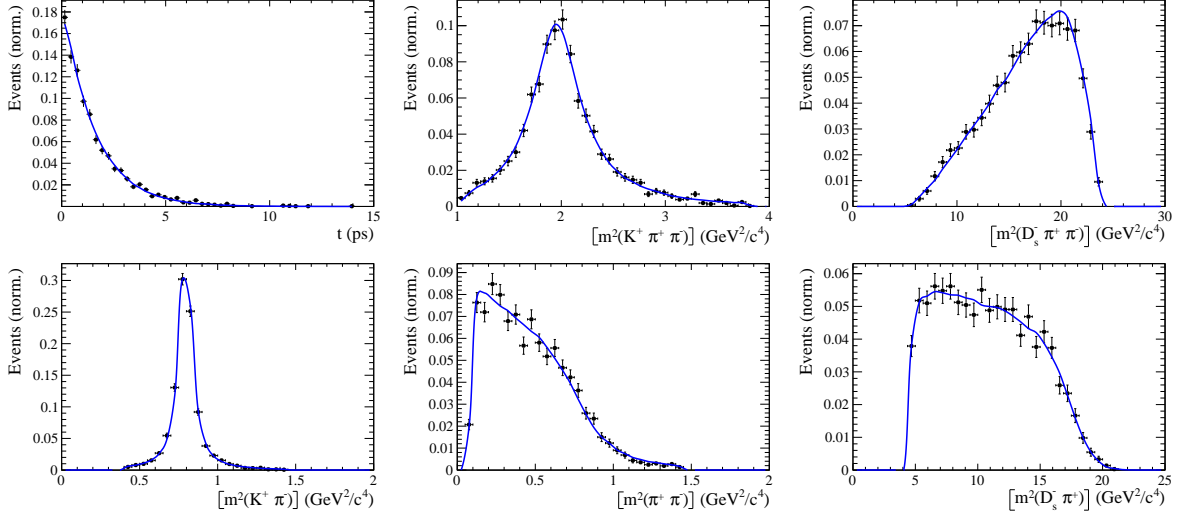


Figure 2.2: Time and invariant mass distributions of $B_s \rightarrow D_s K \pi \pi$ events generated with EVTGEN (points with error bars) and MINT2 fit projections (blue solid line).

Table 2.2: Result of the phasespace-integrated fit to EVTGEN toy events.

	Generated	Fit result	Pull(σ)
C	0.759	0.763 ± 0.026	0.2
D	-0.314	-0.376 ± 0.227	-0.3
\bar{D}	-0.101	-0.261 ± 0.246	-0.7
S	-0.570	-0.626 ± 0.035	1.6
\bar{S}	-0.643	-0.669 ± 0.035	-0.7

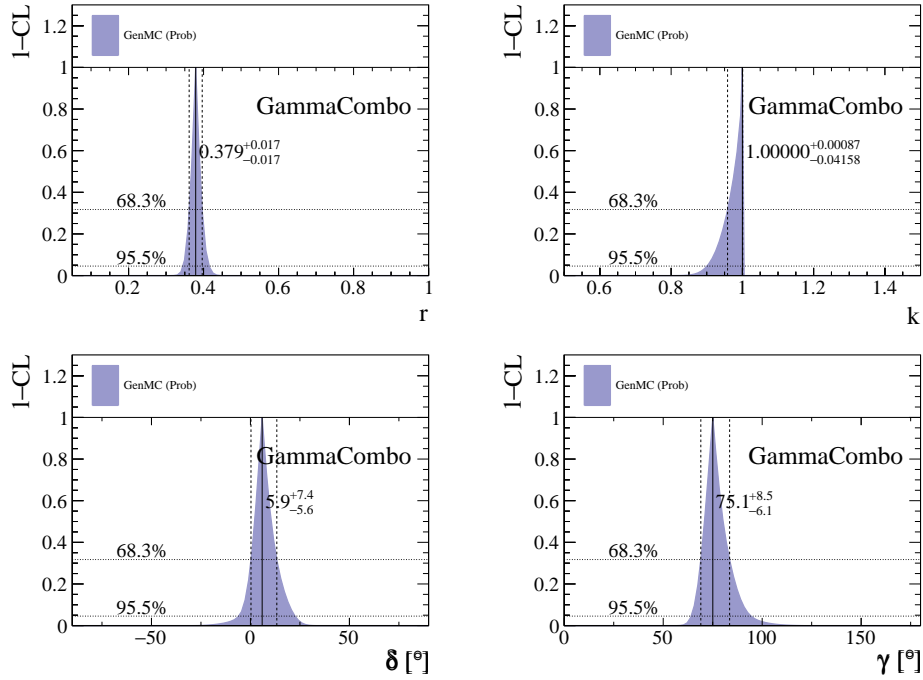


Figure 2.3: The 1-CL contours for the physical observable r, κ, δ and γ obtained with the phasespace-integrated fit to the EVTGEN toy sample.

Table 2.3: Results for the physical observables obtained from fits to EVTGEN toy events.

	Generated	Full PDF	Phasespace-integrated
r	0.370	0.379 ± 0.021	0.379 ± 0.017
κ	1.0	1.0	1.000 ± 0.059
δ	10.0°	9.0 ± 5.1	5.9 ± 6.0
γ	71.1°	67.3 ± 5.9	75.1 ± 6.9

222 3 Data samples and event selection

223 3.1 Stripping and Trigger selection

224 The dataset used for this analysis corresponds to 1 fb^{-1} of proton-proton collision data col-
225 lected in 2011 with a centre of mass energy $\sqrt{s} = 7 \text{ TeV}$, 2 fb^{-1} collected in 2012 with $\sqrt{s} =$
226 7 TeV and 4 fb^{-1} collected in 2015/2016/2017 with $\sqrt{s} = 13 \text{ TeV}$. Candidate $B_s^0 \rightarrow D_s K \pi \pi$
227 ($B_s^0 \rightarrow D_s \pi \pi \pi$) decays are reconstructed using the `B02DKPiPiD2HHHPIDBeauty2CharmLine`
228 (`B02DPiPiD2HHHPIDBeauty2CharmLine`) line of the `BHadronCompleteEvent` stream of
229 `Stripping21r1` (2011), `Stripping21` (2012), `Stripping24r1` (2015) and `Stripping28r1p1` (2016)
230 and `Stripping29r2` (2017). Both stripping lines employ the same selection cuts, listed in
231 Appendix A, except for the PID requirement on the bachelor kaon/pion.

232 Events that pass the stripping selection are further required to fulfill the following
233 trigger requirements: at the hardware stage, the B_s^0 candidates are required to be TOS
234 on the `L0Hadron` trigger or TIS on `L0Global`; at Hlt1, B_s^0 candidates are required to be
235 TOS on the `Hlt1TrackAllL0` (`Hlt1TrackMVA` or `Hlt1TwoTrackMVA`) trigger line for Run-I
236 (Run-II) data; at Hlt2, candidates have to be TOS on either one of the 2, 3 or 4-body
237 topological trigger lines or the inclusive ϕ trigger. More details on the used HLT lines are
238 given in Appendix A.

239 Due to a residual kinematic dependence on whether the event is triggered by `L0Hadron`
240 or not and on the data taking condition, the analysis is performed in four disjoint categories:
241 `[Run-I,L0-TOS]`, `[Run-I,L0-TIS]`, `[Run-II,L0-TOS]` and `[Run-II,L0-TIS]`, where for simplic-
242 ity we denote `L0Hadron-TOS` as `L0-TOS` and (`L0Global-TIS` and not `L0Hadron-TOS`) as
243 `L0-TIS`.

244 3.2 Offline selection

245 The offline selection, in particular the requirements on the D_s hadron, are guided by
246 the previous analyses of $B_s \rightarrow D_s K/\pi$, $B_d \rightarrow D^0 \pi$ as well as the branching fraction
247 measurement of $B_s^0 \rightarrow D_s K \pi \pi$ decays. Tables 3.1 and 3.2 summarize all selection
248 requirements which are described in the following. Throughout the note, we abbreviate
249 $B_s^0 \rightarrow D_s X_s (\rightarrow K \pi \pi)$ and $B_s^0 \rightarrow D_s X_d (\rightarrow \pi \pi \pi)$.

250 Given the high number of pp interactions per bunch crossing, a large fraction of
251 events have more than one reconstructed PV. We choose the 'best' PV to be the one
252 to which the B_s candidate has the smallest χ_{IP}^2 . In instances where the association
253 of the B_s candidate to the best PV is wrong, the decay time of this candidate will be
254 incorrect. These wrongly associated candidates are rejected by requiring that the B_s
255 χ_{IP}^2 with respect to any other PV is sufficiently higher than with respect to the best PV
256 ($\Delta\chi_{IP}^2 = \chi_{IP,\text{SECONDBEST}}^2 - \chi_{IP,\text{BEST}}^2 > 20$). Events with only a single PV are not affected.

257 In order to clean up the sample and to align the Run-I to the slightly tighter Run-II
258 stripping selection, we apply the following loose cuts to the b-hadron:

- 259 • DIRA > 0.99994
- 260 • min IP $\chi^2 < 16$ to the best PV,
- 261 • FD $\chi^2 > 100$ to the best PV,
- 262 • Vertex $\chi^2/\text{nDoF} < 8$.

263 The cut on the B_s decay-time is tightened with respect to the stripping selection ($t > 0.2$ ps)
264 because, while offline we use the decay-time determined for a DTF in which the PV position,
265 the D_s and the B_s mass are constrained, in the stripping the simple decay-time returned
266 by a kinematic fit is used. The difference between these two decay-times extends up to 0.1
267 ps, thus cutting at 0.4 ps avoids any boundary effects and simplifies the time-acceptance
268 studies. We further remove outliers with poorly estimated decay times ($\delta t < 0.15$ ps).

269 We reconstruct the $B_s^0 \rightarrow D_s h\pi\pi$ decay through three different final states of the
270 D_s meson: $D_s \rightarrow KK\pi$, $D_s \rightarrow \pi\pi\pi$ and $D_s \rightarrow K\pi\pi$. Of those, $D_s \rightarrow KK\pi$ is the
271 most prominent one, while $\mathcal{BR}(D_s \rightarrow \pi\pi\pi) \approx 0.2 \cdot \mathcal{BR}(D_s \rightarrow KK\pi)$ and $\mathcal{BR}(D_s \rightarrow$
272 $K\pi\pi) \approx 0.12 \cdot \mathcal{BR}(D_s \rightarrow KK\pi)$ holds for the others. For the $KK\pi$ final state we make
273 use of the well known resonance structure; the decay proceeds either via the narrow ϕ
274 resonance, the broader K^{*0} resonance or (predominantly) non-resonant. Within the ϕ
275 resonance region the sample is already sufficiently clean after the stripping so that we do
276 not impose additional criteria on the D_s daughters. For the K^{*0} and non-resonant regions
277 consecutively tighter requirements on the particle identification and the D_s flight-distance
278 are applied. We apply global requirements (*i.e.* independent of the D_s Dalitz-plot position)
279 for the other final states. All cuts are summarized in Table 3.1.

280 3.2.1 Phase space region

281 Due to the comparably low masses of the final state particles with respect to the B_s
282 mass, there is, in contrast to for example b-hadron to charmonia or charm decays, a
283 huge phase-space available for the $B_s^0 \rightarrow D_s K\pi\pi$ decay. For the invariant mass of
284 the $K\pi\pi$ subsystem it extends up to 3.4 GeV. It has however been observed that the
285 decay proceeds predominantly through the low lying axial vector states $K_1(1270)$ and
286 $K_1(1400)$, while the combinatorial background is concentrated at high $K\pi\pi$ invariant
287 masses ($m(K\pi\pi) > 2000$ MeV). Moreover, the strange hadron spectrum above 2 GeV
288 is poorly understood experimentally such that a reliable extraction of the strong phase
289 motion in that region is not possible. We consequently choose to limit the considered
290 phase space region to $m(K\pi\pi) < 1950$ MeV, which is right below the charm-strange
291 threshold ($B_s^0 \rightarrow D_s^+ D_s^-$).

292 **3.2.2 Physics background vetoes**

293 We veto various physical backgrounds, which have either the same final state as our
 294 signal decay, or can contribute via a single misidentification of $K \leftrightarrow \pi$, $K \leftrightarrow p$ or $\pi \leftrightarrow p$.
 295 Depending on the D_s final state different vetoes are applied in order to account for peaking
 296 backgrounds originating from charm meson or charmed baryon decays.

297 1. $D_s^- \rightarrow K^+ K^- \pi^-$

298 (a) $D^- \rightarrow K^+ \pi^- \pi^-$:

299 Possible with $\pi^- \rightarrow K^-$ misidentification, vetoed by requiring $m(K^+ K_\pi^- \pi^-) \neq$
 300 $m(D^-) \pm 40$ MeV or the K^- has to fulfill more stringent PID criteria depending
 301 on the resonant region (see Table 3.1).

302 (b) $\Lambda_c^- \rightarrow K^+ \bar{p} \pi^-$:

303 Possible with $\bar{p} \rightarrow K^-$ misidentification, vetoed by requiring $m(K^+ K_p^- \pi^-) \neq$
 304 $m(\Lambda_c^-) \pm 40$ MeV or the K^- has to fulfill more stringent PID criteria depending
 305 on the resonant region (see Table 3.1).

306 (c) $D^{*-} \rightarrow (D^0 \rightarrow KK)\pi^-$:

307 Same final state, vetoed by requiring $(M(KK\pi^-) - m(KK)) > 155$ MeV.

308 2. $D_s^- \rightarrow \pi^+ \pi^- \pi^-$

309 (a) $D^{*-} \rightarrow (D^0 \rightarrow \pi\pi)\pi^-$:

310 Same final state, vetoed by requiring $(M(\pi\pi\pi^-) - m(\pi\pi)) > 155$ MeV.

311 3. $D_s^- \rightarrow K^- \pi^+ \pi^-$

312 (a) $D^- \rightarrow \pi^- \pi^+ \pi^-$:

313 Possible with $\pi^- \rightarrow K^-$ misidentification, vetoed by requiring $m(K_\pi^- \pi^+ \pi^-) \neq$
 314 $m(D^-) \pm 40$ MeV or $\text{PIDK}(K^+) > 15$.

315 (b) $\Lambda_c^- \rightarrow \bar{p} \pi^+ \pi^-$:

316 Possible with $\bar{p} \rightarrow K^-$ misidentification, vetoed by requiring $m(K_p^- \pi^+ \pi^-) \neq$
 317 $m(\Lambda_c^-) \pm 40$ MeV or $\text{PIDK}(K^-) - \text{PIDp}(K^-) > 5$.

318 (c) $D^{*-} \rightarrow (D^0 \rightarrow K\pi)\pi^-$:

319 Same final state, vetoed by requiring $(M(K\pi\pi^-) - m(K\pi)) > 155$ MeV.

320 The effects of these veto cuts are illustrated in Figs. 3.1,3.2 and 3.3. To reduce cross-feed
 321 from our calibration channel into the signal channel and vice-versa we require tight PID
 322 cuts on the ambiguous bachelor track; for the signal channel we apply $\text{PIDK}(K^+) > 10$
 323 and for the calibration channel $\text{PIDK}(\pi^+) < 0$. In addition, we veto $B_s^0 \rightarrow D_s^- D_s^+$ decays
 324 which is illustrated in Fig. 3.4.

- 325 1. $X_s^+ \rightarrow K^+\pi^+\pi^-$:
- 326 (a) $B_s^0 \rightarrow D_s\pi\pi\pi$:
 327 Possible with $\pi^+ \rightarrow K^+$ misidentification, suppressed with $\text{PIDK}(K^+) > 10$.
- 328 (b) $B_s^0 \rightarrow D_s^-(D_s^+ \rightarrow K^+\pi^+\pi^-)$:
 329 Outside of considered phase-space region, see Sec. 3.2.1.
- 330 (c) $B_s^0 \rightarrow D_s^-(D_s^+ \rightarrow K^+K^-\pi^+)$:
 331 To suppress $B_s^0 \rightarrow D_s^-K^+K^-\pi^+$ background, possible with $K^- \rightarrow \pi^-$ misiden-
 332 tification, we require $\text{PIDK}(\pi^-) < 0$. In case the invariant mass of the $K^+\pi^+\pi^-$
 333 system recomputed applying the kaon mass hypothesis to the pion is close to
 334 the D_s mass ($m(K^+\pi^+\pi_K^-) = m(D_s) \pm 20$ MeV), we further tighten the cut to
 335 $\text{PIDK}(\pi^-) < -5$.
- 336 2. $X_d^+ \rightarrow \pi^+\pi^+\pi^-$:
- 337 (a) $B_s^0 \rightarrow D_sK\pi\pi$:
 338 Possible with single missID of $K^+ \rightarrow \pi^+$, suppressed with $\text{PIDK}(\pi^+) < 0$.
- 339 (b) $B_s^0 \rightarrow D_s^-(D_s^+ \rightarrow \pi^+\pi^+\pi^-)$:
 340 Outside of considered phase-space region, see Sec. 3.2.1.
- 341 (c) $B_s^0 \rightarrow D_s^-(D_s^+ \rightarrow K^+\pi^-\pi^+)$:
 342 Possible with single missID of $K^+ \rightarrow \pi^+$, vetoed by requiring $m(\pi^+\pi_K^+\pi^-) \neq$
 343 $m(D_s) \pm 20$ MeV or $\text{PIDK}(\pi^+) < -5$ for both π^+ .

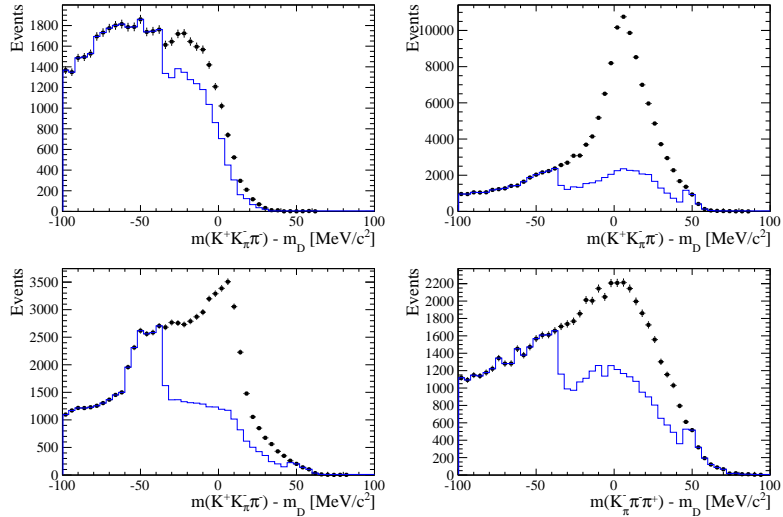


Figure 3.1: Background contributions from D^- decays where the π^- is misidentified as K^- . The D_s invariant mass is recomputed applying the pion mass hypothesis to the kaon and shown for the $D_s \rightarrow \phi\pi$, $D_s \rightarrow K^*(892)K$, $D_s \rightarrow KK\pi$ (non-resonant) and $D_s \rightarrow K\pi\pi$ final state categories from top-left to bottom-right. The distributions are shown without (black) and with (blue) the D^- -veto applied.

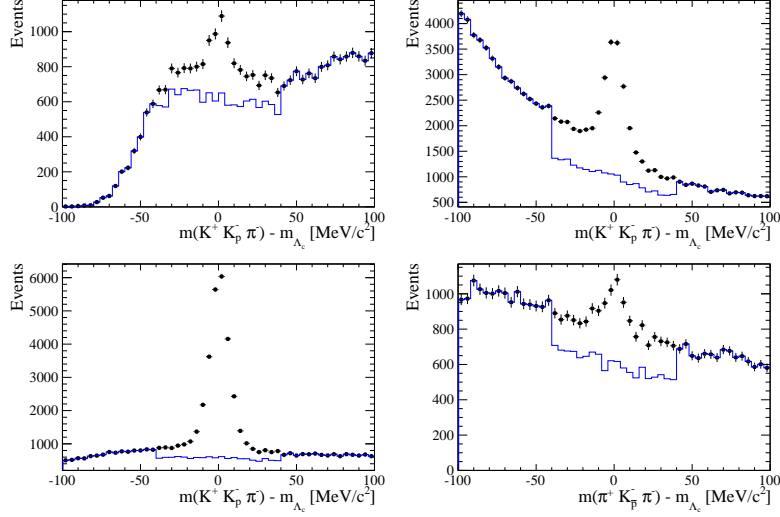


Figure 3.2: Background contributions from Λ_c decays where the \bar{p} is misidentified as K^- . The D_s invariant mass is recomputed applying the proton mass hypothesis to the kaon and shown for the $D_s \rightarrow \phi\pi$, $D_s \rightarrow K^*(892)K$, $D_s \rightarrow KK\pi$ (non-resonant) and $D_s \rightarrow K\pi\pi$ final state categories from top-left to bottom-right. The distributions are shown without (black) and with (blue) the Λ_c -veto applied.

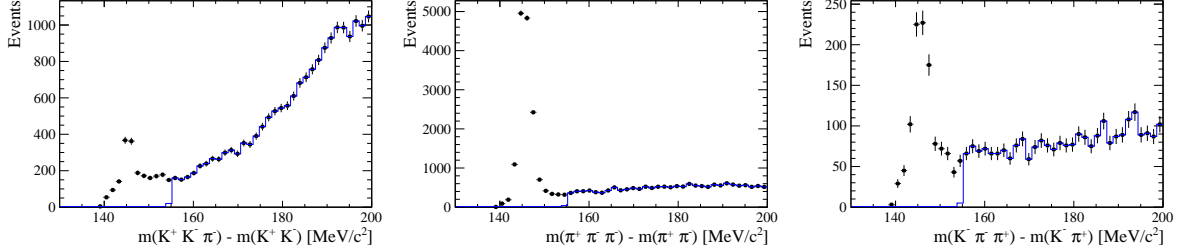


Figure 3.3: Background contributions to $D_s^- \rightarrow KK\pi$ (left), $D_s^- \rightarrow \pi\pi\pi$ (middle) and $D_s^- \rightarrow K\pi\pi$ (right) from $D^{*-} \rightarrow (D^0 \rightarrow hh)\pi^-$ decays. The D^{*-} background contribution peaks at $m(hh\pi^-) - m(hh) \approx 145.5$ MeV which corresponds to the mass difference of the D^{*-} and D^0 mesons.

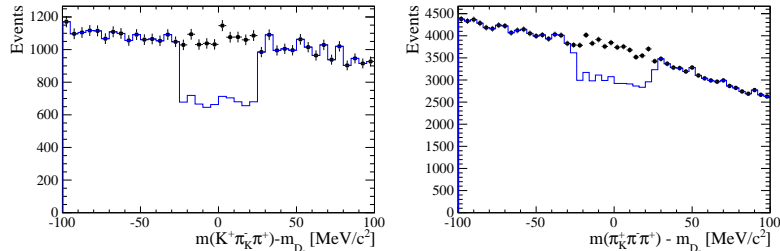


Figure 3.4: Background contributions to $B_s \rightarrow D_s K\pi\pi$ (left) and $B_s \rightarrow D_s \pi\pi\pi$ (right) from $B_s \rightarrow D_s D_s$ decays where the kaon is misidentified as pion. The $X_{s,d}$ invariant mass is recomputed applying the kaon mass hypothesis to the pion and shown without (black) and with (blue) the D_s -veto applied.

3.2.3 Training of multivariate classifier

The Toolkit for Multivariate Analysis (TMVA [31]) is used to train a multivariate classifier (BDT with gradient boosting, BDTG) discriminating signal and combinatorial background. We use $B_s \rightarrow D_s \pi\pi$ data that passes the preselection as signal proxy. The background is statistically subtracted by applying `sWeights` based on the fit to the reconstructed B_s mass shown in Fig. 3.5. This is a simplified version (performed in a reduced mass range) of the final mass fits described in Sec. 4. The sideband data ($m(B_s) > 5500$ MeV) is used as background proxy.

Training the classifier on a sub-sample which is supposed to be used in the final analysis might cause a bias, as the classifier selects, in case of overtraining, the training events more efficiently. As overtraining can not be completely avoided, we split the signal and the background training samples into two disjoint subsamples according to whether the event number is even or odd. We then train the classifier on the even sample and apply it to the odd one, and vice-versa (cross-training).

The following discriminating variables are used for the BDTG training:

- logarithm of the B_s impact-parameter χ^2 , $B_s \log(\chi_{IP}^2)$
- logarithm of the cosine of the B_s direction angle, $\log(\text{DIRA})$
- fit quality of the DTF with PV constrain, χ_{DTF}^2/ndf
- logarithm of the minimal vertex quality difference for adding one extra track, $\log(\Delta\chi_{add-track}^2)$
- the asymmetry between the transverse momentum of the B_s - candidate and the transverse momentum of all the particles reconstructed with a cone of radius $r = \sqrt{(\Delta\Phi)^2 + (\Delta\eta)^2} < 1$ rad around the B_s - candidate, $B_s A_{pT}^{\text{cone}}$
- largest ghost probability of all tracks, $\max(\text{ghostProb})$
- logarithm of the the smallest X_s daughter impact-parameter χ^2 , $X_s \log(\min(\chi_{IP}^2))$
- largest distance of closest approach of the X_s daughters, $\max(\text{DOCA})$
- cosine of the largest opening angle between the D_s and another bachelor track h_i in the plane transverse to the beam, $\cos(\max \theta_{D_s h_i})$
- logarithm of the the smallest D_s daughter impact-parameter χ^2 , $D_s \log(\min(\chi_{IP}^2))$
- logarithm of the D_s flight-distance significance, $D_s \log(\chi_{FD}^2)$
- logarithm of the D_s radial flight-distance, $D_s \log(RFD)$

Loose cuts on the variables χ_{DTF}^2/ndf , $\Delta\chi_{add-track}^2$ and $\cos(\max \theta_{D_s h_i})$ are applied prior to the training which are expected to be 100% signal efficient. Figure 3.6 shows the distributions of the input variables for signal and background. As shown in Appendix B, these distributions differ between data-taking period and trigger category. In particular variables depending on the B_s kinematics and the event multiplicity are affected (*e.g.* $\theta_{D_s h_i}$ or A_{pT}^{cone}). The BDTG is consequently trained separately for these categories. The resulting classifier response is shown in Fig. 3.7 for each category (even and odd test samples combined) and in Appendix B for each training.

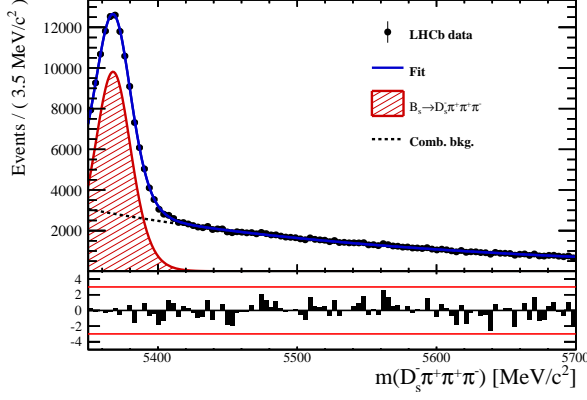


Figure 3.5: Reconstructed B_s mass for $B_s \rightarrow D_s \pi\pi\pi$ events that pass the preselection. The fitted PDF is shown in blue, the signal component in red and the background component in black.

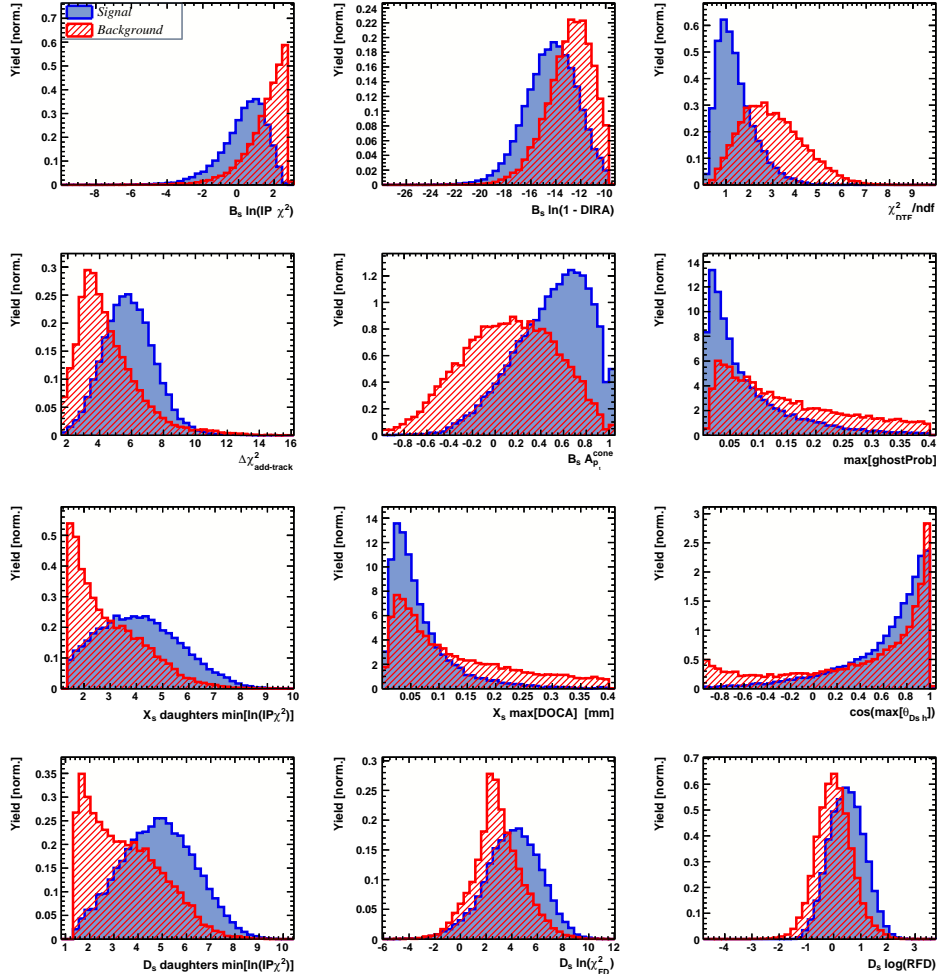


Figure 3.6: Discriminating variables used to train the BDTG for all data categories combined.

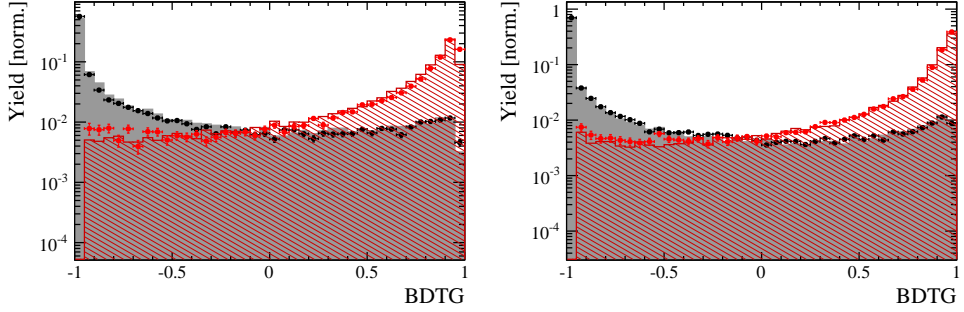


Figure 3.7: Signal (red) and background (black) distributions for the BDTG response for Run-I (left) and Run-II (right) data. Filled histograms (data points) show the BDTG response for the L0-TOS (L0-TIS) category. Even and odd test samples are combined.

3.2.4 Final selection

The cut on the BDTG output is optimized using the signal significance as figure of merit:

$$\text{FOM}(\text{BDTG}) = \frac{N_s(\text{BDTG})}{\sqrt{N_s(\text{BDTG}) + N_b(\text{BDTG})}} \quad (3.1)$$

where $N_s(\text{BDTG})$ is the $B_s \rightarrow D_s K\pi\pi$ signal yield for a given BDTG cut and $N_b(\text{BDTG})$ is the combinatorial background yield in the signal region ($m(D_s K\pi\pi) = m_{B_s} \pm 40 \text{ MeV}$). To compute the yields as function of the BDTG cut, we use the BDTG efficiencies, $\epsilon_{s,b}$, evaluated on the corresponding test samples. To fix the overall scale, it is required to know the yields at (at least) one point of the scanned range. We arbitrarily choose this fix point to be $\text{BDTG} > 0$ and perform a fit to the reconstructed B_s mass as described in Sec. 4 to obtain the yields $N_{s,b}(0)$. These yields are then efficiency corrected to calculate the yields for a given BDTG cut:

$$N_{s,b}(\text{BDTG}) = N_{s,b}(0) \cdot \frac{\epsilon_{s,b}(\text{BDTG})}{\epsilon_{s,b}(0)}. \quad (3.2)$$

Figure 3.8 shows the resulting BDTG scans for each training category.

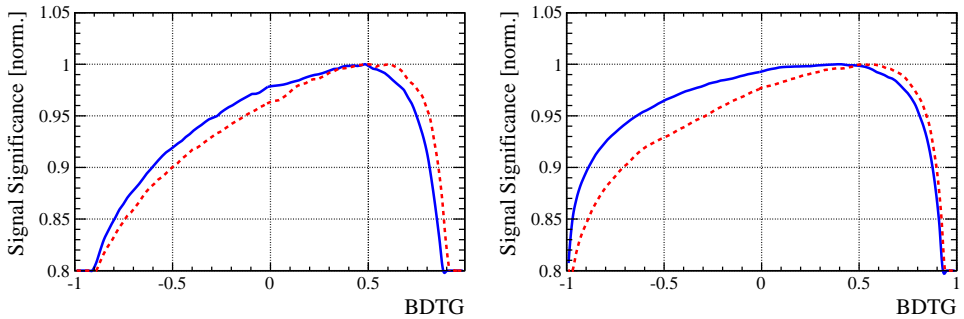


Figure 3.8: Signal significance as function of the applied cut on the BDTG response for Run-I (left) and Run-II (right) data. The scans for the L0-TOS (L0-TIS) category are shown in blue (red). The signal significance is normalized to be 1 at the optimal BDTG cut value.

Table 3.1: Offline selection requirements for $D_s \rightarrow 3h$ candidates.

	Description	Requirement
$D_s \rightarrow hh\bar{h}$	$m(hh\bar{h})$	$= m_{D_s} \pm 25$ MeV
$D_s^- \rightarrow KK\pi^-$	D^{*-} veto	$m(KK\pi^-) - m(KK) > 155$ MeV
$D_s^- \rightarrow \phi\pi^-$	$m(KK)$ PIDK(K^+) PIDK(K^-) PIDK(π^-) χ_{FD}^2 FD in z D^- veto Λ_c veto	$= m_\phi \pm 12$ MeV > -10 > -10 < 20 > 0 > -1 $m(K^+K_\pi^-\pi^-) \neq m(D^-) \pm 40$ MeV PIDK(K^-) > 5 $m(K^+K_p^-\pi^-) \neq m(\Lambda_c) \pm 40$ MeV PIDK(K^-) – PIDp(K^-) > 2
$D_s^- \rightarrow K^*(892)K^-$	$m(KK)$ $m(K^+\pi^-)$ PIDK(K^+) PIDK(K^-) PIDK(π^-) χ_{FD}^2 FD in z D^- veto Λ_c veto	$\neq m_\phi \pm 12$ MeV $= m_{K^*(892)} \pm 75$ MeV > -10 > -5 < 10 > 0 > 0 $m(K^+K_\pi^-\pi^-) \neq m(D^-) \pm 40$ MeV PIDK(K^-) > 15 $m(K^+K_p^-\pi^-) \neq m(\Lambda_c) \pm 40$ MeV PIDK(K^-) – PIDp(K^-) > 5
$D_s^- \rightarrow (KK\pi^-)_{NR}$	$m(KK)$ $m(K^+\pi^-)$ PIDK(K^+) PIDK(K^-) PIDK(π^-) χ_{FD}^2 FD in z D^- veto Λ_c veto	$\neq m_\phi \pm 12$ MeV $\neq m_{K^*(892)} \pm 75$ MeV > 5 > 5 < 10 > 4 > 0 $m(K^+K_\pi^-\pi^-) \neq m(D^-) \pm 40$ MeV PIDK(K^-) > 15 $m(K^+K_p^-\pi^-) \neq m(\Lambda_c) \pm 40$ MeV PIDK(K^-) – PIDp(K^-) > 5
$D_s^- \rightarrow \pi\pi\pi$	PIDK(π) PIDp(π) D^{*-} veto χ_{FD}^2 FD in z	< 10 < 20 $m(\pi\pi\pi^-) - m(\pi\pi) > 155$ MeV > 9 > 0
$D_s^- \rightarrow K^-\pi^+\pi^-$	PIDK(K) PIDK(π) PIDp(π) D^{*-} veto χ_{FD}^2 FD in z D^- veto Λ_c veto	> 8 < 5 < 20 $m(K^-\pi^+\pi^-) - m(K^-\pi^+) > 155$ MeV > 9 > 0 $m(K_\pi^-\pi^+\pi^-) \neq m(D^-) \pm 40$ MeV PIDK(K^-) > 15 $m(K_p^-\pi^+\pi^-) \neq m(\Lambda_c) \pm 40$ MeV PIDK(K^-) – PIDp(K^-) > 5

Table 3.2: Offline selection requirements for $B_s \rightarrow D_s K\pi\pi(D_s\pi\pi\pi)$ candidates.

	Description	Requirement
$B_s \rightarrow D_s h\pi\pi$	$m(D_s h\pi\pi)$	$> 5200 \text{ MeV}$
	χ^2_{vtx}/ndof	< 8
	DIRA	> 0.99994
	χ^2_{FD}	> 100
	χ^2_{IP}	< 16
	χ^2_{DTF}/ndof	< 15
	$\Delta\chi^2_{add-track}$	> 2
	$\cos(\max \theta_{D_s h_i})$	> -0.9
	t	$> 0.4 \text{ ps}$
	δt	$< 0.15 \text{ ps}$
	Phasespace region	$m(h\pi\pi) < 1.95 \text{ GeV}$ $m(h\pi) < 1.2 \text{ GeV}$ $m(\pi\pi) < 1.2 \text{ GeV}$
Wrong PV veto		$\text{nPV} = 1 \parallel \min(\Delta\chi^2_{IP}) > 20$
BDTG		$> 0.45 \text{ [Run-I,L0-TOS]}$ $> 0.50 \text{ [Run-I,L0-TIS]}$ $> 0.35 \text{ [Run-II,L0-TOS]}$ $> 0.50 \text{ [Run-II,L0-TIS]}$
$X_s^+ \rightarrow K^+\pi^+\pi^-$	PIDK(K)	> 10
	PIDK(π^+)	< 10
	PIDK(π^-)	< 0
	D_s veto	$m(K^+\pi^+\pi_K^-) \neq m(D_s) \pm 20 \text{ MeV} \parallel \text{PIDK}(\pi^-) < -5$
$X_d^+ \rightarrow \pi^+\pi^+\pi^-$	PIDK(π^+)	< 0
	PIDK(π^-)	< 10
	D_s veto	$m(\pi^+\pi_K^+\pi^-) \neq m(D_s) \pm 20 \text{ MeV} \parallel \text{PIDK}(\pi^+) < -5$
All tracks	hasRich	$= 1$

394 3.3 Simulation

395 Several Monte Carlo (MC) samples are used in the analysis for acceptance and background
 396 studies. A full list of them is given in Tab. 3.3. In each case, the decay model includes
 397 a mixture of non-interfering resonances contributing to the $X_s \rightarrow K\pi\pi$ or $X_d \rightarrow \pi\pi\pi$
 398 bachelor system and a non-resonant (phase-space) component. All MC samples are
 399 generated using **Pythia8**, reconstructed using **Reco14c**, **Reco15** and **Reco16** for Run-I,15
 400 and 16 data and selected using the same criteria as in data.

401

402

403 All samples indicated with 'Requested' have been requested in Dec. 17 and are ex-
 pected to be available soon.

Table 3.3: List of simulated samples used in the analysis.

Decay	Event Type	Sim	Statistics				Filter
			11	12	15	16	
$B_s \rightarrow (D_s \rightarrow KK\pi)K\pi\pi$	13266007	08i	1.2 M	1.2 M	-	-	Generator Level
$B_s \rightarrow (D_s \rightarrow KK\pi)K\pi\pi$	13266008	09c	Requested	Requested	Requested	Requested	Generator Level, Stripping
$B_s \rightarrow (D_s \rightarrow K\pi\pi)K\pi\pi$	13266058	09c	Requested	Requested	Requested	Requested	Generator Level, Stripping
$B_s \rightarrow (D_s \rightarrow \pi\pi\pi)K\pi\pi$	13266038	09c	Requested	Requested	Requested	Requested	Generator Level, Stripping
$B_s \rightarrow (D_s \rightarrow KK\pi)\pi\pi\pi$	13266006	08i	1.2 M	1.2 M	-	-	Generator Level
$B_s \rightarrow (D_s \rightarrow KK\pi)\pi\pi\pi$	13266068	09c	Requested	Requested	Requested	Requested	Generator Level, Stripping
$B_s \rightarrow (D_s \rightarrow K\pi\pi)\pi\pi\pi$	13266088	09c	Requested	Requested	Requested	Requested	Generator Level, Stripping
$B_s \rightarrow (D_s \rightarrow \pi\pi\pi)\pi\pi\pi$	13266078	09c	Requested	Requested	Requested	Requested	Generator Level, Stripping
$B_s \rightarrow D_s^* \pi\pi\pi, D_s \rightarrow KK\pi$	13266201	08i	1.2 M	1.2 M	-	-	Generator Level

4 Yields determination

An extended unbinned maximum likelihood fit to the reconstructed B_s mass of the selected events is performed in order to determine the signal and background yields. The invariant mass $m(D_s h\pi\pi)$ is determined from a DTF constraining the mass of the D_s to the PDG value and the position of the PV. The probability density functions (PDFs) used to describe the signal and background components are described in the following.

Due to different mass resolutions, we perform the invariant mass fits simultaneously for each data-taking period and each trigger category. We further introduce four D_s final state categories: $D_s \rightarrow \phi\pi$, $D_s \rightarrow K^*(892)\pi$, $D_s \rightarrow \pi\pi\pi$ and $D_s \rightarrow Kh\pi$ to account for different signal purities. The $D_s \rightarrow Kh\pi$ category combines the two D_s decay channels with the lowest statistics: $D_s \rightarrow KK\pi$ (non-resonant) and $D_s \rightarrow K\pi\pi$. This amounts to 16 categories in total.

4.1 Signal model

The signal B_s -mass distribution of both $B_s^0 \rightarrow D_s K\pi\pi$ and $B_s^0 \rightarrow D_s \pi\pi\pi$ is modeled using a Johnson's SU function [32], which results from a variable transformation of a normal distribution to allow for asymmetric tails:

$$\mathcal{J}(x|\mu, \sigma, \nu, \tau) = \frac{e^{-\frac{1}{2}r^2}}{2\pi \cdot c \cdot \sigma \cdot \tau \cdot \sqrt{z^2 + 1}} \quad (4.1)$$

$$r = -\nu + \frac{\operatorname{asinh}(z)}{\tau} \quad (4.2)$$

$$z = \frac{x - (\mu - c \cdot \sigma \cdot e^\tau \sinh(\nu \cdot \tau))}{c \cdot \tau} \quad (4.3)$$

$$c = \frac{e^{\tau^2} - 1}{2\sqrt{e^{\tau^2} \cdot \cosh(2\nu \cdot \tau) + 1}}. \quad (4.4)$$

It is conveniently expressed in terms of the central moments up to order four: The mean of the distribution μ , the standard deviation σ , the skewness ν and the kurtosis τ . The tail parameters ν and τ are fixed to the values obtained by a fit to the invariant mass distribution of simulated events shown in Fig 4.1. To account for differences between

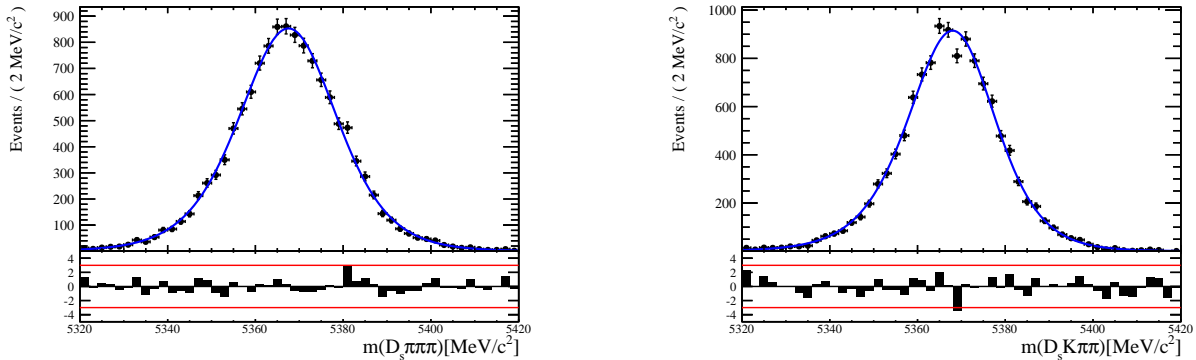


Figure 4.1: Invariant mass distributions of simulated (left) $B_s^0 \rightarrow D_s \pi\pi\pi$ and (right) $B_s^0 \rightarrow D_s K\pi\pi$ events. A fit with a Johnson's SU PDF is overlaid.

424 simulation and real data, linear scaling factors for the mean μ and width σ are determined
425 in the fit to $B_s^0 \rightarrow D_s\pi\pi\pi$ data and later fixed in the fit to $B_s^0 \rightarrow D_sK\pi\pi$ decays. The scale
426 factors are determined separately for each data-taking period and each trigger category.

427 4.2 Background models

428 After the full selection the following residual background components have to be accounted
429 for:

430

431 Combinatorial background

432 The combinatorial background is described by a second order polynomial, whose
433 parameters are determined, for each D_s final state separately, in the fit to data. For
434 systematic studies an exponential PDF is used.

435

436 Peaking B_d background

437 Decays of B_d mesons into the $D_s h\pi\pi$ final state are described by the B_s signal PDF
438 where the mean is shifted by the known mass difference $m_{B_s} - m_{B_d}$ [12].

439

440 Partially reconstructed background

441 Partially reconstructed $B_s^0 \rightarrow D_s^*\pi\pi\pi$ decays, with $D_s^* \rightarrow D_s\gamma$ or $D_s^* \rightarrow D_s\pi^0$, are expected
442 to be peaking lower than signal in the $m(D_s\pi\pi\pi)$ spectrum with large tails due to the
443 momentum carried away by the not reconstructed π^0 or γ . An empirical description for
444 the shape of this contribution is derived from a $B_s^0 \rightarrow D_s^*\pi\pi\pi$ MC sample subject to
445 the nominal $B_s^0 \rightarrow D_s\pi\pi\pi$ selection. Figure 4.2 (left) shows the respective reconstructed
446 $m(D_s\pi\pi\pi)$ distribution. A sum of three bifurcated Gaussian functions (*i.e.* Gaussian
447 functions with different widths on the left and the right side of the maximum value) is used
448 to describe it. In the fit to data, all parameters are fixed to the ones obtained from MC
449 except for the parameter which describes the width of the right tail of the distribution to
450 account for data-simulation differences in mass resolution. The equivalent $B_s^0 \rightarrow D_s^*K\pi\pi$
451 component contributing to the $B_s^0 \rightarrow D_sK\pi\pi$ data sample is described by the same PDF
452 with the right tail fixed to the $B_s^0 \rightarrow D_s\pi\pi\pi$ result.

453 Contributions from $B^0 \rightarrow D_s^*K\pi\pi$ decays are modeled with the $B_s^0 \rightarrow D_s^*K\pi\pi$ PDF
454 shifted by $m_{B_s^0} - m_{B^0}$.

455

456 Misidentified background

457 A small fraction of $B_s \rightarrow D_s^-\pi^+\pi^+\pi^-$ and $B_s^0 \rightarrow D_s^*\pi^+\pi^+\pi^-$ decays, where one of the
458 pions is misidentified as a kaon, contaminate the $B_s^0 \rightarrow D_s K^+\pi^+\pi^-$ sample. To determine
459 the corresponding background shapes, we use simulated events passing the nominal
460 selection except for the PID cuts on the bachelor π^+ tracks. The **PIDCalib** package
461 is used to determine the p_T, η -dependent $\pi^+ \rightarrow K^+$ misidentification probability for
462 each pion. We change the particle hypothesis from pion to kaon for the pion with the
463 higher misidentification probability and recompute the invariant B_s^0 mass, $m(D_s^-\pi_K^+\pi^+\pi^-)$.
464 Similarly, the invariant masses $m(\pi_K^+\pi^+\pi^-)$ and $m(\pi_K^+\pi^-)$ are recomputed and required
465 to be within the considered phasespace region. The background distributions are shown
466 in Fig. 4.2 (middle,right) and modeled by the sum of two Crystal Ball functions. The
467 expected yield of misidentified $B_s^0 \rightarrow D_s\pi\pi\pi$ ($B_s^0 \rightarrow D_s^*\pi^+\pi^+\pi^-$) candidates in the
468 $B_s^0 \rightarrow D_sK\pi\pi$ sample is computed by multiplying the fake rate (within the considered

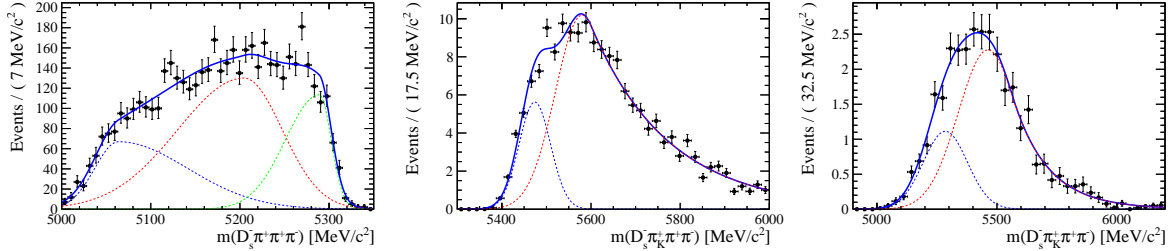


Figure 4.2: Left: Invariant mass distribution of simulated $B_s^0 \rightarrow D_s^* \pi\pi\pi$ events, where the γ/π^0 is excluded from the reconstruction. Middle: Invariant mass distribution of simulated $B_s^0 \rightarrow D_s \pi\pi\pi$ events, where one of the pions is reconstructed as a kaon taking the misidentification probability into account. Right: Invariant mass distribution for simulated $B_s^0 \rightarrow D_s^* \pi\pi\pi$ events, where the γ/π^0 from the D_s^* is excluded from reconstruction and one of the pions is reconstructed as a kaon taking the misidentification probability into account. The fitted PDF is shown in blue.

469 B_s mass range) of 0.47% (0.61%) by the $B_s^0 \rightarrow D_s \pi\pi\pi$ ($B_s^0 \rightarrow D_s^* \pi^+\pi^+\pi^-$) yield as
470 determined in the mass fit to the $B_s^0 \rightarrow D_s \pi\pi\pi$ data sample which is corrected for the
471 PID($\pi^+ < 0$) requirement. The $B_s^0 \rightarrow D_s^* \pi^+\pi^+\pi^-$ yield is additionally corrected for the
472 efficiency of the cut $m(D_s K\pi\pi) > 5200$ MeV evaluated on MC. In the fit to data, the
473 misidentified background yields are fixed to the predicted ones.

474 We consider the $B_s^0 \rightarrow D_s K\pi\pi$ and $B_s^0 \rightarrow D_s^* K\pi\pi$ components contributing to the
475 $B_s^0 \rightarrow D_s \pi\pi\pi$ data sample to be negligible due to the low branching fractions and the
476 tight PID cuts on the bachelor pions.

477 4.3 Results

478 Figure 4.3 shows the invariant mass distribution for $B_s^0 \rightarrow D_s \pi\pi\pi$ and $B_s^0 \rightarrow D_s K\pi\pi$
479 candidates passing all selection criteria. The projections for all categories of the simula-
480 taneous fit are shown in Appendix C together with the results for all fitted parameters.
481 The integrated signal and background yields are listed in Tables 4.1 and 4.2.

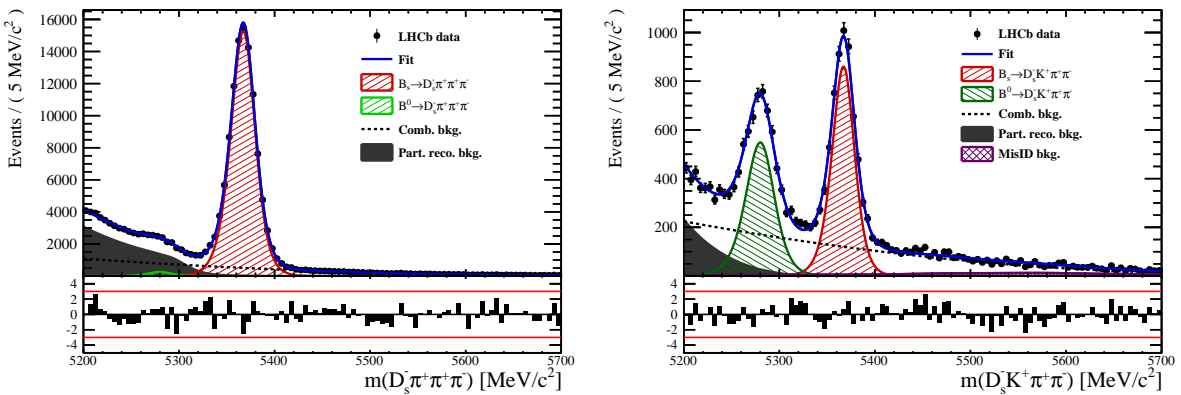


Figure 4.3: Invariant mass distribution of $B_s^0 \rightarrow D_s \pi\pi\pi$ (left) and $B_s^0 \rightarrow D_s K\pi\pi$ (right) candidates.

Table 4.1: Total signal and background yields for the $B_s \rightarrow D_s\pi\pi\pi$ sample (left) and signal yield for the different D_s final states contributing to the $B_s \rightarrow D_s\pi\pi\pi$ sample (right).

Component	Yield		
$B_s \rightarrow D_s\pi\pi\pi$	101289 ± 348		
$B^0 \rightarrow D_s\pi\pi\pi$	2318 ± 1763		
Partially reconstructed bkg.	29817 ± 530		
Combinatorial bkg.	52256 ± 603		
		D_s final state	Signal yield
		$D_s^- \rightarrow \phi^0(1020)\pi^-$	34563 ± 197
		$D_s^- \rightarrow K^{*0}(892)K^-$	28472 ± 189
		$D_s^- \rightarrow (K^-h^+\pi^-)$	21047 ± 160
		$D_s^- \rightarrow \pi^+\pi^-\pi^-$	17208 ± 145

Table 4.2: Total signal and background yields for the $B_s \rightarrow D_sK\pi\pi$ sample (left) and signal yield for the different D_s final states contributing to the $B_s \rightarrow D_sK\pi\pi$ sample (right).

Component	Yield		
$B_s \rightarrow D_sK\pi\pi$	5125 ± 86		
$B^0 \rightarrow D_sK\pi\pi$	4190 ± 92		
Partially reconstructed bkg.	1707 ± 90		
Misidentified bkg.	683 ± 0		
Combinatorial bkg.	9686 ± 162		
		D_s final state	Signal yield
		$D_s^- \rightarrow \phi^0(1020)\pi^-$	1613 ± 47
		$D_s^- \rightarrow K^{*0}(892)K^-$	1527 ± 46
		$D_s^- \rightarrow (K^-h^+\pi^-)$	1128 ± 40
		$D_s^- \rightarrow \pi^+\pi^-\pi^-$	857 ± 37

482 5 Decay-time Resolution

483 The observed oscillation of B mesons is prone to dilution, if the detector resolution is
 484 of similar magnitude as the oscillation period. In the B_s^0 system, considering that the
 485 measured oscillation frequency of the B_s^0 [33] and the average LHCb detector resolution [34]
 486 are both $\mathcal{O}(50 \text{ fs}^{-1})$, this is the case. Therefore, it is crucial to correctly describe the
 487 decay time resolution in order to avoid a bias on the measurement of time dependent CP
 488 violation. Since the time resolution depends on the particular event, especially the decay
 489 time itself, the sensitivity on γ can be significantly improved by using an event dependent
 490 resolution model rather than an average resolution. For this purpose, we use the per-event
 491 decay time error that is estimated based on the uncertainty obtained from the global
 492 kinematic fit of the momenta and vertex positions (DTF) with additional constraints on
 493 the PV position and the D_s mass. In order to apply it correctly, it has to be calibrated.
 494 The raw decay time error distributions for $B_s^0 \rightarrow D_s\pi\pi\pi$ signal candidates are shown in
 495 Figure 5.1 for Run-I and Run-II data. Significant deviations between the two different
 496 data taking periods are observed due to the increase in center of mass energy from Run-I
 497 to Run-II, as well as (among others) new tunings in the pattern and vertex reconstruction.
 498 The decay time error calibration is consequently performed separately for both data taking
 499 periods.

500 For Run-I data, we use the calibration from the closely related $B_s^0 \rightarrow D_s K$ analysis
 501 which was performed on a data sample of prompt- D_s candidates combined with a random
 502 pion track from the PV. We verify the portability to our decay channel on MC.

503 For Run-II data, a new lifetime unbiased stripping line (LTUB) has been implemented
 504 which selects prompt- D_s candidates combined with random $K\pi\pi$ tracks from the PV.

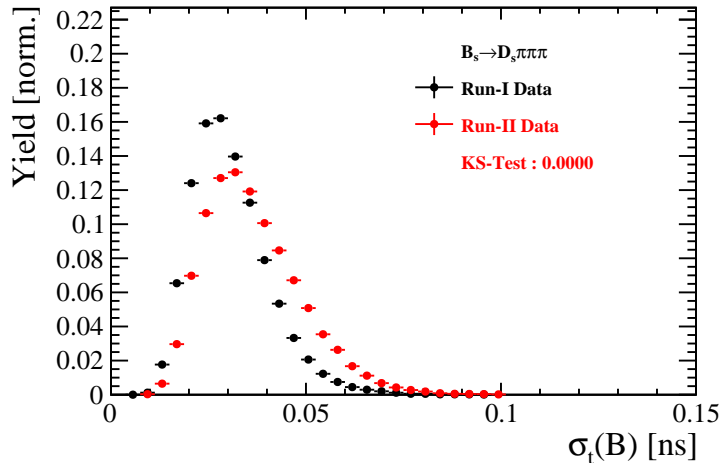


Figure 5.1: Distribution of the decay time error for $B_s^0 \rightarrow D_s\pi\pi\pi$ signal candidates for Run-I (black) and Run-II (red) data (sWeighted).

505 5.1 Calibration for Run-I data

506 For simulated $B_s^0 \rightarrow D_s K \pi\pi$ events, the spread of the differences between reconstructed
 507 decay time and true decay time, $\Delta t = t - t_{true}$, is a direct measure of the decay time
 508 resolution. The sum of two Gaussian pdfs with common mean but different widths is used
 509 to fit the distribution of the decay time difference Δt as shown in Fig. 5.2. The effective
 510 damping of the CP amplitudes due to the finite time resolution is described by the dilution
 511 \mathcal{D} . In the case of infinite precision, there would be no damping and therefore $\mathcal{D} = 1$ would
 512 hold, while for a resolution that is much larger than the B_s^0 oscillation frequency, \mathcal{D} would
 513 approach 0. For a double-Gaussian resolution model, the dilution is given by [35]

$$514 \quad \mathcal{D} = f_1 e^{-\sigma_1^2 \Delta m_s^2 / 2} + (1 - f_1) e^{-\sigma_2^2 \Delta m_s^2 / 2}, \quad (5.1)$$

514 where σ_1 and σ_2 are the widths of the Gaussians, f_1 is the relative fraction of events
 515 described by the first Gaussian relative to the second and Δm_s is the oscillation frequency
 516 of B_s^0 mesons. An effective single Gaussian width is calculated from the dilution as,

$$517 \quad \sigma_{eff} = \sqrt{(-2/\Delta m_s^2) \ln \mathcal{D}}, \quad (5.2)$$

517 which converts the resolution into a single-Gaussian function with an effective resolution
 518 that causes the same damping effect on the magnitude of the B_s oscillation. For the Run-I
 519 $B_s^0 \rightarrow D_s K \pi\pi$ MC sample the effective average resolution is found to be $\sigma_{eff} = 39.1 \pm 0.3$ fs.

520 To analyze the relation between the per-event decay time error δ_t and the actual
 521 resolution σ_t , the simulated $B_s^0 \rightarrow D_s K \pi\pi$ sample is divided into equal-statistics slices of
 522 δ_t . For each slice, the effective resolution is determined as described above. Details of the
 523 fit results in each slice are shown in appendix D. Figure 5.2 shows the obtained values
 524 for σ_{eff} as a function of the per-event decay time error σ_t . To account for the variable
 525 binning, the bin values are not placed at the bin center but at the weighted mean of the
 526 respective per-event-error bin. A linear function is used to parametrize the distribution.
 527 The obtained values are

$$528 \quad \sigma_{eff}^{MC}(\sigma_t) = (0.0 \pm 0.0) \text{ fs} + (1.232 \pm 0.010) \sigma_t \quad (5.3)$$

528 where the offset is fixed to 0. For comparison, the calibration function found for $B_s^0 \rightarrow D_s K$
 529 MC is also shown in Figure 5.2 [35]:

$$529 \quad \sigma_{eff}^{D_s K, MC}(\sigma_t) = (0.0 \pm 0.0) \text{ fs} + (1.201 \pm 0.013) \sigma_t. \quad (5.4)$$

530 Due to the good agreement between the scale factors for $B_s^0 \rightarrow D_s K$ and $B_s^0 \rightarrow D_s K \pi\pi$
 531 MC, we conclude that the resolution calibration for $B_s^0 \rightarrow D_s K$ data:

$$532 \quad \sigma_{eff}^{D_s K}(\sigma_t) = (10.26 \pm 1.52) \text{ fs} + (1.280 \pm 0.042) \sigma_t \quad (5.5)$$

532 can be used for our analysis. The following calibration functions were used in the
 533 $B_s^0 \rightarrow D_s K$ analysis to estimate the systematic uncertainty on the decay-time resolution:

$$534 \quad \sigma_{eff}^{D_s K}(\sigma_t) = (-0.568 \pm 1.570) \text{ fs} + (1.243 \pm 0.044) \sigma_t \quad (5.6)$$

$$534 \quad \sigma_{eff}^{D_s K}(\sigma_t) = (0.0 \pm 0.0) \text{ fs} + (1.772 \pm 0.012) \sigma_t \quad (5.7)$$

535 The difference of the scale factors observed on $B_s^0 \rightarrow D_s K$ and $B_s^0 \rightarrow D_s K \pi\pi$ MC is
 536 assigned as additional systematic uncertainty.

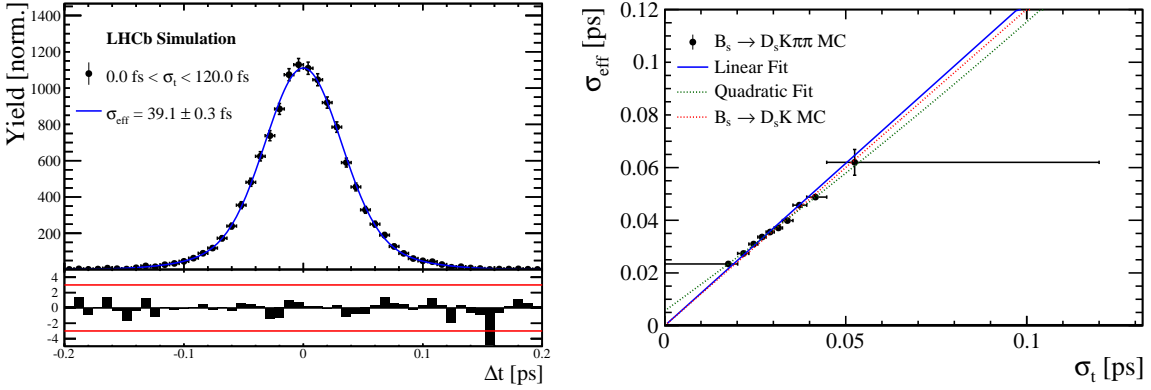


Figure 5.2: (Left) Difference of the true and measured decay time of $B_s^0 \rightarrow D_s K\pi\pi$ MC candidates. (Right) The measured resolution σ_{eff} as function of the per-event decay time error estimate σ_t for $B_s \rightarrow D_s K\pi\pi$ MC (Run-I). The fitted calibration curve is shown in blue.

5.2 Calibration for Run-II data

For the resolution calibration of Run-II data, a sample of promptly produced D_s candidates is selected using the B02DsKPiPiLTUBD2HHHBeauty2CharmLine stripping line. This lifetime-unbiased stripping line does not apply selection requirements related to lifetime or impact parameter, allowing for a study of the resolution. In order to reduce the rate of this sample it is pre-scaled in the stripping. Each D_s candidate is combined with a random kaon track and two random pion tracks which originate from the PV to obtain a sample of fake B_s candidates with a known true decay-time of $t_{true} = 0$. The difference of the measured decay time, t , of these candidates with respect to the true decay time is attributed to the decay time resolution.

The offline selection of the fake B_s candidates is summarized in Tab. 5.1. The selection is similar than the one for real data with the important difference that the D_s candidate is required to come from the PV by cutting on the impact parameter significance. Even after the full selection, a significant number of multiple candidates is observed. These are predominantly fake B_s candidates that share the same D_s candidate combined with different random tracks from the PV. We select one of these multiple candidates randomly which retains approximately 20% of the total candidates. The invariant mass distribution of the selected D_s candidates is shown in Fig. 5.3. To separate true D_s candidates from random combinations, the sPlot method is used to statistically subtract combinatorial background from the sample.

Figure 5.4 shows the sWeighted decay-time distribution for fake B_s candidates. Similar as in the previous section, the decay-time distribution is fitted with a double-Gaussian resolution model in slices of the per-event decay time error. Since some D_s candidates might actually originate from true B_s decays, the decay-time distribution of the fake B_s candidates might show a bias towards positive decay times. Therefore, we determine the decay-time resolution from the negative decay-time distribution only. Details of the fit results in each slice are shown in appendix D. The resulting calibration function:

$$\sigma_{eff}^{Data}(\sigma_t) = (9.7 \pm 1.7) \text{ fs} + (0.915 \pm 0.040) \sigma_t \quad (5.8)$$

⁵⁶⁴ is in good agreement with the one obtained for the $B_s \rightarrow J/\psi\phi$ (Run-II) analysis [36].

$$\sigma_{eff}^{J/\psi\phi}(\sigma_t) = (12.25 \pm 0.33) \text{ fs} + (0.8721 \pm 0.0080) \sigma_t \quad (5.9)$$

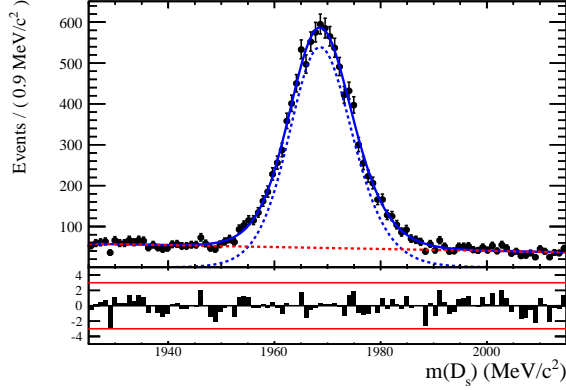


Figure 5.3: The invariant mass distribution for prompt D_s candidates.

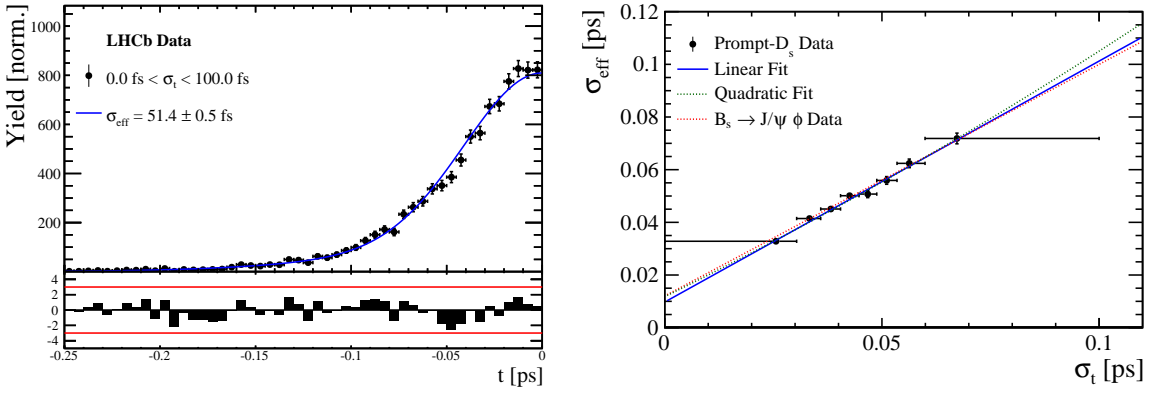


Figure 5.4: (Left) Decay-time distribution for fake B_s candidates from promptly produced D_s candidates, combined with random prompt $K\pi\pi$ bachelor tracks. (Right) The measured resolution σ_{eff} as function of the per-event decay time error estimate σ_t for fake B_s candidates (Run-II data). The fitted calibration curve is shown in blue.

Table 5.1: Offline selection requirements for fake B_s candidates from promptly produced D_s candidates combined with random prompt $K\pi\pi$ bachelor tracks.

	Description	Requirement
$B_s \rightarrow D_s K\pi\pi$	χ^2_{vtx}/ndof	< 8
	χ^2_{DTF}/ndof	< 15
	t	< 0 ps
$D_s \rightarrow hhh$	χ^2_{vtx}/ndof	< 5
	DIRA	> 0.99994
	χ^2_{FD}	> 9
	p_T	> 1800 MeV
	χ^2_{IP}	< 9
	$\chi^2_{IP}(h)$	> 5
	Wrong PV veto	$nPV = 1 \parallel \min(\Delta\chi^2_{IP}) > 20$
$D_s^- \rightarrow KK\pi^-$	D^0 veto	$m(KK) < 1840$ MeV
	D^- veto	$m(K^+K_\pi^-\pi^-) \neq m(D^-) \pm 30$ MeV
	Λ_c veto	$m(K^+K_p^-\pi^-) \neq m(\Lambda_c) \pm 30$ MeV
$D_s^- \rightarrow \phi\pi^-$	$m(KK)$	$= m_\phi \pm 20$ MeV
	PIDK(K^+)	> -10
	PIDK(K^-)	> -10
	PIDK(π^-)	< 20
$D_s^- \rightarrow K^*(892)K^-$	$m(KK)$	$\neq m_\phi \pm 20$ MeV
	$m(K^+\pi^-)$	$= m_{K^*(892)} \pm 75$ MeV
	PIDK(K^+)	> -10
	PIDK(K^-)	> -5
	PIDK(π^-)	< 20
$D_s^- \rightarrow (KK\pi^-)_{NR}$	$m(KK)$	$\neq m_\phi \pm 20$ MeV
	$m(K^+\pi^-)$	$\neq m_{K^*(892)} \pm 75$ MeV
	PIDK(K^+)	> 5
	PIDK(K^-)	> 5
	PIDK(π^-)	< 10
$D_s \rightarrow \pi\pi\pi$	PIDK(h)	< 10
	PIDp(h)	< 10
	D^0 veto	$m(\pi^+\pi^-) < 1700$ MeV
$X_s \rightarrow K\pi\pi$	$\chi^2_{IP}(h)$	< 40
	PIDK(K)	> 10
	PIDK(π)	< 5
	isMuon(h)	False
All tracks	p_T	> 500 MeV

565 6 Acceptance

566 6.1 MC corrections

567 6.1.1 Truth matching of simulated candidates

568 We use the `BackgroundCategory` tool to truth match our simulated candidates. Candidates
 569 with background category (`BKGCAT`) 20 or 50 are considered to be true signal. Background
 570 category 60 is more peculiar since it contains both badly reconstructed signal candidates
 571 and ghost background. This is due to the fact that the classification algorithms identifies
 572 all tracks for which less than 70% of the reconstructed hits are matched to generated
 573 truth-level quantities as ghosts. In particular for signal decays involving many tracks (as
 574 in our case), this arbitrary cutoff is not 100% efficient. Moreover, the efficiency is expected
 575 to depend on the kinematics which would lead to a biased acceptance determination if
 576 candidates with `BKGCAT`= 60 would be removed. We therefore include `BKGCAT`= 60 and
 577 statistically subtract the ghost background by using the `sPlot` technique. The `sWeights`
 578 are calculated from a fit to the reconstructed B_s mass. The signal contribution is modeled
 579 as described in Sec. 4.1 and the background with a polynomial. The fit is performed
 580 simultaneously in two categories; the first includes events with `BKGCAT` = 20 or 50 and
 581 the second events with `BKGCAT` = 60. To account for the different mass resolution we
 582 use a different σ for each category, while the mean and the tail parameters are shared
 583 between them. The background component is only included for the second category.

584 A significant fraction of 8% of the true signal candidates are classified as ghosts, while
 585 only 20% of the events classified with `BKGCAT`= 60 are indeed genuine ghosts.

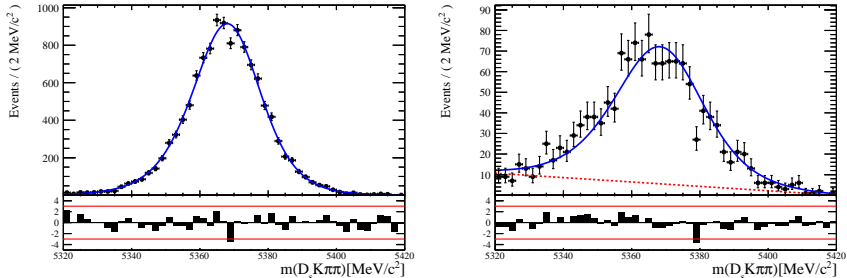


Figure 6.1: The reconstructed B_s mass distribution for simulated $B_s \rightarrow D_s K\pi\pi$ decays classified with `BKGCAT` = 20 or 50 (left) and `BKGCAT` = 60 (right) after the full selection.

586 6.1.2 Correction of data-simulation differences

587 For the evaluation of phase space efficiency and to a lesser extend also the decay-time
 588 efficiency we rely on simulated data as discussed in the following sections. A number
 589 of data-driven corrections are applied to the MC samples to account for known data-
 590 simulation differences. The MC sample is reweighted to match the two-dimensional p_T and
 591 η distribution observed on real data. An additional reweighting of the track multiplicity
 592 is applied on top of that. These corrections are derived from the calibration channel
 593 $B_s \rightarrow D_s \pi\pi\pi$ and applied to both the signal and calibration channel MC samples. The
 594 distributions before and after reweighting are shown in Appendix H. We use the `PIDCorr`
 595 tool to correct the simulated PID responses based on PID calibration samples [37].

596 6.2 Decay-time acceptance

597 The decay-time distribution of the B_s^0 mesons is sculpted due to the geometry of the LHCb
 598 detector and the applied selection cuts, which are described in Section 3. In particular, any
 599 requirement on the flight distance, the impact parameter or the direction angle (DIRA)
 600 of the B_s^0 mesons, as well as the direct cut on the proper-time, will lead to a decay-time
 601 dependent efficiency $\epsilon(t)$.

602 We use a combination of control channels to derive the acceptance function $\epsilon(t)$,
 603 because for $B_s^0 \rightarrow D_s K\pi\pi$ decays the decay-time acceptance is strongly correlated with
 604 the CP -observables which we aim to measure. Therefore, extracting the CP -observables
 605 and the acceptance shape at the same time is not possible. A fit to the decay-time
 606 distribution of $B_s^0 \rightarrow D_s \pi\pi\pi$ candidates is performed and the obtained acceptance shape
 607 is corrected for the small difference observed between the $B_s^0 \rightarrow D_s K\pi\pi$ and $B_s^0 \rightarrow D_s \pi\pi\pi$
 608 MC samples. In addition, we include the control channel $B^0 \rightarrow D_s K\pi\pi$ to increase
 609 the statistical precision. A simultaneous fit to the four datasets ($B_s^0 \rightarrow D_s \pi\pi\pi$ data,
 610 $B^0 \rightarrow D_s K\pi\pi$ data, $B_s^0 \rightarrow D_s K\pi\pi$ MC and $B_s^0 \rightarrow D_s \pi\pi\pi$ MC) is performed to allow for
 611 a straightforward propagation of uncertainties. In each case, a PDF of the following form

$$\mathcal{P}(t, \delta t) = \left[e^{-\Gamma t} \cdot \cosh\left(\frac{\Delta\Gamma t'}{2}\right) \otimes \mathcal{R}(t - t', \delta t) \right] \cdot \epsilon(t), \quad (6.1)$$

612 is used to describe the decay-time distribution. For real data, the values for $\Gamma_{s,d}$ and
 613 $\Delta\Gamma_{s,d}$ are fixed to the latest HFAG results [38], while for simulated data, the generated
 614 values are used. A single Gaussian resolution function $\mathcal{R}(t - t', \delta t)$ is used where the
 615 decay-time error estimate is scaled with the respective calibration functions determined in
 616 Sec. 5. Each decay-time acceptance $\epsilon(t)$ is modeled using cubic splines, allowing for the
 617 analytical computation of the decay-time integrals appearing in the PDF [39]. The splines
 618 are parametrized by so-called knots (t_0, t_1, \dots, t_N) which determine their boundaries. Two
 619 knots are located by default at the lower and upper edge of the interval allowed for the
 620 decay time, the remaining ones are chosen such that there is an approximately equal
 621 amount of data in-between two consecutive knots. In the basis of cubic b-splines, $b_i(t)$,
 622 the acceptance is then constructed as:

$$\epsilon(t) = \sum_{i=0}^N v_i b_i(t) \quad (6.2)$$

623 where the spline coefficients v_i are determined from the fit. We fix coefficient v_{N-1} to unity
 624 in order to normalize the overall acceptance function. To stabilize the upper decay-time
 625 acceptance, v_N is fixed by a linear extrapolation from the two previous coefficients:

$$v_N = v_{N-1} + \frac{v_{N-2} - v_{N-1}}{t_{N-2} - t_{N-1}} \cdot (t_N - t_{N-1}). \quad (6.3)$$

626 It was found that at least $N = 6$ knots are necessary for a sufficient fit quality.

627 Three distinct splines are used in the following combinations to describe the acceptances
628 for the four datasets:

- 629 • $B_s^0 \rightarrow D_s K\pi\pi$ MC: $\epsilon_{D_s K\pi\pi}^{MC}(t)$
630 • $B_s^0 \rightarrow D_s \pi\pi\pi$ MC: $\epsilon_{D_s \pi\pi\pi}^{MC}(t) = R(t) \cdot \epsilon_{D_s K\pi\pi}^{MC}(t)$
631 • $B_s^0 \rightarrow D_s \pi\pi\pi$ data: $\epsilon_{D_s \pi\pi\pi}^{Data}(t) = R(t) \cdot \epsilon_{D_s K\pi\pi}^{Data}(t)$
632 • $B^0 \rightarrow D_s K\pi\pi$ data: $\epsilon_{D_s K\pi\pi}^{Data}(t)$

633 where $\epsilon_{D_s K\pi\pi}^{MC}(t)$ represents the acceptance in $B_s^0 \rightarrow D_s K\pi\pi$ MC, $R(t)$ represents the
634 ratio of acceptances in $B_s^0 \rightarrow D_s \pi\pi\pi$ and $B_s^0 \rightarrow D_s K\pi\pi$ MC and the final acceptance in
635 $B_s^0 \rightarrow D_s K\pi\pi$ data is represented by $\epsilon_{D_s K\pi\pi}^{Data}(t)$.

636 The acceptances are determined separately for each data-taking period and each
637 trigger category as discussed in more detail in Appendix E. The fit results are shown in
638 Figs. 6.2 to 6.5 and the fitted parameters are summarized in Tables 6.1 to 6.4.

639

640

641 As currently there are no Run-II MC samples available, we use the Run-I MC
samples also for the Run-II fits. An alternative approach would be to fit only the
 $B^0 \rightarrow D_s K\pi\pi$ data sample in order to remove the MC dependency. The final strat-
egy will be fixed, depending on the MC availability, during the review.

Table 6.1: Time acceptance parameters for events in category [Run-I,L0-TOS].

Knot position	Coefficient	$B_s^0 \rightarrow D_s K\pi\pi$ data	$B_s^0 \rightarrow D_s K\pi\pi$ MC	Ratio
0.4	v_0	0.592 ± 0.038	0.542 ± 0.021	0.972 ± 0.056
0.8	v_1	0.805 ± 0.057	0.781 ± 0.033	0.915 ± 0.064
1.6	v_2	0.852 ± 0.077	0.917 ± 0.051	1.034 ± 0.080
2.5	v_3	1.117 ± 0.042	1.108 ± 0.029	0.955 ± 0.045
6.5	v_4	1.0 (fixed)	1.0 (fixed)	1.0 (fixed)
10.0	v_5	0.898 (interpolated)	0.906 (interpolated)	1.039 (interpolated)

Table 6.2: Time acceptance parameters for events in category [Run-I,L0-TIS].

Knot position	Coefficient	$B_s^0 \rightarrow D_s K\pi\pi$ data	$B_s^0 \rightarrow D_s K\pi\pi$ MC	Ratio
0.4	v_0	0.417 ± 0.038	0.415 ± 0.021	0.948 ± 0.077
0.8	v_1	0.623 ± 0.060	0.654 ± 0.035	0.873 ± 0.080
1.6	v_2	0.901 ± 0.097	0.976 ± 0.061	0.909 ± 0.087
2.5	v_3	1.095 ± 0.052	1.076 ± 0.035	1.003 ± 0.051
6.5	v_4	1.0 (fixed)	1.0 (fixed)	1.0 (fixed)
10.0	v_5	0.917 (interpolated)	0.933 (interpolated)	0.998 (interpolated)

Table 6.3: Time acceptance parameters for events in category [Run-II,L0-TOS].

Knot position	Coefficient	$B_s^0 \rightarrow D_s K\pi\pi$ data	$B_s^0 \rightarrow D_s K\pi\pi$ MC	Ratio
0.4	v_0	0.568 ± 0.028	0.496 ± 0.015	0.965 ± 0.044
0.8	v_1	0.787 ± 0.043	0.738 ± 0.024	0.892 ± 0.049
1.6	v_2	0.899 ± 0.061	0.943 ± 0.039	0.984 ± 0.059
2.5	v_3	1.079 ± 0.030	1.093 ± 0.021	0.979 ± 0.030
6.5	v_4	1.0 (fixed)	1.0 (fixed)	1.0 (fixed)
10.0	v_5	0.931 (interpolated)	0.919 (interpolated)	1.018 (interpolated)

Table 6.4: Time acceptance parameters for events in category [Run-II,L0-TIS].

Knot position	Coefficient	$B_s^0 \rightarrow D_s K\pi\pi$ data	$B_s^0 \rightarrow D_s K\pi\pi$ MC	Ratio
0.4	v_0	0.389 ± 0.009	0.506 ± 0.015	0.908 ± 0.031
0.8	v_1	0.592 ± 0.013	0.744 ± 0.024	0.896 ± 0.035
1.6	v_2	0.798 ± 0.052	0.965 ± 0.041	0.927 ± 0.054
2.5	v_3	1.111 ± 0.035	1.112 ± 0.023	0.941 ± 0.039
6.5	v_4	1.0 (fixed)	1.0 (fixed)	1.0 (fixed)
10.0	v_5	0.903 (interpolated)	0.902 (interpolated)	1.052 (interpolated)

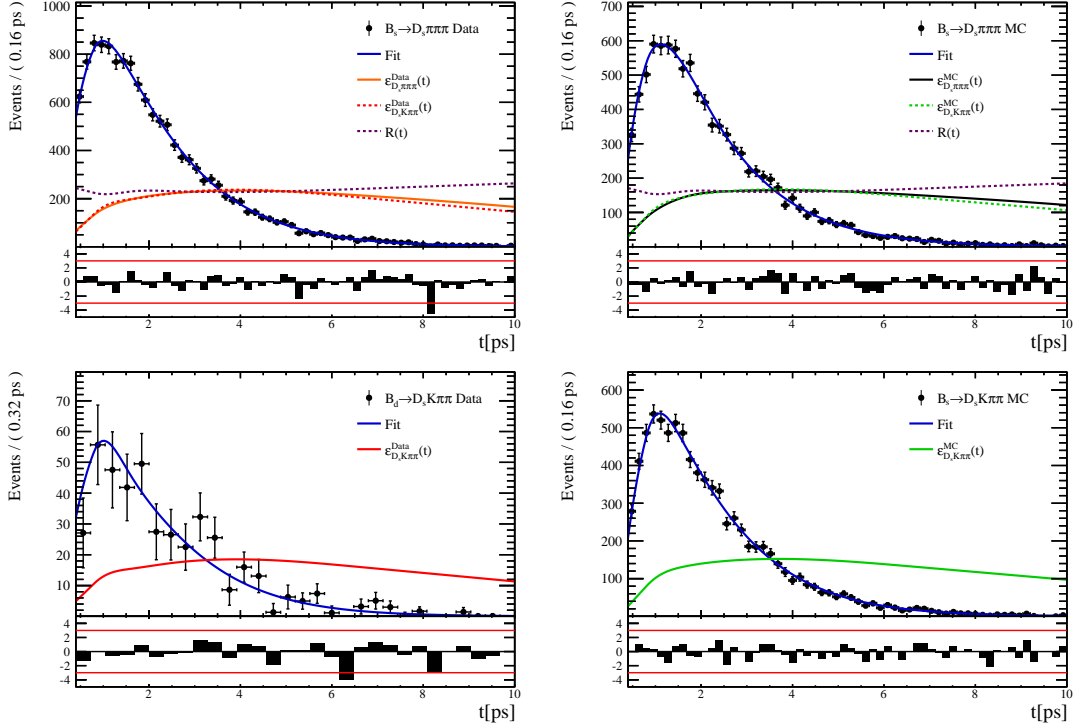


Figure 6.2: Decay-time fit projections for $B_s^0 \rightarrow D_s\pi\pi\pi$ data (top-left), $B_s^0 \rightarrow D_s\pi\pi\pi$ MC (top-right), $B_s^0 \rightarrow D_sK\pi\pi$ data (bottom-left) and $B_s^0 \rightarrow D_sK\pi\pi$ MC (bottom-right) in category [Run-I,L0-TOS]. The respective acceptance function is overlaid in an arbitrary scale.

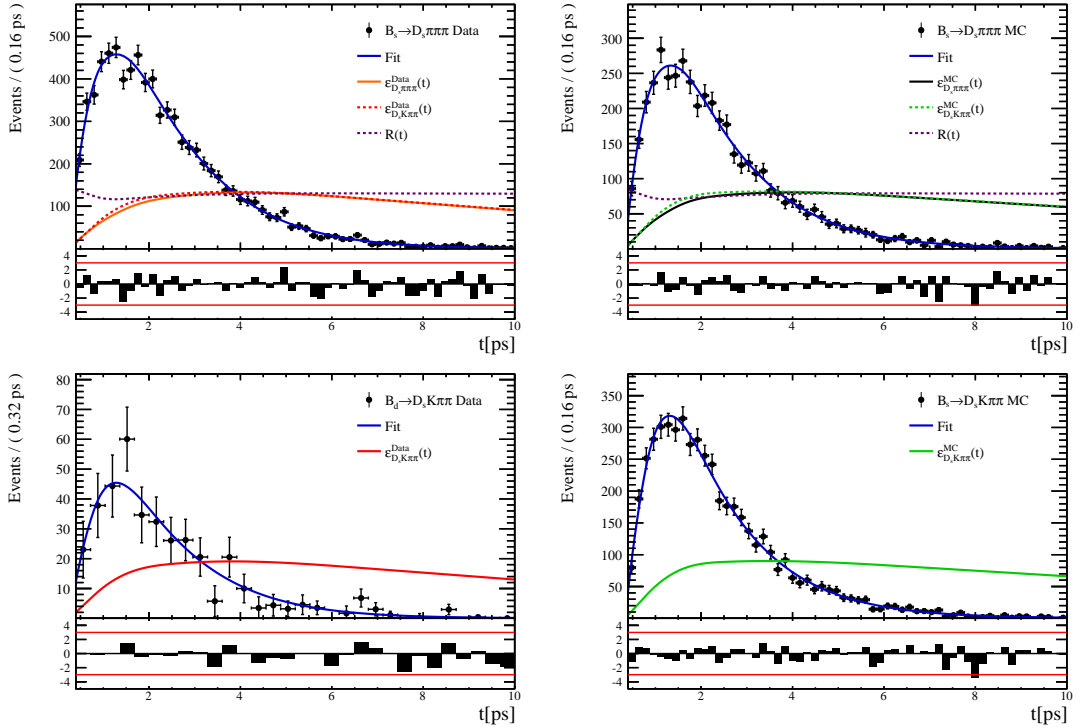


Figure 6.3: Decay-time fit projections for $B_s^0 \rightarrow D_s\pi\pi\pi$ data (top-left), $B_s^0 \rightarrow D_s\pi\pi\pi$ MC (top-right), $B_s^0 \rightarrow D_sK\pi\pi$ data (bottom-left) and $B_s^0 \rightarrow D_sK\pi\pi$ MC (bottom-right) in category [Run-I,L0-TIS]. The respective acceptance function is overlaid in an arbitrary scale.

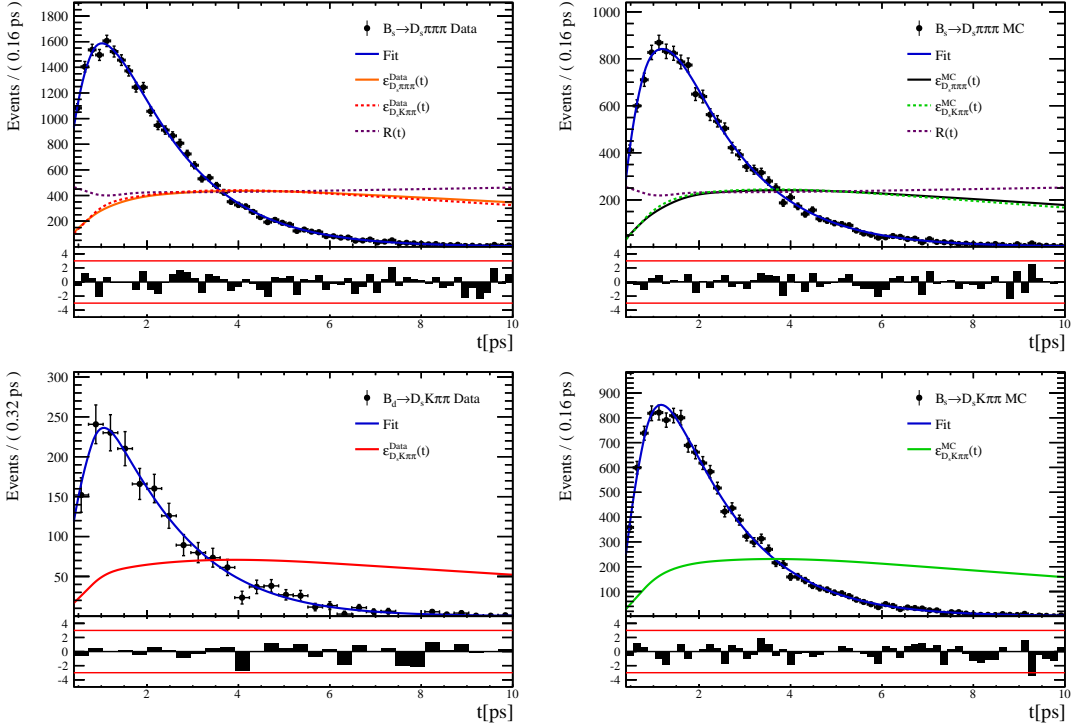


Figure 6.4: Decay-time fit projections for $B_s^0 \rightarrow D_s \pi\pi\pi$ data (top-left), $B_s^0 \rightarrow D_s \pi\pi\pi$ MC (top-right), $B^0 \rightarrow D_s K\pi\pi$ data (bottom-left) and $B_s^0 \rightarrow D_s K\pi\pi$ MC (bottom-right) in category [Run-II,L0-TOS]. The respective acceptance function is overlaid in an arbitrary scale.

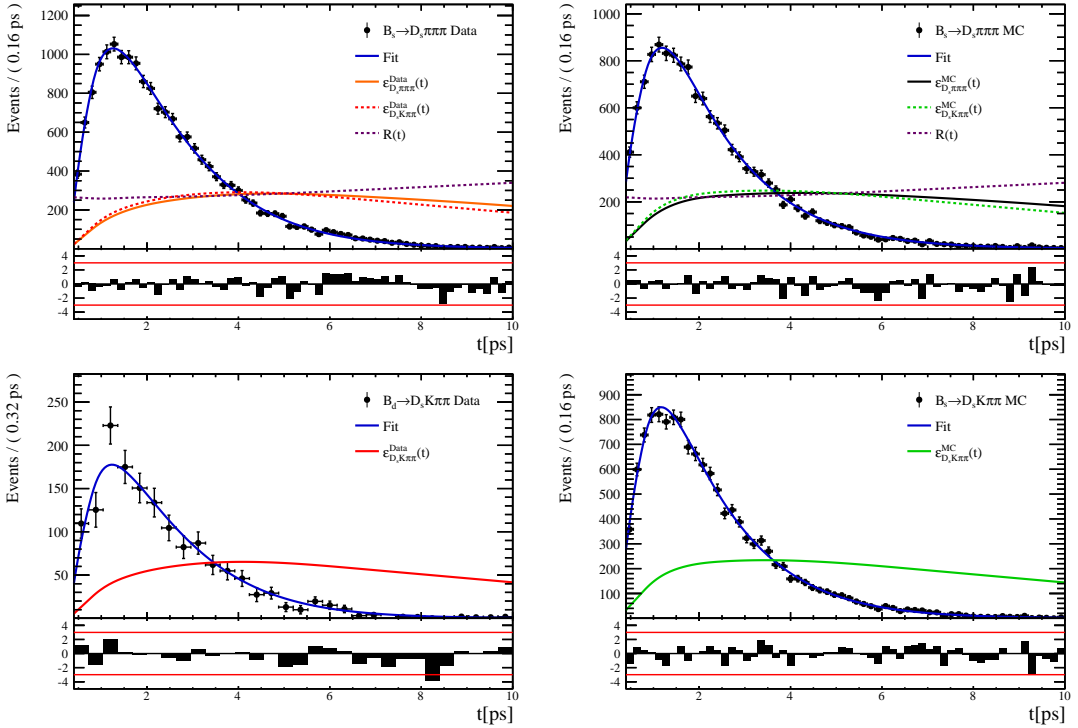


Figure 6.5: Decay-time fit projections for $B_s^0 \rightarrow D_s \pi\pi\pi$ data (top-left), $B_s^0 \rightarrow D_s \pi\pi\pi$ MC (top-right), $B^0 \rightarrow D_s K\pi\pi$ data (bottom-left) and $B_s^0 \rightarrow D_s K\pi\pi$ MC (bottom-right) in category [Run-II,L0-TIS]. The respective acceptance function is overlaid in an arbitrary scale.

642 6.3 Phase space acceptance

643 The signal PDF used for the full time-dependent amplitude fit can be written in terms of
 644 the differential decay rate from Equation 2.29 as

$$\mathcal{P}(\mathbf{x}, t, g, f) = \frac{\left(\frac{d\Gamma(\mathbf{x}, t, q, f)}{dt d\Phi_4} \right) \cdot \epsilon(\mathbf{x}) \cdot \epsilon(t)}{\int \sum_{q,f} \left(\frac{d\Gamma(\mathbf{x}, t, q, f)}{dt d\Phi_4} \right) \cdot \epsilon(\mathbf{x}) \cdot \epsilon(t) dt d\Phi_4} \quad (6.4)$$

645 where $\epsilon(\mathbf{x})$ is the phase-space efficiency. Note that the efficiency in the numerator appears
 646 as an additive constant in the log \mathcal{L} that does not depend on any fit parameters such that it
 647 can be ignored. However, the efficiency function still enters via the normalization integrals.
 648 In contrast to the time integrals which can be performed analytically as discussed in
 649 Sec. 6.2, the phase-space integrals are determined numerically. For this purpose, we use
 650 simulated events generated with **EVTGEN**, pass them through the full detector simulation
 651 and apply the same selection criteria as for data in order to perform the MC integrals. As
 652 an example, the integral of the total $b \rightarrow c$ amplitude squared can be approximated as

$$\int |\mathcal{A}_f^c(\mathbf{x})|^2 \epsilon(\mathbf{x}) d\Phi_4 \approx \frac{1}{N_{MC}} \sum_k^{N_{MC}} \frac{|\mathcal{A}_f^c(\mathbf{x}_k)|^2}{|A'(\mathbf{x}_k)|^2} \quad (6.5)$$

653 where A' labels the amplitude model used for the generation and x_k is the k -th MC
 654 event. As a result, the phase-space efficiency can be included in the fit without explicitly
 655 modeling it.

656

657

Disclaimer: At the moment there is only a small Run-I MC sample available where a DecFile (EventType: 13266007) was used from which we were not able to reproduce the generator pdf A' . We can therefore not follow our preferred procedure described above. An alternative, provisionally method is briefly described in the following.

658

659 We use a BDTG to map the five-dimensional phase space to an one-dimensional distribution
 660 [40]. The BDTG is trained to learn the differences between the selected MC and a generator
 661 level MC sample. As discriminating variables, five invariant mass combinations are used
 662 as shown in Fig. 6.6. Based on the classifier output distributions, shown in Fig. 6.7, an
 663 efficiency as function of the BDTG response is derived.

664 A large toy MC sample is generated (500 k events) according to a preliminary amplitude
 665 model $A'(\mathbf{x})$ and for each event a weight, depending on the BDTG response (see Fig. 6.7),
 666 is assigned to account for the efficiency variation across phase space. This reweighted toy
 667 MC sample is then effectively distributed as $A'(\mathbf{x}) \cdot \epsilon(\mathbf{x})$ and can be used to calculate the
 668 normalization integrals in Equation 6.5. Figure 6.8 compares the phase space efficiency
 669 obtained from the reweighed toy MC sample with the 'true' efficiency given by the ratio of
 670 selected and generated MC events. A fairly good agreement is observed in all dimensions.

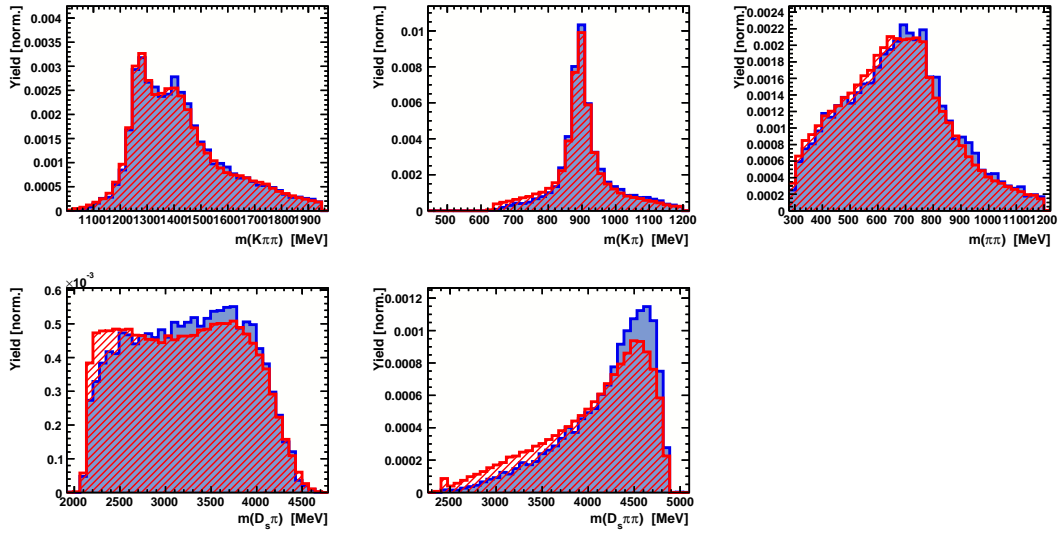


Figure 6.6: Discriminating variables used to train the BDTG. The selected MC sample is shown in blue and the generator MC sample in red.

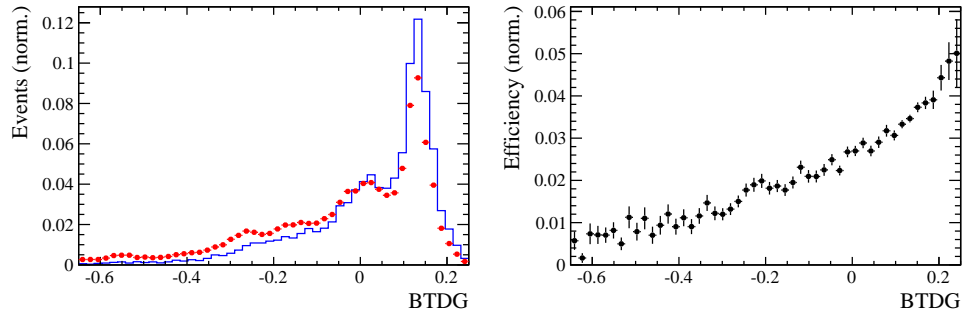


Figure 6.7: Left: Output distributions of the BDTG for the simulated MC sample (blue) and the generator level sample (red). Right: Phase space efficiency as function of the BDTG response computed as the ratio of selected and generated decays.

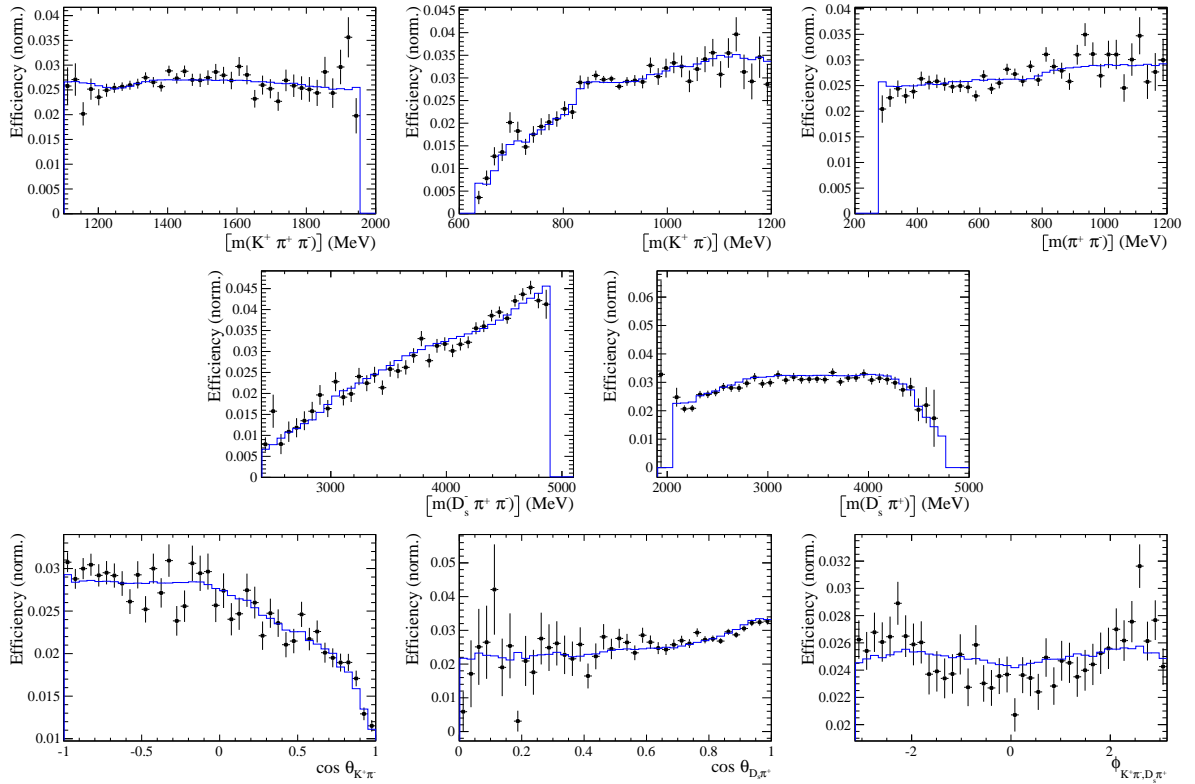


Figure 6.8: Efficiency variation as a function of the phase-space variables obtained from the ratio of selected and generated MC events (data points) and efficiency obtained from a reweighted toy MC sample (blue).

7 Flavour Tagging

To identify the initial flavour state of the B_s^0 meson, a number of flavour tagging algorithms are used that either determine the flavour of the non-signal b-hadron produced in the event (opposite site, OS [41]) or use particles produced in the fragmentation of the signal candidate B_s^0/\bar{B}_s^0 (same side, SS [42]). For the same side, the algorithm searching for the charge of an additional kaon that accompanies the fragmentation of the signal candidate is used (SS-Kaon). For the opposite site, four different taggers are chosen: the algorithms that use the charge of an electron or a muon from semi-leptonic B decays (OS- e,μ), the tagger that uses the charge of a kaon from a $b \rightarrow c \rightarrow s$ decay chain (OS-nnetKaon) and the algorithm that determines the B_s^0/\bar{B}_s^0 candidate flavour from the charge of a secondary vertex, reconstructed from the OS b decay product (OS-VtxCharge).

Every tagging algorithm is prone to misidentify the signal candidate at a certain mistag rate ω . This might be caused by particle misidentification, flavour oscillation of the neutral opposite site B-meson or by tracks that are wrongly picked up from the underlying event. An imperfect determination of the B_s^0 production flavor dilutes the observed CP asymmetry by a factor $D_{tag} = 1 - 2\omega$. This means that the statistical precision, with which the CP asymmetry can be measured, scales as the inverse square root of the effective tagging efficiency:

$$\epsilon_{eff} = \epsilon_{tag}(1 - 2\omega)^2, \quad (7.1)$$

where ϵ_{tag} is the fraction of tagged candidates.

For each B_s^0/\bar{B}_s^0 candidate, the tagging algorithms provide, besides a flavour tag $q = 1, -1, 0$ (for an initial B_s^0 , \bar{B}_s^0 or no tag), a prediction for the mistag probability η based on the output of multivariate classifiers. These are trained on simulated samples of flavour specific control channels ($B_s^0 \rightarrow D_s^- \pi^+$ (SS algorithm) and $B^+ \rightarrow J/\psi K^+$ (OS algorithms)) and are optimized for highest ϵ_{eff} on data. Utilizing flavour-specific final states, the estimated mistag η of each tagger has to be calibrated to match the actual mistag probability ω . For the calibration, a linear model

$$\omega(\eta) = p_0 + p_1 \cdot (\eta - \langle \eta \rangle), \quad (7.2)$$

is used where $\langle \eta \rangle$ is the average estimated mistag probability. A perfectly calibrated tagger would lead to $\omega(\eta) = \eta$ and one would expect $p_1 = 1$ and $p_0 = \langle \eta \rangle$. Due to the different interaction cross-sections of oppositely charged particles, the tagging calibration parameters depend on the initial state flavour of the B_s^0 . Therefore, the flavour asymmetry parameters Δp_0 , Δp_1 and $\Delta \epsilon_{tag}$ are introduced.

7.1 OS tagger combination

First, the OS electron, muon, neural net kaon and the secondary vertex charge taggers are individually calibrated and then combined into a single OS-Combo tagger using the `EspressoPerformanceMonitor` tool. We choose the flavour specific decay $B_s \rightarrow D_s \pi \pi \pi$ as calibration mode since it is very similar to the signal decay $B_s \rightarrow D_s K \pi \pi$. The calibration is performed separately for Run-I and Run-II data. Where available the latest Run-II tuning is used for Run-II data, otherwise the Run-I tuning of the taggers is used. Figures 7.1 and 7.2 show the fitted calibration functions and Tables 7.1 and 7.2 list the measured tagging performances.

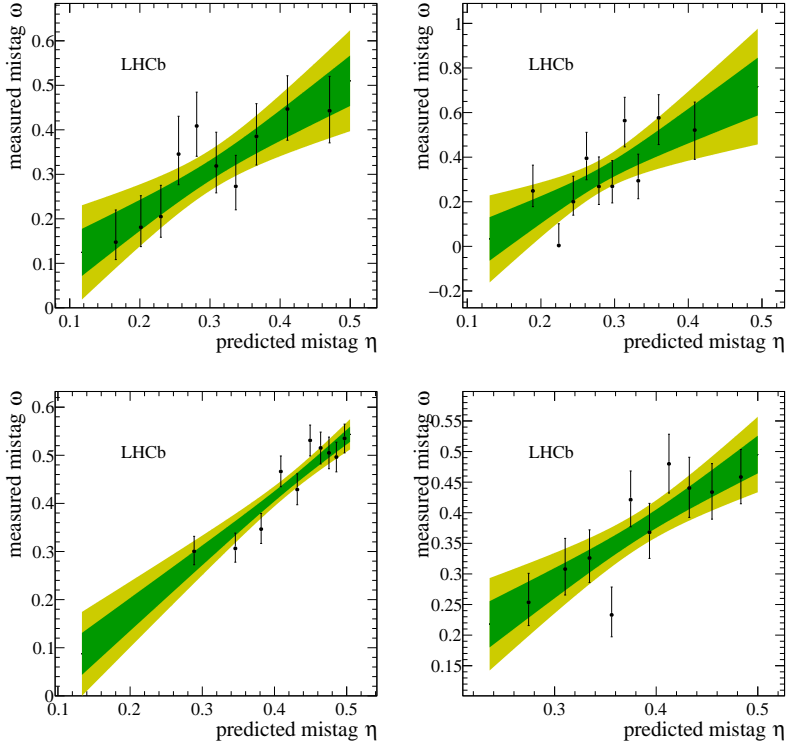


Figure 7.1: Predicted versus measured mistag probability for the (top left) OS muon, (top right) OS electron, (bottom left) OS kaon and (bottom right) OS vertex charge tagger for Run-I. A linear fit, including the 1σ and 2σ error bands is overlaid for each tagger.

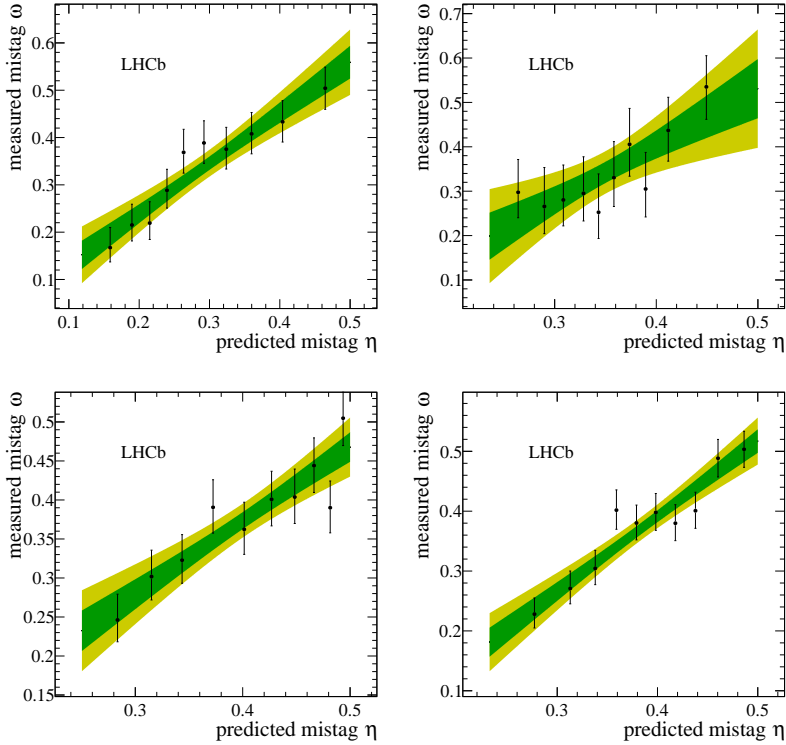


Figure 7.2: Predicted versus measured mistag probability for the (top left) OS muon, (top right) OS electron, (bottom left) OS kaon and (bottom right) OS vertex charge tagger for Run-II. A linear fit, including the 1σ and 2σ error bands is overlaid for each tagger.

Table 7.1: The flavour tagging performances for the used OS taggers for Run-I data.

Tagger	ϵ	ω	$\epsilon \langle D^2 \rangle = \epsilon (1 - 2\omega)^2$
OS μ	$(8.775 \pm 0.207)\%$	$(28.935 \pm 0.180(\text{stat}) \pm 2.288(\text{cal}))\%$	$(1.558 \pm 0.045(\text{stat}) \pm 0.338(\text{cal}))\%$
OS e	$(3.191 \pm 0.129)\%$	$(28.778 \pm 0.366(\text{stat}) \pm 3.636(\text{cal}))\%$	$(0.575 \pm 0.031(\text{stat}) \pm 0.197(\text{cal}))\%$
OS K NN	$(32.099 \pm 0.342)\%$	$(38.405 \pm 0.094(\text{stat}) \pm 1.152(\text{cal}))\%$	$(1.726 \pm 0.033(\text{stat}) \pm 0.343(\text{cal}))\%$
Vertex Charge	$(21.797 \pm 0.302)\%$	$(35.672 \pm 0.092(\text{stat}) \pm 1.480(\text{cal}))\%$	$(1.790 \pm 0.034(\text{stat}) \pm 0.370(\text{cal}))\%$

Table 7.2: The flavour tagging performances for the used OS taggers for Run-II data.

Tagger	ϵ	ω	$\epsilon \langle D^2 \rangle = \epsilon (1 - 2\omega)^2$
OS μ	$(8.904 \pm 0.146)\%$	$(30.119 \pm 0.119(\text{stat}) \pm 1.477(\text{cal}))\%$	$(1.408 \pm 0.029(\text{stat}) \pm 0.209(\text{cal}))\%$
OS e	$(3.284 \pm 0.091)\%$	$(32.834 \pm 0.166(\text{stat}) \pm 2.367(\text{cal}))\%$	$(0.387 \pm 0.013(\text{stat}) \pm 0.107(\text{cal}))\%$
OS K NN	$(16.709 \pm 0.191)\%$	$(35.960 \pm 0.075(\text{stat}) \pm 1.076(\text{cal}))\%$	$(1.317 \pm 0.021(\text{stat}) \pm 0.202(\text{cal}))\%$
Vertex Charge	$(20.605 \pm 0.208)\%$	$(34.625 \pm 0.077(\text{stat}) \pm 0.967(\text{cal}))\%$	$(1.948 \pm 0.028(\text{stat}) \pm 0.245(\text{cal}))\%$

7.2 Tagging performance

The OS-Combo and SS-Kaon taggers are calibrated simultaneously by fitting the $B_s \rightarrow D_s \pi\pi\pi$ decay-time distribution as discussed in Sec. 9. In this fit, the predicted mistag probabilities η_{OS} and η_{SS} , shown Fig. 7.3 for $B_s \rightarrow D_s \pi\pi\pi$ and $B_s \rightarrow D_s K\pi\pi$ data, are included as per-event observables, effectively giving a larger weight to the events that have a lower mistag probability. The tagger responses are combined into a single response on an event-by-event basis during the fit. Tables 7.3 and 7.4 report the tagging performances for the OS and SS combination considering three mutually exclusive categories of tagged events: OS only, SS only and both OS and SS.

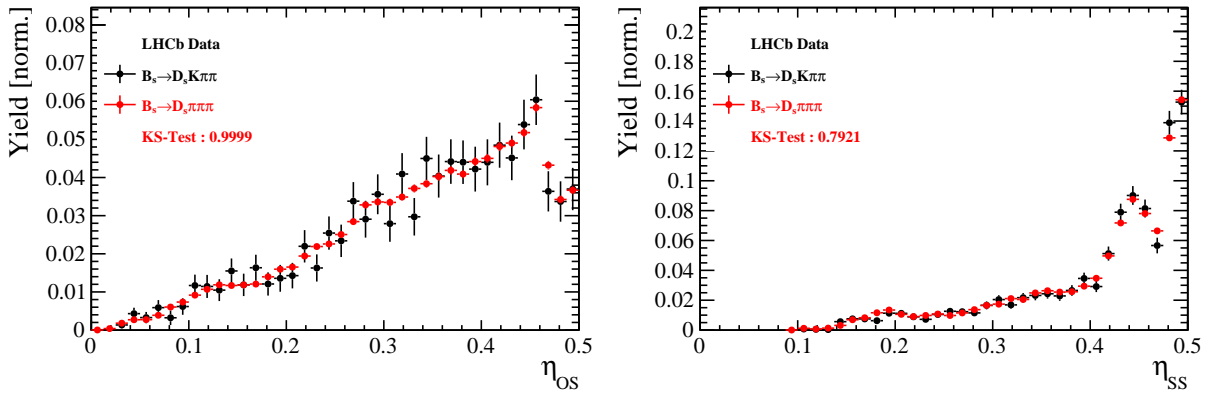


Figure 7.3: Distributions of the predicted mistag η for the OS combination (left) and the SS kaon tagger (right) for signal candidates in the $B_s^0 \rightarrow D_s K\pi\pi$ (black) and $B_s^0 \rightarrow D_s \pi\pi\pi$ (red) data samples.

Table 7.3: The flavour tagging performances for only OS tagged, only SS tagged and both OS and SS tagged events for Run-I data.

$B_s \rightarrow D_s \pi\pi\pi$	$\epsilon_{tag} [\%]$	$\langle \omega \rangle [\%]$	$\epsilon_{eff} [\%]$
Only OS	14.75 ± 0.11	39.03 ± 0.82	1.27 ± 0.17
Only SS	35.46 ± 0.18	44.15 ± 0.64	1.10 ± 0.19
Both OS-SS	32.92 ± 0.30	37.18 ± 0.76	3.48 ± 0.35
Combined	83.12 ± 0.37	40.48 ± 0.72	5.85 ± 0.43

Table 7.4: The flavour tagging performances for only OS tagged, only SS tagged and both OS and SS tagged events for Run-II data.

$B_s \rightarrow D_s \pi\pi\pi$	$\epsilon_{tag} [\%]$	$\langle \omega \rangle [\%]$	$\epsilon_{eff} [\%]$
Only OS	10.92 ± 0.05	36.56 ± 0.56	1.09 ± 0.07
Only SS	43.80 ± 0.11	42.44 ± 0.37	1.99 ± 0.15
Both OS-SS	26.08 ± 0.14	34.87 ± 0.45	3.44 ± 0.17
Combined	80.80 ± 0.19	39.20 ± 0.42	6.52 ± 0.23

8 Production and Detection Asymmetries

8.1 B_s Production Asymmetry

The production rates of b and \bar{b} hadrons in pp collisions are not expected to be identical, therefore this effect must be taken into account when computing CP asymmetries. The production asymmetry for B_s mesons is defined as:

$$A_p(B_s^0) = \frac{\sigma(\bar{B}_s^0) - \sigma(B_s^0)}{\sigma(\bar{B}_s^0) + \sigma(B_s^0)} \quad (8.1)$$

where σ are the corresponding production cross-section. This asymmetry was measured by LHCb in pp collisions at $\sqrt{s} = 7$ TeV and $\sqrt{s} = 8$ TeV by means of a time-dependent analysis of $B_s \rightarrow D_s^- \pi^+$ decays [43]. The results in bins of p_T and η of the B_s meson are shown in Table 8.1. To correct for the different kinematics of $B_s \rightarrow D_s^- \pi^+$ and $B_s^0 \rightarrow D_s K\pi\pi$ decays, the measured B_s production asymmetries $A_p(p_T, \eta)$ are folded with the sWeighted p_T, η distribution of our signal channel. The resulting effective production asymmetries are:

$$A_p(B_s^0)_{2011} = (-0.506 \pm 1.90)\% \quad (8.2)$$

$$A_p(B_s^0)_{2012} = (-0.164 \pm 1.30)\% \quad (8.3)$$

$$A_p(B_s^0)_{\text{Run-I}} = (-0.045 \pm 1.04)\%. \quad (8.4)$$

As for Run-II data no measurement is available yet, we determine the production asymmetry from $B_s \rightarrow D_s \pi\pi\pi$ data together with the tagging parameters.

Table 8.1: B_s production asymmetries in kinematic bins for 2011 and 2012 data. [43]

p_T [GeV/c]	η	$A_p(B_s^0)_{\sqrt{s}=7 \text{ TeV}}$	$A_p(B_s^0)_{\sqrt{s}=8 \text{ TeV}}$
(2.00, 7.00)	(2.10, 3.00)	$0.0166 \pm 0.0632 \pm 0.0125$	$0.0412 \pm 0.0416 \pm 0.0150$
(2.00, 7.00)	(3.00, 3.30)	$0.0311 \pm 0.0773 \pm 0.0151$	$-0.0241 \pm 0.0574 \pm 0.0079$
(2.00, 7.00)	(3.30, 4.50)	$-0.0833 \pm 0.0558 \pm 0.0132$	$0.0166 \pm 0.0391 \pm 0.0092$
(7.00, 9.50)	(2.10, 3.00)	$0.0364 \pm 0.0479 \pm 0.0068$	$0.0482 \pm 0.0320 \pm 0.0067$
(7.00, 9.50)	(3.00, 3.30)	$0.0206 \pm 0.0682 \pm 0.0127$	$0.0983 \pm 0.0470 \pm 0.0155$
(7.00, 9.50)	(3.30, 4.50)	$0.0058 \pm 0.0584 \pm 0.0089$	$-0.0430 \pm 0.0386 \pm 0.0079$
(9.50, 12.00)	(2.10, 3.00)	$-0.0039 \pm 0.0456 \pm 0.0121$	$0.0067 \pm 0.0303 \pm 0.0063$
(9.50, 12.00)	(3.00, 3.30)	$0.1095 \pm 0.0723 \pm 0.0179$	$-0.1283 \pm 0.0503 \pm 0.0171$
(9.50, 12.00)	(3.30, 4.50)	$0.1539 \pm 0.0722 \pm 0.0212$	$-0.0500 \pm 0.0460 \pm 0.0104$
(12.00, 30.00)	(2.10, 3.00)	$-0.0271 \pm 0.0336 \pm 0.0061$	$-0.0012 \pm 0.0222 \pm 0.0050$
(12.00, 30.00)	(3.00, 3.30)	$-0.0542 \pm 0.0612 \pm 0.0106$	$0.0421 \pm 0.0416 \pm 0.0162$
(12.00, 30.00)	(3.30, 4.50)	$-0.0586 \pm 0.0648 \pm 0.0150$	$0.0537 \pm 0.0447 \pm 0.0124$

734 8.2 $K^-\pi^+$ Detection Asymmetry

735 The presented measurement of the CKM-angle γ using $B_s^0 \rightarrow D_s K\pi\pi$ decays is sensitive to
 736 a possible charge asymmetry of the kaon. Kaons are known to have a nuclear cross-section
 737 which is asymmetrically dependent on the sign of their charge. It is indispensable to
 738 determine the charge asymmetry of the kaon, as fitting without taking this effect into
 739 account would introduce a 'fake' CP violation. Instead of determining the single track
 740 detection asymmetry of a kaon, it is found that the combined two track asymmetry of a
 741 kaon-pion pair is much easier to access [44]. Therefore, the two track asymmetry defined
 742 as

$$A^{det}(K^-\pi^+) = \frac{\epsilon^{det}(K^-\pi^+) - \epsilon^{det}(K^+\pi^-)}{\epsilon^{det}(K^-\pi^+) + \epsilon^{det}(K^+\pi^-)}, \quad (8.5)$$

743 is used.

744 This asymmetry can be measured from the difference in asymmetries in the $D^+ \rightarrow$
 745 $K^-\pi^+\pi^+$ and $D^+ \rightarrow K_s^0\pi^+$ modes [45]:

$$\begin{aligned} A^{det}(K^-\pi^+) &= \frac{N(D^+ \rightarrow K^-\pi^+\pi^+) - N(D^- \rightarrow K^+\pi^-\pi^-)}{N(D^+ \rightarrow K^-\pi^+\pi^+) + N(D^- \rightarrow K^+\pi^-\pi^-)} \\ &\quad - \frac{N(D^+ \rightarrow K_s^0\pi^+) - N(D^- \rightarrow K_s^0\pi^-)}{N(D^+ \rightarrow K_s^0\pi^+) + N(D^- \rightarrow K_s^0\pi^-)} \\ &\quad - A(K^0), \end{aligned} \quad (8.6)$$

746 where possible CP violation in the $D^+ \rightarrow K_s^0\pi^+$ mode is predicted to be smaller than
 747 10^{-4} in the Standard Model [46]. The asymmetry in the neutral kaon system, $A(K^0)$, has
 748 to be taken into account as a correction.

749 We use a dedicated LHCb tool to determine $A^{det}(K^-\pi^+)$ for all data taking periods
 750 used in this analysis. A detailed description can be found in [45]. The tool provides
 751 large calibration samples of $D^\pm \rightarrow K^\pm\pi^\pm\pi^\pm$ and $D^\pm \rightarrow K_s^0\pi^\pm$ decays, which are used to
 752 determine the asymmetry following Eq. 8.6. Several weighting steps are performed to
 753 match the kinematics of the calibration samples to our signal decay sample:

754 First, weights are assigned to the K^\pm and π^\pm of the $D^\pm \rightarrow K^\pm\pi^\pm\pi^\pm$ sample, using
 755 p, η of the K^\pm and p_T, η of the π^\pm from our $B_s^0 \rightarrow D_s K\pi\pi$ signal decay. Then, weights
 756 are assigned to the D^\pm (p_T, η) and the π^\pm (p_T) of the $D^\pm \rightarrow K_s^0\pi^\pm$ sample to match
 757 the corresponding, weighted distributions of the $D^\pm \rightarrow K^\pm\pi^\pm\pi^\pm$ sample. In a last
 758 step, weights are assigned to match the bachelor pions ϕ distributions between the two
 759 calibration samples.

760 After the samples are weighted, fits are performed to the invariant
 761 $m(K^-\pi^+\pi^+)/m(K^+\pi^-\pi^-)$ and $m(K_s^0\pi^+)/m(K_s^0\pi^-)$ distributions to determine
 762 $A^{det}(K^-\pi^+)$. The PDFs used to describe the invariant mass distributions consist of
 763 gaussian functions for the signal component and exponentials describing the residual
 764 background.

765 The detection asymmetry is determined separately for every year and (since it is a
 766 charge asymmetry effect) magnet polarity. Serving as an example for Run-I and Run-
 767 II, the fits used to determine $N(D^+ \rightarrow K^-\pi^+\pi^+)/N(D^- \rightarrow K^+\pi^-\pi^-)$ and $N(D^+ \rightarrow$
 768 $K_s^0\pi^+)/N(D^- \rightarrow K_s^0\pi^-)$ for 2011, magnet up data and 2015, magnet up data are shown
 769 in Fig. 8.1 and 8.2 respectively. The obtained values of $A^{det}(K^-\pi^+) + A(K^0)$ for all years
 770 and polarities are shown in Table 8.2.

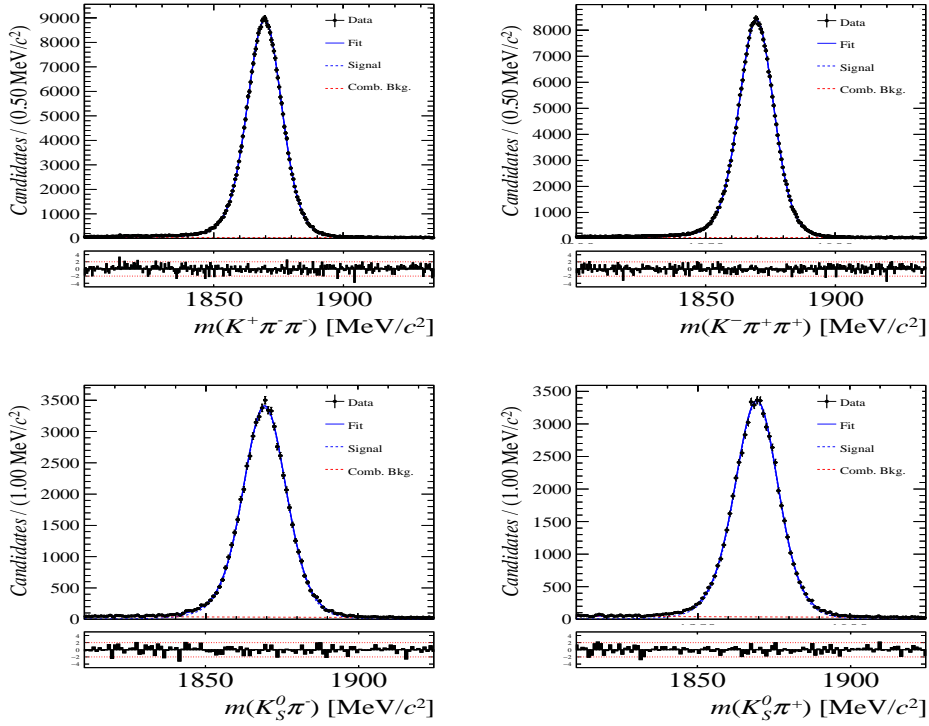


Figure 8.1: Distributions of the invariant mass of (top) $D^\pm \rightarrow K^\pm \pi^\pm \pi^\pm$ and (bottom) $D^\pm \rightarrow K_s^0 \pi^\pm$ candidates for Run-I data from the calibration samples. A fit described in the text is overlaid.

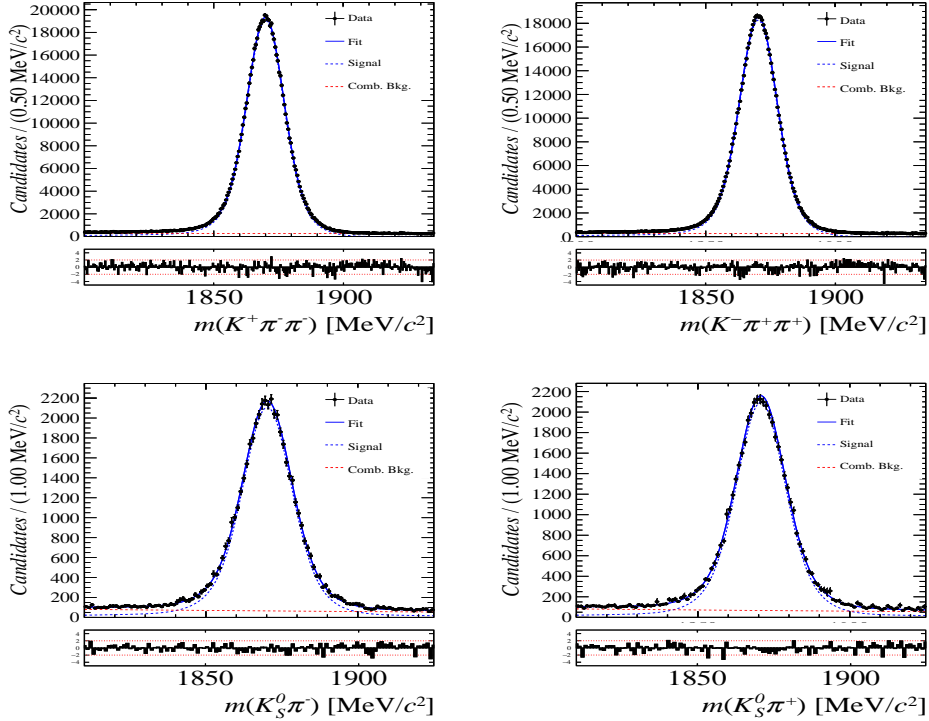


Figure 8.2: Distributions of the invariant mass of (top) $D^\pm \rightarrow K^\pm \pi^\pm \pi^\pm$ and (bottom) $D^\pm \rightarrow K_s^0 \pi^\pm$ candidates for Run-II data from the calibration samples. A fit described in the text is overlaid.

Data sample	$A^{det}(K^-\pi^+) + A(K^0)$ [%]
Run-I	
2011, mag. up	-2.01 \pm 0.32
2011, mag. down	-0.16 \pm 0.28
2011, average	-1.09 \pm 0.21
2012, mag. up	-0.90 \pm 0.20
2012, mag. down	-1.01 \pm 0.22
2012, average	-0.96 \pm 0.15
Run-II	
mag. up	-1.16 \pm 0.34
mag. down	-0.65 \pm 0.27
average	-0.91 \pm 0.22

Table 8.2: Summary of the $K^-\pi^+$ detection asymmetry obtained from the fits to the Run-I and Run-II calibration samples.

9 Decay-time fit

This section covers the (phase space integrated) decay-time fits to $B_s^0 \rightarrow D_s h\pi\pi$ data. We use the **sFit** technique [47] to statistically subtract the background, leaving only the signal PDF to describe the decay-time. The **sWeights** are calculated based on the fit to the reconstructed B_s mass distribution described in Sec. 4. The signal PDF is conditional on the tagging decisions q_i , the mistag estimates η_i ($i = \text{OS,SS}$) and the decay-time error δt :

$$\mathcal{P}(t|\delta t, q_{\text{OS}}, \eta_{\text{OS}}, q_{\text{SS}}, \eta_{\text{SS}}) \propto [p(t' | q_{\text{OS}}, \eta_{\text{OS}}, q_{\text{SS}}, \eta_{\text{SS}}) \otimes \mathcal{R}(t - t', \delta t)] \cdot \epsilon(t) \quad (9.1)$$

where $p(t|q_{\text{OS}}, \eta_{\text{OS}}, q_{\text{SS}}, \eta_{\text{SS}})$ is given by Equation 2.7 taking the tagging dilution into account. The decay-time acceptance $\epsilon(t)$ (Sec. 6) and the Gaussian time-resolution function $\mathcal{R}(t - t', \delta t)$ (Sec. 5) are fixed to the values obtained by the dedicated studies. We fix the values of Γ_s and $\Delta\Gamma_s$ to the latest HFAG results [38].

The unbinned maximum likelihood fits are performed simultaneously in four categories: [Run-I,L0-TOS], [Run-I,L0-TIS], [Run-II,L0-TOS] and [Run-II,L0-TIS].

9.1 Fit to $B_s^0 \rightarrow D_s \pi\pi\pi$ data

Since the decay $B_s^0 \rightarrow D_s \pi\pi\pi$ is flavour specific, the CP coefficients can be fixed to $C = 1$ and $D_f = D_{\bar{f}} = S_f = S_{\bar{f}} = 0$. The fit determines the calibration parameters for the OS-Combo and SS-Kaon taggers, the B_s^0 production asymmetry for Run-II data as well as the mixing frequency Δm_s . Table 9.1 summarizes the fitted parameters. The **sWeighted** decay-time distribution and the time-dependent asymmetry A_{mix} between mixed and unmixed B_s^0 candidates are shown in Fig. 9.1 along with the fit projections.

Table 9.1: Parameters determined from a fit to the $B_s \rightarrow D_s \pi\pi\pi$ decay-time distribution. The uncertainties are statistical and systematic, respectively.

Fit Parameter	Run-I	Run-II
p_0^{OS}	$0.397 \pm 0.010 \pm 0.010$	$0.367 \pm 0.005 \pm 0.009$
p_1^{OS}	$0.908 \pm 0.087 \pm 0.090$	$0.772 \pm 0.046 \pm 0.063$
Δp_0^{OS}	$0.030 \pm 0.011 \pm 0.002$	$0.006 \pm 0.006 \pm 0.000$
Δp_1^{OS}	$0.010 \pm 0.094 \pm 0.015$	$0.085 \pm 0.054 \pm 0.003$
$\epsilon_{\text{tag}}^{OS} [\%]$	$47.667 \pm 0.365 \pm 0.032$	$37.018 \pm 0.181 \pm 0.009$
$\Delta\epsilon_{\text{tag}}^{OS} [\%]$	$0.087 \pm 1.249 \pm 0.093$	$0.185 \pm 0.582 \pm 0.127$
p_0^{SS}	$0.443 \pm 0.008 \pm 0.004$	$0.426 \pm 0.004 \pm 0.004$
p_1^{SS}	$0.974 \pm 0.110 \pm 0.066$	$0.800 \pm 0.041 \pm 0.050$
Δp_0^{SS}	$-0.019 \pm 0.009 \pm 0.001$	$-0.017 \pm 0.005 \pm 0.000$
Δp_1^{SS}	$0.057 \pm 0.125 \pm 0.018$	$0.038 \pm 0.048 \pm 0.004$
$\epsilon_{\text{tag}}^{SS} [\%]$	$0.684 \pm 0.003 \pm 0.000$	$0.699 \pm 0.002 \pm 0.000$
$\Delta\epsilon_{\text{tag}}^{SS} [\%]$	$-0.003 \pm 0.012 \pm 0.001$	$-0.003 \pm 0.006 \pm 0.000$
$A_P [\%]$	-0.045 (fixed)	$-0.150 \pm 0.618 \pm 0.090$
$\Delta m_s [\text{ps}^{-1}]$		$\text{xx.xx} \pm 0.009 \pm 0.006$

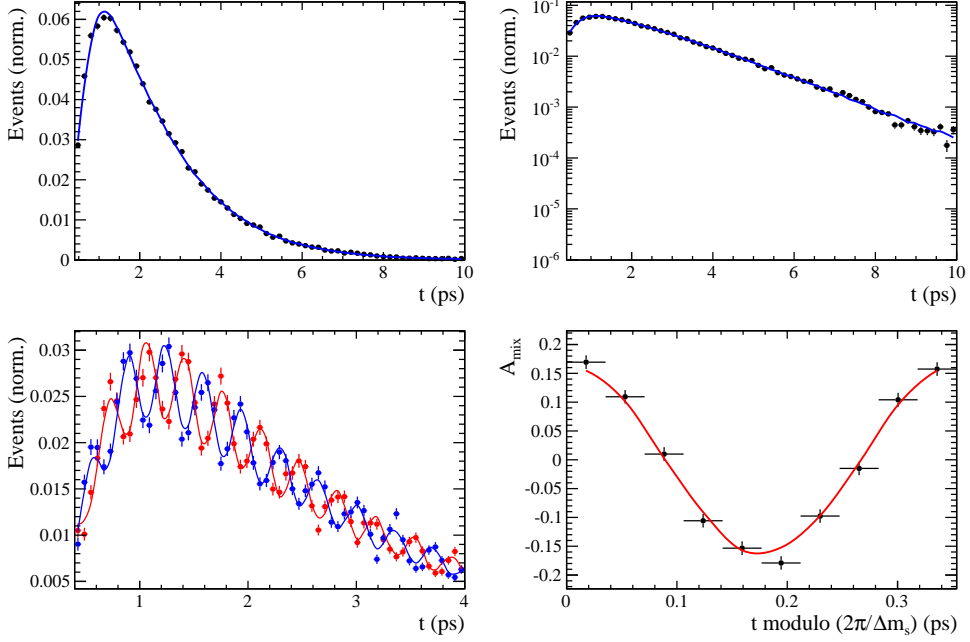


Figure 9.1: Top: Flavour averaged decay time distribution of $B_s^0 \rightarrow D_s\pi\pi\pi$ candidates. Bottom-left: Tagged decay time distribution of mixed (red) and unmixed (blue) signal candidates. Bottom-right: Time-dependent asymmetry A_{mix} between mixed and unmixed B_s^0 candidates folded into one oscillation period.

790 9.2 Fit to $B_s^0 \rightarrow D_s K\pi\pi$ data

791 The measured CP coefficients $C, D_f, D_{\bar{f}}, S_f$ and $S_{\bar{f}}$ extracted from a fit to the
 792 $B_s \rightarrow D_s K\pi\pi$ decay-time distribution are reported in Table 9.2. The fit projection is
 793 shown in Fig. 9.2. We included Gaussian-constraints for the tagging calibration parameters
 794 with the central values and uncertainties determined in Sec. 9.1.

795

796

The CP coefficients will be converted to the observables $r, \kappa, \delta, \gamma$ using the Gamma-Combo package after unblinding.

797

Currently the mixing frequency is fixed to the HFAG value. We intend to update
 the fit after unblinding our result from the $B_s^0 \rightarrow D_s\pi\pi\pi$ fit since our precision is
 significantly higher.

798

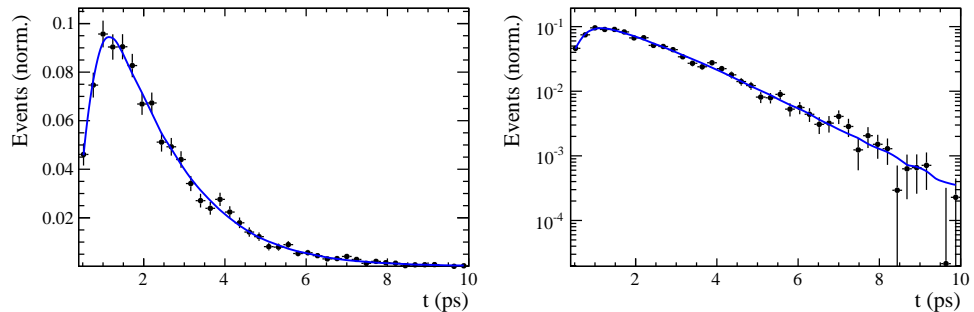


Figure 9.2: Decay-time distribution of $B_s^0 \rightarrow D_s K\pi\pi$ signal candidates with the fit projection overlaid.

Table 9.2: CP coefficients determined from a fit to the $B_s \rightarrow D_s K\pi\pi$ decay-time distribution. The uncertainties are statistical and systematic, respectively.

Fit Parameter	Value
C	x.xx \pm 0.11 \pm 0.02
D	x.xx \pm 0.29 \pm 0.08
\bar{D}	x.xx \pm 0.27 \pm 0.09
S	x.xx \pm 0.16 \pm 0.05
\bar{S}	x.xx \pm 0.16 \pm 0.04

799 10 Time-dependent amplitude fit

800 The signal PDF used for the full time-dependent fit is defined as

$$\mathcal{P}(\mathbf{x}, t | \delta t, q_{OS}, \eta_{OS}, q_{SS}, \eta_{SS}) \propto [p(\mathbf{x}, t' | q_{OS}, \eta_{OS}, q_{SS}, \eta_{SS}) \otimes \mathcal{R}(t - t', \delta t)] \cdot \epsilon(t) \quad (10.1)$$

801 where $p(\mathbf{x}, t | q_{OS}, \eta_{OS}, q_{SS}, \eta_{SS})$ is given the differential decay rate in Equation 2.29 taking
 802 the tagging dilution into account. The phase space efficiency $\epsilon(\mathbf{x})$ is only included in the
 803 normalization of $\mathcal{P}(\mathbf{x}, t | \delta t, q_{OS}, \eta_{OS}, q_{SS}, \eta_{SS})$ as discussed in Sec 6.3. The model selection
 804 of the amplitude components is described in the following Section. The remaining fitting
 805 strategy is exactly the same as for the decay-time fits, see Sec. 9.

806 10.1 Signal Model Construction

807 The light meson spectrum comprises multiple resonances which are expected to contribute
 808 to $B_s \rightarrow D_s K\pi\pi$ decays as intermediate states. Apart from clear contributions coming
 809 from resonances such as $K_1(1270)$, $K_1(1400)$, $\rho(770)$ and $K^*(892)^0$, the remaining structure
 810 is impossible to infer due to the cornucopia of broad, overlapping and interfering resonances
 811 within the phase space boundary. We follow the LASSO [48, 49] approach to limit the
 812 model complexity in two steps.

813 First, we fit the time-integrated and flavour averaged phase-space distribution of
 814 $B_s \rightarrow D_s K\pi\pi$ decays. In this case, a single total amplitude can be used:

$$\mathcal{A}_f^{eff}(\mathbf{x}) = \sum_i a_i^{eff} A_i(\mathbf{x}) \quad (10.2)$$

815 which effectively describes the incoherent superposition of the $b \rightarrow c$ and $b \rightarrow u$ amplitudes:

$$|A_f^{eff}(\mathbf{x})|^2 = |A_f^c(\mathbf{x})|^2 + |A_f^u(\mathbf{x})|^2. \quad (10.3)$$

816 This significantly simplifies the fitting procedure and allows us to include the whole pool
 817 of considered intermediate state amplitudes A_i which can be found in Appendix G. The
 818 LASSO penalty term added to the likelihood function

$$-2 \log \mathcal{L} \rightarrow -2 \log \mathcal{L} + \lambda \sum_i \sqrt{\int |a_i^{eff} A_i(\mathbf{x})|^2 d\Phi_4}, \quad (10.4)$$

819 shrinks the amplitude coefficients towards zero. The amount of shrinkage is controlled by
 820 the parameter λ , to be tuned on data. Higher values for λ encourage sparse models, *i.e.*
 821 models with only a few non-zero amplitude coefficients. The optimal value for λ is found
 822 by minimizing the Bayesian information criteria [50] (BIC),

$$BIC(\lambda) = -2 \log \mathcal{L} + r \log N_{Sig}, \quad (10.5)$$

823 where N_{Sig} is the number of signal events and r is the number of amplitudes with a decay
 824 fraction above a certain threshold. The fit fractions are defined as

$$F_i \equiv \frac{\int |a_i^{eff} A_i(\mathbf{x})|^2 d\Phi_4}{\int |\mathcal{A}_f^{eff}(\mathbf{x})|^2 d\Phi_4}, \quad (10.6)$$

and are a measure of the relative strength between the different transitions. Figure 10.1(left) shows the distribution of BIC values obtained by scanning over λ where we choose the decay fraction threshold to be 0.5%. At the optimal value of $\lambda = 50$, the set of amplitudes with a decay fraction above the threshold are considered further for step two of the model selection. The selected amplitudes and their fractions are summarized in Table 10.1. The fit projections are shown in Fig. 10.2. The set of selected amplitudes is stable for thresholds between 0.1% and 1%.. Other choices result in marginally different models containing one component more or less. These are included in the set of alternative models used for the systematic studies presented in Sec. 11.10.

In Stage 2, the LASSO procedure is again performed by fitting the full time-dependent amplitude PDF. The components selected by Stage 1 are included for both $b \rightarrow c$ and $b \rightarrow u$ transitions and the likelihood is extended as follows:

$$-2 \log \mathcal{L} \rightarrow -2 \log \mathcal{L} + \lambda \sum_i \sqrt{\int |a_i^c A_i(\mathbf{x})|^2 d\Phi_4} + \lambda \sum_i \sqrt{\int |a_i^u A_i(\mathbf{x})|^2 d\Phi_4} \quad (10.7)$$

Figure 10.1(right) shows a plot of the complexity factor λ , against the resulting BIC values. The final set of $b \rightarrow c$ and $b \rightarrow u$ amplitudes is selected using the optimal value of $\lambda = 28$, and is henceforth called the LASSO model.

Table 10.1: Fit fractions of the amplitudes selected by Stage 1 of the model selection procedure.

Decay channel	Fraction [%]
$B_s \rightarrow K(1)(1270)^+ (\rightarrow K^*(892)^0 (\rightarrow K^+ \pi^-) \pi^+) D_s^-$	8.56 ± 1.43
$B_s \rightarrow K(1)(1400)^+ (\rightarrow K^*(892)^0 (\rightarrow K^+ \pi^-) \pi^+) D_s^-$	43.72 ± 2.80
$B_s \rightarrow K(1460)^+ (\rightarrow K^*(892)^0 (\rightarrow K^+ \pi^-) \pi^+) D_s^-$	3.25 ± 0.69
$B_s \rightarrow K^*(1410)^+ (\rightarrow K^*(892)^0 (\rightarrow K^+ \pi^-) \pi^+) D_s^-$	15.33 ± 1.13
$B_s \rightarrow (D_s^- \pi^+) P K^*(892)^0 (\rightarrow K^+ \pi^-)$	4.63 ± 0.69
$B_s \rightarrow K^*(1410)^+ (\rightarrow \rho(770)^0 (\rightarrow \pi^+ \pi^-) K^+) D_s^-$	5.58 ± 0.62
$B_s \rightarrow (D_s^- K^+) P \rho(770)^0 (\rightarrow \pi^+ \pi^-)$	1.49 ± 0.40
$B_s \rightarrow K(1)(1270)^+ (\rightarrow K(0)^*(1430)^0 (\rightarrow K^+ \pi^-) \pi^+) D_s^-$	4.72 ± 0.54
$B_s \rightarrow K(1)(1270)^+ (\rightarrow \rho(770)^0 (\rightarrow \pi^+ \pi^-) K^+) D_s^-$	14.20 ± 1.56
Sum	101.47 ± 3.86

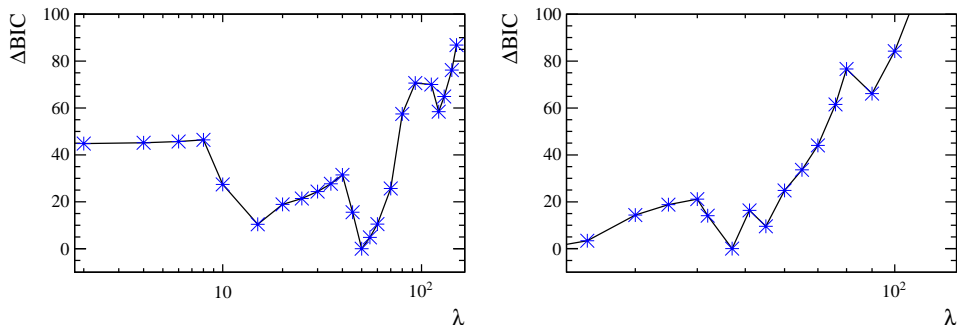


Figure 10.1: Difference in the BIC value from its minimum as function of the LASSO parameter λ for step 1 (left) and step 2 (right) of the model selection.

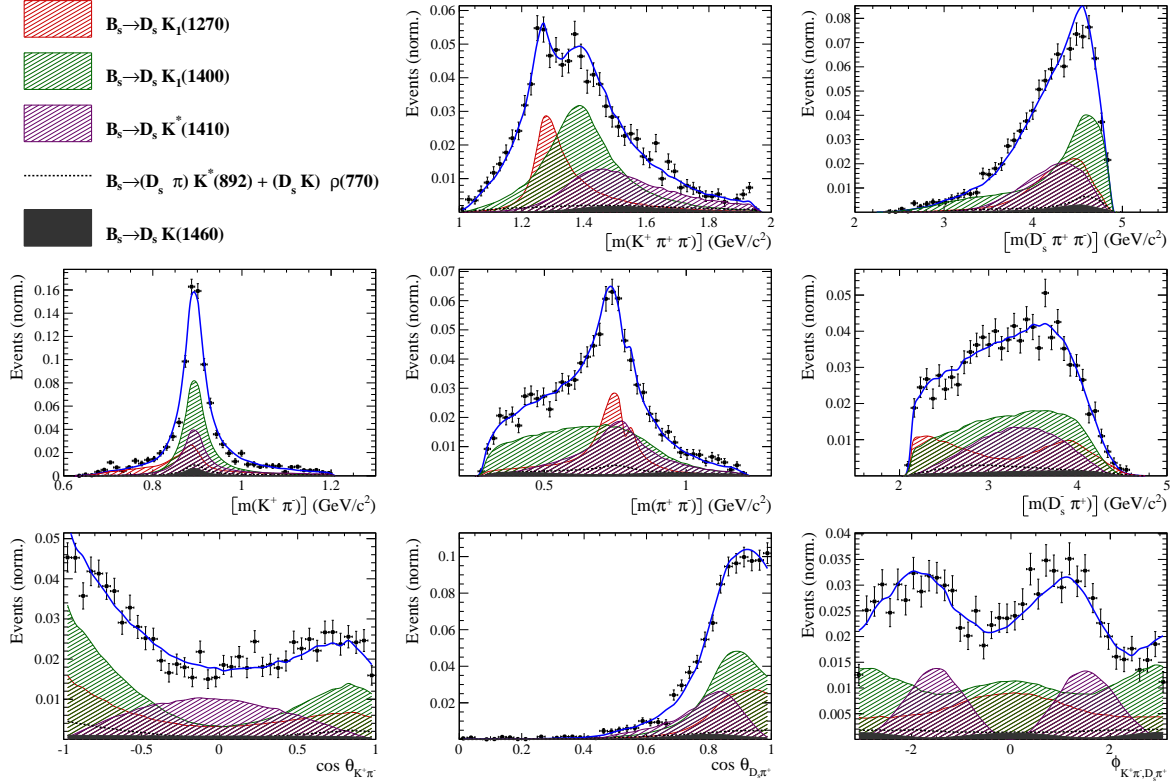


Figure 10.2: Projections of the fit result to the time-integrated and flavour averaged phase-space distribution of $B_s \rightarrow D_s K \pi \pi$ decays.

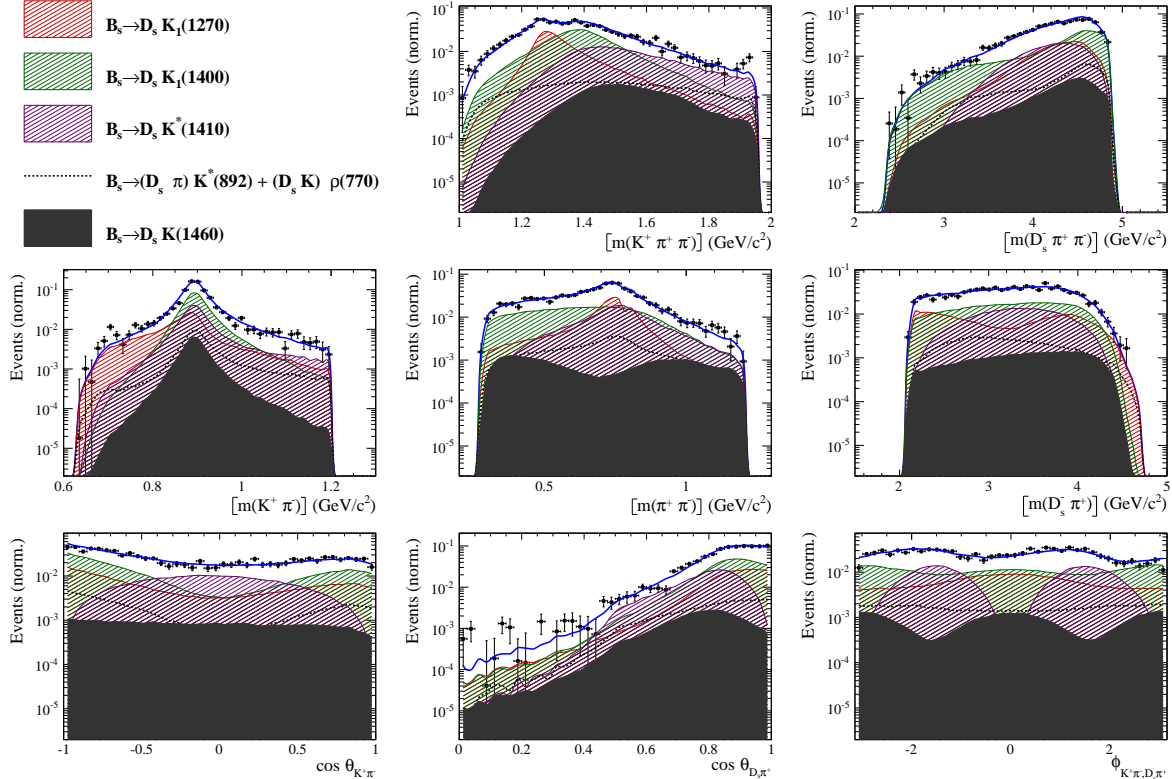


Figure 10.3: Projections of the fit result to the time-integrated and flavour averaged phase-space distribution of $B_s \rightarrow D_s K \pi \pi$ decays in logarithmic scale.

840 10.2 Results

841 Table 10.2 lists the modulus and phases of the complex amplitude coefficients a_i^c and a_i^u ,
 842 obtained by fitting the LASSO model to the data. The corresponding fit fractions for the
 843 $b \rightarrow c$ and $b \rightarrow u$ amplitudes are individually normalized

$$F_i^{c,u} \equiv \frac{\int |a_i^{c,u} A_i(\mathbf{x})|^2 d\Phi_4}{\int |\mathcal{A}_f^{c,u}(\mathbf{x})|^2 d\Phi_4} \quad (10.8)$$

844 and shown in Table 10.3. In addition to the amplitude coefficients, the amplitude ratio
 845 and the strong and weak phase differences between the $b \rightarrow c$ and $b \rightarrow u$ decays are
 846 determined. Moreover, the masses and widths of the $K_1(1400)$ and $K^*(1410)$ resonances
 847 are fitted.

848 Figure 10.4 shows the distributions of selected phase space observables, which demon-
 849 strate reasonable agreement between data and the fit model. We also project into the
 850 transversity basis to demonstrate good description of the overall angular structure (see
 851 10.4 bottom row). The acoplanarity angle χ , is the angle between the two decay planes
 852 formed by the $K^+\pi^-$ system and the $D_s^-\pi^+$ system in the B_s rest frame; boosting into the
 853 rest frames of the two-body systems defining these decay planes, the two helicity variables
 854 are defined as the cosine of the angle, θ , of the K^+ or D_S^- momentum with the B_s flight
 855 direction.

856 In order to quantify the quality of the fit in the five-dimensional phase space, a χ^2
 857 value is determined by binning the data;

$$\chi^2 = \sum_{b=1}^{N_{\text{bins}}} \frac{(N_b - N_b^{\text{exp}})^2}{N_b^{\text{exp}}}, \quad (10.9)$$

858 where N_b is the number of data events in a given bin, N_b^{exp} is the event count predicted
 859 by the fitted PDF and N_{bins} is the number of bins. An adaptive binning is used to ensure
 860 sufficient statistics in each bin for a robust χ^2 calculation [51]. At least 25 events per
 861 bin are required. The number of degrees of freedom ν , in an unbinned fit is bounded by
 862 $N_{\text{bins}} - 1$ and $(N_{\text{bins}} - 1) - N_{\text{par}}$, where N_{par} is the number of free fit parameters. We use
 863 the χ^2 value divided by $\nu = (N_{\text{bins}} - 1) - N_{\text{par}}$ as a conservative estimate. For the LASSO
 864 model, this amounts to $\chi^2/\nu = 1.40$ with $\nu = 137$, indicating a decent fit quality.

Table 10.2: Modulus and phases of the amplitudes contributing to $b \rightarrow c$ and $b \rightarrow u$ decays. In case of multiple decay modes of three-body resonances, the amplitude coefficients are defined relative to the one listed first. Additional fit parameters are listed below. The first quoted uncertainty is statistical, while the second arises from systematic sources. The third uncertainty arises from the alternative models considered.

Decay Channel	$A_{b \rightarrow c}$		$A_{b \rightarrow u}$	
	$ a_i $	$\arg(a_i)[^\circ]$	$ a_i $	$\arg(a_i)[^\circ]$
$B_s \rightarrow D_s (K_1(1270) \rightarrow K \rho(770))$	1.0	0.0	1.0	0.0
$K_1(1270) \rightarrow K^*(892) \pi$	$0.76 \pm 0.11 \pm 0.09$	$60.9 \pm 9.6 \pm 10.1$		
$K_1(1270) \rightarrow K_0^*(1430) \pi$	$0.68 \pm 0.06 \pm 0.13$	$116.5 \pm 5.1 \pm 9.4$		
$B_s \rightarrow D_s (K_1(1400) \rightarrow K^*(892) \pi)$	$2.53 \pm 0.27 \pm 0.36$	$12.9 \pm 7.4 \pm 6.5$	$0.67 \pm 0.20 \pm 0.55$	$-76.3 \pm 16.9 \pm 19.9$
$B_s \rightarrow D_s (K^*(1410) \rightarrow K^*(892) \pi)$	$1.28 \pm 0.12 \pm 0.07$	$54.9 \pm 5.6 \pm 6.2$		
$K^*(1410) \rightarrow K \rho(770)$	$0.66 \pm 0.04 \pm 0.03$	$-172.9 \pm 5.0 \pm 7.8$		
$B_s \rightarrow D_s (K(1460) \rightarrow K^*(892) \pi)$			$0.77 \pm 0.11 \pm 0.26$	$-93.6 \pm 11.2 \pm 10.8$
$B_s \rightarrow (D_s \pi)_P K^*(892)$	$1.02 \pm 0.13 \pm 0.13$	$-28.4 \pm 8.0 \pm 7.1$	$0.79 \pm 0.18 \pm 0.16$	$3.7 \pm 12.5 \pm 12.9$
$B_s \rightarrow (D_s K)_P \rho(770)$			$0.61 \pm 0.08 \pm 0.09$	$36.4 \pm 7.7 \pm 16.0$
Fit parameter	Value			
$m_{K_1(1400)} [\text{MeV}]$	$1394.9 \pm 8.8 \pm 7.1 \pm 20.6$			
$\Gamma_{K_1(1400)} [\text{MeV}]$	$224.0 \pm 15.9 \pm 11.1 \pm 17.9$			
$m_{K^*(1410)} [\text{MeV}]$	$1419.6 \pm 10.8 \pm 17.6 \pm 10.6$			
$\Gamma_{K^*(1410)} [\text{MeV}]$	$342.4 \pm 23.5 \pm 40.4 \pm 20.9$			
r	$xx.xx \pm 0.04 \pm 0.02 \pm 0.04$			
$\delta [^\circ]$	$xx.xx \pm 16.1 \pm 6.6 \pm 4.9$			
$\gamma - 2\beta_s [^\circ]$	$xx.xx \pm 16.1 \pm 9.6 \pm 5.0$			

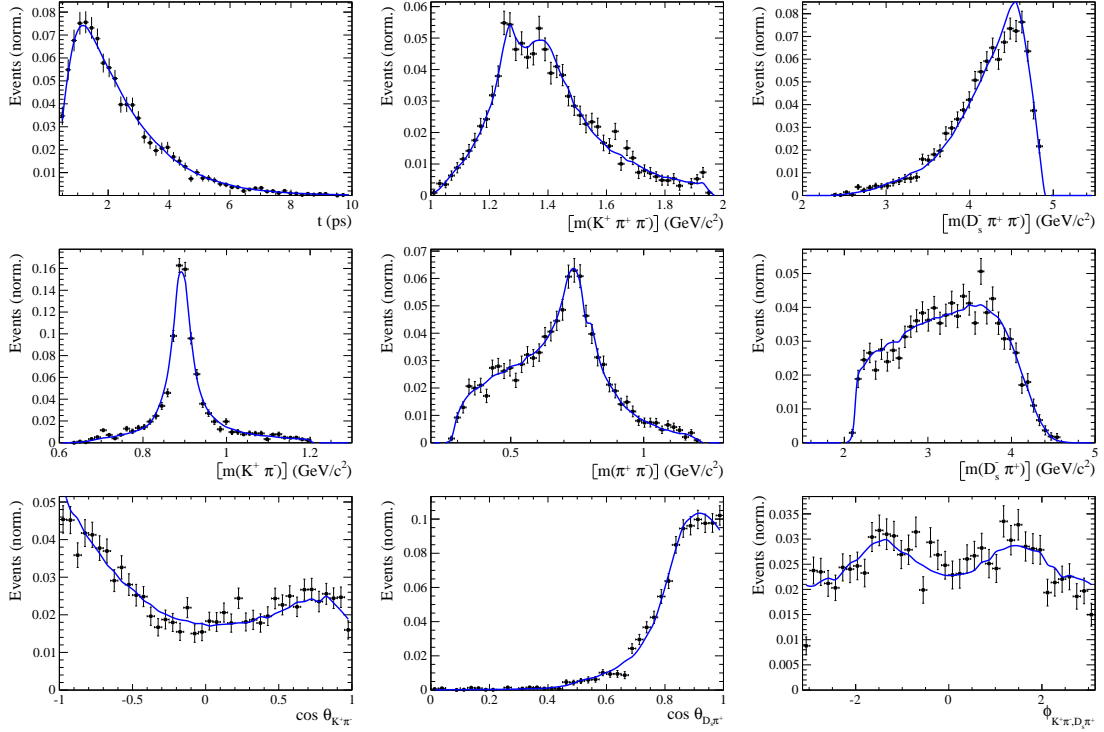


Figure 10.4: Projections of the full time-dependent amplitude fit.

Table 10.3: Fit fractions of the amplitudes contributing to $b \rightarrow c$ and $b \rightarrow u$ decays.

Decay Channel	$F_{b \rightarrow c} [\%]$	$F_{b \rightarrow u} [\%]$
$B_s \rightarrow D_s (K_1(1270) \rightarrow K^*(892) \pi)$	5.2 ± 1.2	17.6 ± 4.2
$B_s \rightarrow D_s (K_1(1270) \rightarrow K \rho(770))$	9.4 ± 1.1	32.0 ± 4.9
$B_s \rightarrow D_s (K_1(1270) \rightarrow K_0^*(1430) \pi)$	4.5 ± 0.6	15.2 ± 2.4
$B_s \rightarrow D_s (K_1(1400) \rightarrow K^*(892) \pi)$	59.9 ± 5.0	16.6 ± 8.5
$B_s \rightarrow D_s (K^*(1410) \rightarrow K^*(892) \pi)$	14.8 ± 0.9	
$B_s \rightarrow D_s (K^*(1410) \rightarrow K \rho(770))$	7.0 ± 0.6	
$B_s \rightarrow D_s (K(1460) \rightarrow K^*(892) \pi)$		18.8 ± 4.2
$B_s \rightarrow (D_s \pi)_P K^*(892)$	9.7 ± 1.8	21.8 ± 7.2
$B_s \rightarrow (D_s K)_P \rho(770)$		13.5 ± 4.0
<i>Sum</i>	110.5 ± 5.4	135.4 ± 10.3

865 11 Systematic uncertainties

866 The systematic uncertainties on the measured observables are summarized in Table 11.3 for
867 the decay-time fit to $B_s \rightarrow D_s \pi\pi\pi$, in Table 11.4 for the decay-time fit to $B_s \rightarrow D_s K\pi\pi$
868 and in Table 11.5 for the full time-dependent amplitude fit to $B_s \rightarrow D_s K\pi\pi$ decays. A
869 description of each systematic effect is given in the following subsections starting with the
870 ones common to all fits. Afterwards, systematic effect specific to the amplitude description
871 are discussed.

872 11.1 Fit bias

873 Pseudo-experiments are performed, where a signal toy sample of the same size as the
874 number of observed signal data events is generated according to the nominal fit model
875 and subsequently fitted with the same model. The means of the pull distributions are
876 taken as systematic uncertainties of the fit parameters.

877 11.2 Background subtraction

878 The statistical subtraction of the residual background [47], left after the full selection,
879 relies on the correct description of the invariant B_s^0 mass distribution. Since the choice of
880 signal and background models is not unique, alternative parameterizations are tested:

- 881 • The Johnson's SU function which is used as nominal signal model is replaced by the
882 sum of two Crystal Ball functions [52].
- 883 • For the combinatorial background, the nominal second order polynomial is replaced
884 by an exponential function.
- 885 • For the description of the partially reconstructed background, a combination of the
886 RooHILLdini and RooHORNsdini model [53] is used instead of the nominal model of
887 three bifurcated gaussians.
- 888 • For the shape of the mis-ID background, the nominal approach is to use a simulated
889 sample of $B_s^0 \rightarrow D_s^- \pi^+ \pi^- \pi^+$ or $B_s^0 \rightarrow D_s^{*-} \pi^+ \pi^- \pi^+$ decays and flip the mass
890 hypothesis of the π^+ with the higher misidentification probability (see Sec. 4).
891 Two alternative approaches are considered: we flip the mass hypothesis of the π^+
892 candidate with the lower probability of being misidentified; we randomly flip the
893 mass hypothesis of a π^+ candidate. We further vary the default PIDK cut (PIDK
894 > 10) by ± 2 . For each case, the mis-ID yields are reevaluated from the $\pi \rightarrow K$ fake
895 rate and fixed in the corresponding fit.

896 In total 15 (7) different combinations of the modifications discussed above are tested
897 for the fit to the $D_s K\pi\pi$ ($D_s \pi\pi\pi$) mass distribution. For each case, new signal **sWeights**
898 are calculated and the **sFits** to data are repeated. The sample variance of the obtained
899 differences to the nominal fit value are used as systematic uncertainty due to the background
900 subtraction.

901 11.3 Decay-time acceptance

902 The systematic uncertainty related to the decay-time efficiency as well as Γ_s and $\Delta\Gamma_s$ are
 903 studied simultaneously. We generate toys in the nominal configuration and fit back in
 904 both this nominal configuration and a configuration in which we have randomized the
 905 acceptance parameters together with Γ_s and $\Delta\Gamma_s$ within their uncertainties. For each toy,
 906 a pull is calculated by dividing the difference between the fitted values of the nominal
 907 and shifted configurations by the uncertainty in the nominal toy. We add the bias in the
 908 mean of this pull to its width, in quadrature, in order to arrive at the final systematic
 909 uncertainty.

910 To improve the coverage of the multi-dimensional parameter space, a Cholesky decom-
 911 position [54] is used to generate a set of uncorrelated vectors from the covariance matrix
 912 $\text{cov}(\lambda_i, \lambda_j)$, where the vector λ includes the parameters Γ_s , $\Delta\Gamma_s$ and the $N = 4$ spline
 913 coefficients for each category of the simultaneous fit. The correlations between Γ_s ($\Delta\Gamma_s$)
 914 and the spline coefficients are measured by rerunning the acceptance fits described in
 915 Sec. 6.2 with the values of Γ_s ($\Delta\Gamma_s$) varied by $\pm 1\sigma$ and measuring the shift in the spline
 916 coefficients as a fraction of their uncertainty. For the correlation between Γ_s and $\Delta\Gamma_s$ we
 917 use the HFAG value [38].

918 11.4 Decay-time resolution and tagging

919 To study systematic effects originating from the scaling of the decay-time error estimate,
 920 two different approaches which either slightly overestimate or underestimate the resolution
 921 are used:

- 922 • A double Gaussian is fit to the decay-time distributions of fake B_s^0 candidates, but
 923 only the width of the core Gaussian is considered to represent the time resolution in
 924 the respective bin. Therefore the resolution is slightly underestimated in this case.
- 925 • A single Gaussian is fit to the decay-time distributions of fake B_s^0 candidates in a
 926 wide range of $[-3\sigma_t : 1.5\sigma_t]$. Due to the tails of the distribution, which broaden the
 927 width of the Gaussian function, this method slightly overestimates the decay-time
 928 resolution.

929 For each case, a new scaling function is derived:

$$\sigma_{\text{eff}}^{\text{core-Gauss}}(\sigma_t) = (4.9 \pm 2.0) \text{ fs} + (0.821 \pm 0.050) \sigma_t \quad (11.1)$$

$$\sigma_{\text{eff}}^{\text{single-Gauss}}(\sigma_t) = (8.3 \pm 1.5) \text{ fs} + (0.997 \pm 0.037) \sigma_t \quad (11.2)$$

931 which are compared to the nominal result in Fig. 11.1.

932 Due to the high correlation between the decay-time resolution and the tagging calibra-
 933 tion, their systematic uncertainty has to be studied simultaneously. First, the decay-time
 934 fits to $B_s \rightarrow D_s \pi \pi$ data are repeated using the alternative decay-time error scaling
 935 functions. New tagging calibration parameters are obtained which are then used (together
 936 with the respective decay-time error scaling function) in the fits to $B_s \rightarrow D_s K \pi \pi$ data
 937 to define the Gaussian-constraints as discussed in Sec. 9. For the width of the Gaussians
 938 only the statistical error of the tagging calibration parameters are used since systematic
 939 uncertainties (except the systematic arising from the decay-time resolution which is already

included by the procedure described above) are found to be negligible, see Table 11.3.
 Finally, we take the biggest change in fit central value as the systematic for each parameter
 of the $B_s \rightarrow D_s K\pi\pi$ fits.

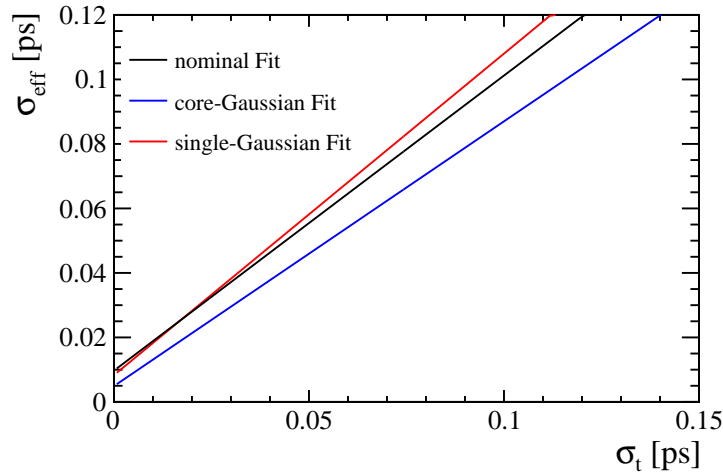


Figure 11.1: The measured resolution scaling function of the per-event decay time error estimate σ_t for fake B_s candidates (Run-II data) for (black line) the nominal scaling, (blue line) only using the narrow gaussian width of the double gaussian fit model or (red line) when determining the resolution using a single gaussian model.

11.5 Production, detection asymmetries and mixing frequency

The systematic from the production, detection asymmetries and Δm_s (in case of $B_s \rightarrow D_s K\pi\pi$ decays) which are fixed in the fit are evaluated by means of a toy study similar to the procedure performed for the time-acceptance. The parameters are assumed to be uncorrelated.

11.6 Multiple candidates

The fraction of events with multiple candidates has been found to be very small, it is 1.6% for $D_s K\pi\pi$ and 1.5% for $D_s \pi\pi\pi$. Thus the nominal result is obtained keeping all candidates, while a systematic uncertainty is assigned by repeating the fit randomly keeping only one candidate when multiple ones are founds. No shifts in the fit central values are observed.

11.7 Length and momentum scales

The uncertainty on the LHCb length scale is estimated to be at most 0.020% [55], which translates directly in an uncertainty on Δm_s of 0.020% with other parameters being unaffected. The momentum scale uncertainty is at most 0.022%.

958 11.8 Phase space acceptance

959 For the phase space acceptance we rely on simulated data. The integration error due
960 to the limited size of the MC sample used to normalize the signal PDF is evaluated by
961 bootstrapping the MC sample and repeating the full time-dependent amplitude fit.

962 To asses the uncertainty due to possible data-simulation differences, we determine
963 alternative phase space efficiencies by varying the selection requirements on quantities
964 that are expected not to be well described by the simulation. In particular, we consider
965 the following variations:

- 966 • No BDT cut is applied
- 967 • A tighter BDT requirement is used ($\text{BDTG} > 0.6$)
- 968 • No reweighting is applied
- 969 • Instead of the PID responses obtained from the `PIDCorr` tool, we use the `PIDGen`
970 tool to resample the PID variables [37]
- 971 • The raw MC PID variables are used
- 972 • Candidates with `BKGAT= 60` are removed

973 We assign the sample variance of the fitted values using the alternative phase space
974 acceptances as systematic.

975 This will be done when the final MC samples are available. We expect the integration
error to be negligible and the systematic error from data-simulation differences
to be small. At the moment we estimate a systematic by assuming a flat phase space
acceptance. The resulting uncertainties shown in Table 11.5 should be considered as
upper limit and illustrate that we are not highly sensitive to the details of the phase
space acceptance shape.

976 11.9 Resonance description

977 The following alternative line shape parameterizations are considered as part of the
978 systematic studies:

- 979 • The Lass description for the $K\pi$ S -wave is replaced by a more general model
980 (Glass [56, 57])
- 981 • The Gounaris-Sakurai description for the $\rho(770)$ is replaced by a relativistic Breit-
982 Wigner propagator (Equation 2.16)
- 983 • The ω contribution to the decay channel $K_1(1270) \rightarrow K \rho(770)/\omega$ is set to zero
- 984 • For the decay channel $K^*(1410) \rightarrow K \rho(770)$, we include $\rho(770) - \omega$ mixing with a
985 relative magnitude and phase determined from data
- 986 • Instead of taking the energy-dependent widths of the three-body resonances from
987 Refs. [9, 21], we derive them from Equation 2.17 taking only the dominant $K\pi\pi$
988 decay mode into account

989 The data fits are repeated for each alternative model and the RMS of the central values
990 are taken as systematic uncertainties.

991 The uncertainties due to fixed masses and widths of resonances are evaluated from
992 toys where we vary them one-by-one within their quoted errors. In our nominal fit, the
993 Blatt-Weisskopf radial parameter is set to $r_{BW} = 1.5 \text{ GeV}^{-1}$. Again, toys are generated
994 according to this nominal configuration and then fitted whereby the radial parameter is
995 uniformly varied within the interval $[0, 3] \text{ GeV}^{-1}$.

996 11.10 Alternative amplitude models

997 We tested several modifications of the LASSO model to assign an additional model
998 uncertainty to the measured observables r, δ and $\gamma - 2\beta_s$ as well as to the measured
999 masses and widths of the $K_1(1400)$ and $K^*(1410)$ resonances. The amplitude coefficients
1000 are by definition parameters of a given model which is why we do not evaluate a model
1001 uncertainty for them. The fit results of the following alternative models (Alt. 1 - Alt. 15)
1002 are summarized in Tables 11.1 and 11.2.

- 1003 • All amplitudes selected by Stage 1 of the model selection are included for both $b \rightarrow c$ and
1004 $b \rightarrow u$ transitions (Alt. 1)
- 1005 • The decay channels $K_1(1270)[D] \rightarrow K^*(892)\pi$, where the $K^*(892)\pi$ system is in relative
1006 a D-wave state, and $K_1(1400) \rightarrow K\rho(1450)$ are added (Alt. 2)
- 1007 • The decay channel $K_1(1400) \rightarrow K\rho(770)$ is added (Alt. 15)
- 1008 • The decay channels $K(1460) \rightarrow K\rho(770)$ and $K(1460) \rightarrow K\sigma$ are added (Alt. 3)
- 1009 • The $K(1460)$ resonance is removed (Alt. 12)
- 1010 • The decay channels $K^*(1680) \rightarrow K\rho(770)$ and $K^*(1680) \rightarrow K^*(892)\pi$ are added (Alt. 9)
- 1011 • The decay channel $K_2(1770) \rightarrow K^*(892)\pi$ is added (Alt. 10)
- 1012 • The amplitude $B_s \rightarrow (D_s K)_P \rho(770)$ is replaced by $B_s \rightarrow (D_s K)_S \rho(770)$ (Alt. 11)
- 1013 • Higher orbital angular momentum states are added for the amplitudes: $B_s \rightarrow (D_s \pi)_P K^*(892)$ and $B_s \rightarrow (D_s K)_P \rho(770)$ (Alt. 4 and Alt. 5)
- 1014 • The amplitudes $B_s \rightarrow (D_s \pi)_P K^*(892)$ and $B_s \rightarrow (D_s K)_P \rho(770)$ are removed (Alt. 14
1015 and Alt. 13)
- 1016 • The amplitudes $B_s \rightarrow (D_s K)_\sigma$, $B_s \rightarrow (D_s K)_f_0(980)$, $B_s \rightarrow (D_s K)_f_2(1270)$ and
1017 $B_s \rightarrow (D_s K)_f_0(1370)$ are added in different combinations and angular momentum
1018 configurations (Alt. 6, Alt. 7 and Alt. 8)
- 1019 • The decay channels $K_2^*(1430) \rightarrow K\rho(770)$ and $K_2^*(1430) \rightarrow K^*(892)\pi$ are added (not
1020 used)
- 1021 • The amplitudes $B_s \rightarrow (D_s \pi)_P K_0^*(1430)$ and $B_s \rightarrow (D_s K)_S K_2^*(1430)$ are added (not
1022 used)
- 1023 • A flat non-resonant $B_s \rightarrow D_s K \pi\pi$ component is added (not used)

1025 In total 20 different sets of amplitudes are fitted. In some cases, the fit fractions of
 1026 additionally added amplitudes turn out to be exactly zero. These model are effectively
 1027 not distinguishable from the baseline LASSO model and are not considered further. From
 1028 the remaining 15 models, we compute the sample variance for each observable and take it
 1029 as model uncertainty.

Table 11.1: Fit fractions in percent for the baseline and several alternative amplitude models (Alt. 1 - Alt. 7). Resonance parameters and the physical observables $r, \kappa, \delta, \gamma - 2\beta_s$ are also given. The values of the physical observables are given relative to the baseline result. The uncertainties are statistical only.

	Baseline	Alt.1	Alt.2	Alt.3	Alt.4	Alt.5	Alt.6	Alt.7
$B_s \rightarrow D_s (K_1(1270) \rightarrow K^*(892) \pi)$	5.4 ± 1.4	4.7 ± 1.6	7.3 ± 1.9	4.1 ± 1.5	3.6 ± 1.4	4.9 ± 1.7	6.7 ± 2.4	5.5 ± 0.8
$B_s \rightarrow D_s (K_1(1270)[D] \rightarrow K^*(892) \pi)$			1.0 ± 0.3					
$B_s \rightarrow D_s (K_1(1270) \rightarrow K \rho(770))$	9.4 ± 1.3	8.1 ± 2.2	8.1 ± 1.2	7.5 ± 1.7	9.1 ± 1.3	8.1 ± 1.4	10.8 ± 1.3	10.4 ± 1.4
$B_s \rightarrow D_s (K_1(1270) \rightarrow K \rho(1450))$			1.1 ± 0.6					
$B_s \rightarrow D_s (K_1(1270) \rightarrow K_2'(1430) \pi)$	4.4 ± 0.7	3.7 ± 0.9	2.8 ± 0.7	3.7 ± 0.6	4.2 ± 0.6	3.8 ± 0.6	3.8 ± 0.7	4.8 ± 0.6
$B_s \rightarrow D_s (K_1(1400) \rightarrow K^*(892) \pi)$	60.0 ± 5.6	61.7 ± 6.8	56.0 ± 3.9	62.4 ± 6.4	66.8 ± 5.6	62.7 ± 6.3	57.3 ± 5.4	57.2 ± 5.1
$B_s \rightarrow D_s (K_1(1400) \rightarrow K \rho(770))$								
$B_s \rightarrow D_s (K^*(1410) \rightarrow K^*(892) \pi)$	15.4 ± 1.1	15.4 ± 1.2	15.3 ± 0.9	16.2 ± 1.1	19.8 ± 2.0	15.2 ± 1.1	14.8 ± 1.0	15.1 ± 0.9
$B_s \rightarrow D_s (K^*(1410) \rightarrow K \rho(770))$	6.9 ± 0.7	6.6 ± 0.8	6.8 ± 0.7	6.8 ± 0.8	6.8 ± 0.7	6.9 ± 0.8	6.6 ± 0.7	6.5 ± 0.5
$B_s \rightarrow D_s (K_2^*(1430) \rightarrow K^*(892) \pi)$								
$B_s \rightarrow D_s (K_2^*(1430) \rightarrow K \rho(770))$								
$B_s \rightarrow D_s (K(1460) \rightarrow K^*(892) \pi)$			0.1 ± 0.3					
$B_s \rightarrow D_s (K(1460) \rightarrow K \sigma)$								
$B_s \rightarrow D_s (K^*(1680) \rightarrow K^*(892) \pi)$								
$B_s \rightarrow D_s (K^*(1680) \rightarrow K \rho(770))$								
$b \rightarrow c$								
$B_s \rightarrow D_s (K_2(1770) \rightarrow K^*(892) \pi)$								
$B_s \rightarrow (D_s \pi)_S K^*(892)$								
$B_s \rightarrow (D_s \pi)_P K^*(892)$	9.7 ± 1.7	11.9 ± 3.1	8.3 ± 1.2	10.3 ± 1.8	24.5 ± 2.6	8.7 ± 1.7	8.8 ± 1.4	9.8 ± 0.9
$B_s [P] \rightarrow (D_s \pi)_P K^*(892)$					1.6 ± 0.6			
$B_s [D] \rightarrow (D_s \pi)_P K^*(892)$					1.5 ± 0.2			
$B_s \rightarrow (D_s K)_S \sigma$							0.2 ± 0.2	
$B_s \rightarrow (D_s K)_P \sigma$							1.0 ± 0.5	
$B_s \rightarrow (D_s K)_S f_0(980)$								
$B_s \rightarrow (D_s K)_S f_2(1270)$							5.6 ± 2.8	
$B_s \rightarrow (D_s K)_P f_2(1270)$							6.2 ± 3.2	
$B_s \rightarrow (D_s K)_S f_0(1370)$								
$B_s \rightarrow (D_s K)_S \rho(770)$								
$B_s \rightarrow (D_s K)_P \rho(770)$		0.0 ± 0.1				0.2 ± 0.3		
$B_s [P] \rightarrow (D_s K)_P \rho(770)$						0.0 ± 0.0		
$B_s [D] \rightarrow (D_s K)_P \rho(770)$								
Sum	111.0 ± 5.6	112.3 ± 6.0	106.6 ± 4.2	111.0 ± 5.9	137.9 ± 7.0	110.6 ± 6.8	121.3 ± 7.7	110.6 ± 4.5
$B_s \rightarrow D_s (K_1(1270) \rightarrow K^*(892) \pi)$	19.3 ± 5.6	17.8 ± 5.7	20.6 ± 5.3	18.8 ± 4.6	13.6 ± 4.8	22.2 ± 7.4	16.9 ± 6.4	15.3 ± 4.2
$B_s \rightarrow D_s (K_1(1270)[D] \rightarrow K^*(892) \pi)$			2.7 ± 0.9					
$B_s \rightarrow D_s (K_1(1270) \rightarrow K \rho(770))$	33.9 ± 5.3	30.5 ± 6.2	22.8 ± 3.9	33.8 ± 4.6	34.5 ± 4.2	36.5 ± 6.3	27.6 ± 6.9	28.6 ± 4.3
$B_s \rightarrow D_s (K_1(1270) \rightarrow K \rho(1450))$			3.1 ± 1.7					
$B_s \rightarrow D_s (K_1(1270) \rightarrow K_2'(1430) \pi)$	15.7 ± 3.2	14.1 ± 3.4	7.7 ± 1.9	16.6 ± 2.8	16.0 ± 2.7	17.0 ± 3.7	9.7 ± 2.4	13.4 ± 2.9
$B_s \rightarrow D_s (K_1(1400) \rightarrow K^*(892) \pi)$	15.2 ± 8.3	23.4 ± 10.7	14.3 ± 8.0	16.4 ± 7.3	17.3 ± 6.2	14.5 ± 8.0	11.8 ± 7.6	11.0 ± 6.1
$B_s \rightarrow D_s (K_1(1400) \rightarrow K \rho(770))$								
$B_s \rightarrow D_s (K^*(1410) \rightarrow K^*(892) \pi)$		3.5 ± 2.2						
$B_s \rightarrow D_s (K^*(1410) \rightarrow K \rho(770))$		1.5 ± 0.9						
$B_s \rightarrow D_s (K_2^*(1430) \rightarrow K^*(892) \pi)$								
$B_s \rightarrow D_s (K_2^*(1430) \rightarrow K \rho(770))$								
$b \rightarrow u$								
$B_s \rightarrow D_s (K(1460) \rightarrow K^*(892) \pi)$	19.7 ± 4.4	13.4 ± 3.8	13.2 ± 3.1	14.6 ± 3.9	14.9 ± 3.4	19.3 ± 4.3	25.2 ± 4.5	19.8 ± 4.1
$B_s \rightarrow D_s (K(1460) \rightarrow K \rho(770))$			2.7 ± 1.0					
$B_s \rightarrow D_s (K(1460) \rightarrow K \sigma)$			1.7 ± 0.8					
$B_s \rightarrow D_s (K^*(1680) \rightarrow K^*(892) \pi)$							13.2 ± 7.3	
$B_s \rightarrow D_s (K^*(1680) \rightarrow K \rho(770))$							14.2 ± 8.6	
$B_s \rightarrow D_s (K_2(1770) \rightarrow K^*(892) \pi)$								
$B_s \rightarrow (D_s \pi)_S K^*(892)$								
$B_s \rightarrow (D_s \pi)_P K^*(892)$	20.6 ± 7.6	13.0 ± 7.6	25.1 ± 5.6	17.6 ± 5.7	21.3 ± 4.9	20.7 ± 5.8	25.8 ± 5.7	27.4 ± 6.6
$B_s [P] \rightarrow (D_s \pi)_P K^*(892)$					1.4 ± 0.7			
$B_s [D] \rightarrow (D_s \pi)_P K^*(892)$					1.3 ± 0.3			
$B_s \rightarrow (D_s K)_S \sigma$							0.8 ± 0.8	
$B_s \rightarrow (D_s K)_P \sigma$							3.4 ± 2.1	
$B_s \rightarrow (D_s K)_S f_0(980)$								
$B_s \rightarrow (D_s K)_S f_2(1270)$								
$B_s \rightarrow (D_s K)_P f_2(1270)$								
$B_s \rightarrow (D_s K)_S f_0(1370)$								
$B_s \rightarrow (D_s K)_S \rho(770)$								
$B_s \rightarrow (D_s K)_P \rho(770)$	12.7 ± 3.0	9.2 ± 3.6	6.0 ± 2.3	14.6 ± 2.9	11.8 ± 1.3	26.3 ± 6.4	6.7 ± 2.7	8.5 ± 2.3
$B_s [P] \rightarrow (D_s K)_P \rho(770)$						1.6 ± 1.2		
$B_s [D] \rightarrow (D_s K)_P \rho(770)$						3.2 ± 0.8		
Sum	137.10 ± 12.46	126.42 ± 15.96	115.59 ± 11.62	136.63 ± 10.96	132.03 ± 8.99	161.15 ± 16.74	152.72 ± 19.36	128.13 ± 8.71
$m_{K_1(1400)}$ [MeV]	1394.78 ± 8.81	1397.03 ± 9.07	1387.59 ± 7.11	1396.89 ± 7.64	1407.60 ± 7.69	1392.08 ± 8.82	1391.75 ± 8.27	1396.82 ± 6.22
$\Gamma_{K_1(1400)}$ [MeV]	223.96 ± 15.92	222.77 ± 17.25	208.30 ± 14.13	232.17 ± 17.17	255.39 ± 19.40	227.83 ± 17.15	213.57 ± 17.48	221.52 ± 11.07
$m_{K^*(1410)}$ [MeV]	1419.59 ± 10.99	1422.77 ± 11.90	1421.88 ± 12.04	1417.49 ± 10.56	1450.00 ± 3.97	1422.76 ± 9.27	1423.13 ± 12.47	1427.06 ± 9.25
$\Gamma_{K^*(1410)}$ [MeV]	342.42 ± 23.60	337.83 ± 23.42	342.27 ± 21.98	342.23 ± 22.67	400.00 ± 87.91	334.80 ± 22.56	340.46 ± 24.52	337.29 ± 22.57
r	0.00 ± 0.04	0.09 ± 0.06	-0.01 ± 0.04	0.04 ± 0.04	-0.01 ± 0.03	0.01 ± 0.05	-0.03 ± 0.04	-0.02 ± 0.03
κ	0.00 ± 0.06	0.10 ± 0.07	0.02 ± 0.06	-0.10 ± 0.05	0.02 ± 0.06	-0.05 ± 0.07	-0.03 ± 0.08	-0.07 ± 0.06
δ [$^\circ$]	0.00 ± 16.23	-3.59 ± 13.85	1.50 ± 15.52	-7.53 ± 16.62	1.68 ± 14.53	-0.11 ± 18.64	3.16 ± 15.71	1.73 ± 14.47
$\gamma - 2\beta_s$ [$^\circ$]	0.00 ± 16.28	2.93 ± 15.21	-8.17 ± 15.24	-5.01 ± 16.25	-2.08 ± 14.74	7.45 ± 19.14	1.37 ± 15.45	2.70 ± 15.55

Table 11.2: Fit fractions in percent for several alternative amplitude models (Alt. 8 - Alt. 15). Resonance parameters and the physical observables $r, \kappa, \delta, \gamma - 2\beta_s$ are also given. The values of the physical observables are given relative to the baseline result. The uncertainties are statistical only.

	Alt.8	Alt.9	Alt.10	Alt.11	Alt.12	Alt.13	Alt.14	Alt.15
$B_s \rightarrow D_s (K_1(1270) \rightarrow K^*(892) \pi)$	6.1 ± 1.8	5.1 ± 1.4	5.1 ± 1.8	6.4 ± 1.7	4.1 ± 1.4	7.3 ± 2.0	7.3 ± 4.4	6.2 ± 1.5
$B_s \rightarrow D_s (K_1(1270) [D] \rightarrow K^*(892) \pi)$								
$B_s \rightarrow D_s (K_1(1270) \rightarrow K \rho(770))$	10.9 ± 1.8	10.3 ± 1.2	8.7 ± 1.2	10.8 ± 1.8	9.9 ± 1.6	13.8 ± 2.0	9.9 ± 1.7	13.2 ± 3.0
$B_s \rightarrow D_s (K_1(1270) \rightarrow K \rho(1450))$								
$B_s \rightarrow D_s (K_1(1270) \rightarrow K^*_s(1430) \pi)$	4.2 ± 0.8	4.2 ± 0.7	4.4 ± 0.7	4.6 ± 0.8	4.5 ± 0.8	4.8 ± 0.7	4.9 ± 0.9	4.7 ± 0.8
$B_s \rightarrow D_s (K_1(1400) \rightarrow K^*(892) \pi)$	55.7 ± 6.2	61.6 ± 5.2	64.3 ± 5.4	56.9 ± 7.4	62.4 ± 4.0	53.5 ± 6.0	87.3 ± 11.2	60.6 ± 5.5
$B_s \rightarrow D_s (K_1(1400) \rightarrow K \rho(770))$								0.6 ± 0.5
$B_s \rightarrow D_s (K^*(1410) \rightarrow K^*(892) \pi)$	15.2 ± 1.2	18.2 ± 1.5	14.6 ± 1.0	15.4 ± 1.2	15.1 ± 1.1	15.4 ± 1.1	13.8 ± 0.9	15.0 ± 0.9
$B_s \rightarrow D_s (K^*(1410) \rightarrow K \rho(770))$	7.0 ± 0.6	5.4 ± 1.2	7.0 ± 0.6	6.7 ± 0.7	6.1 ± 0.6	6.4 ± 0.6	6.1 ± 0.6	6.5 ± 0.6
$B_s \rightarrow D_s (K_2^*(1430) \rightarrow K^*(892) \pi)$								
$B_s \rightarrow D_s (K_2^*(1430) \rightarrow K \rho(770))$								
$B_s \rightarrow D_s (K(1460) \rightarrow K^*(892) \pi)$								
$B_s \rightarrow D_s (K(1460) \rightarrow K \rho(770))$								
$B_s \rightarrow D_s (K(1460) \rightarrow K \sigma)$								
$B_s \rightarrow D_s (K^*(1680) \rightarrow K^*(892) \pi)$		0.6 ± 0.1						
$B_s \rightarrow D_s (K^*(1680) \rightarrow K \rho(770))$		2.0 ± 0.7						
$b \rightarrow c$				0.3 ± 0.2				
$B_s \rightarrow D_s (K_2(1770) \rightarrow K^*(892) \pi)$								
$B_s \rightarrow (D_s \pi)_S K^*(892)$								
$B_s \rightarrow (D_s \pi)_P K^*(892)$	6.7 ± 1.9	10.6 ± 1.4	9.5 ± 1.6	8.5 ± 3.0	13.4 ± 2.3	7.4 ± 2.3		9.3 ± 1.6
$B_s [P] \rightarrow (D_s \pi)_P K^*(892)$								
$B_s [D] \rightarrow (D_s \pi)_P K^*(892)$								
$B_s \rightarrow (D_s K)_S \sigma$	0.2 ± 0.1							
$B_s \rightarrow (D_s K)_P \sigma$								
$B_s \rightarrow (D_s K)_S f_0(980)$	0.0 ± 0.1							
$B_s \rightarrow (D_s K)_S f_0(1270)$	0.5 ± 0.4							
$B_s \rightarrow (D_s K)_P f_2(1270)$								
$B_s \rightarrow (D_s K)_S f_0(1370)$								
$B_s \rightarrow (D_s K)_S \rho(770)$								
$B_s \rightarrow (D_s K)_P \rho(770)$								
$B_s [P] \rightarrow (D_s K)_P \rho(770)$								
$B_s [D] \rightarrow (D_s K)_P \rho(770)$								
Sum	106.6 ± 6.9	118.0 ± 5.2	113.8 ± 5.9	109.2 ± 7.6	115.5 ± 5.2	108.7 ± 7.3	129.3 ± 14.8	116.1 ± 7.1
$B_s \rightarrow D_s (K_1(1270) \rightarrow K^*(892) \pi)$	17.7 ± 4.5	17.0 ± 4.9	21.9 ± 6.2	17.2 ± 4.3	18.5 ± 5.1	11.5 ± 5.9	27.1 ± 18.1	15.7 ± 4.6
$B_s \rightarrow D_s (K_1(1270) [D] \rightarrow K^*(892) \pi)$								
$B_s \rightarrow D_s (K_1(1270) \rightarrow K \rho(770))$	31.4 ± 5.3	34.2 ± 6.0	37.6 ± 6.1	29.0 ± 6.5	44.5 ± 5.3	21.9 ± 7.7	37.1 ± 6.8	33.5 ± 6.2
$B_s \rightarrow D_s (K_1(1270) \rightarrow K \rho(1450))$								
$B_s \rightarrow D_s (K_1(1270) \rightarrow K^*_s(1430) \pi)$	12.0 ± 3.1	14.0 ± 3.1	18.8 ± 3.1	12.3 ± 3.4	20.2 ± 3.3	7.6 ± 3.2	18.1 ± 3.7	11.8 ± 2.9
$B_s \rightarrow D_s (K_1(1400) \rightarrow K^*(892) \pi)$	8.9 ± 8.7	13.4 ± 7.0	16.0 ± 8.1	14.2 ± 10.0	43.8 ± 5.1	5.9 ± 8.4	43.1 ± 26.1	13.2 ± 7.0
$B_s \rightarrow D_s (K_1(1400) \rightarrow K \rho(770))$								0.1 ± 0.2
$B_s \rightarrow D_s (K^*(1410) \rightarrow K^*(892) \pi)$								
$B_s \rightarrow D_s (K^*(1410) \rightarrow K \rho(770))$								
$B_s \rightarrow D_s (K_2^*(1430) \rightarrow K^*(892) \pi)$								
$B_s \rightarrow D_s (K_2^*(1430) \rightarrow K \rho(770))$								
$B_s \rightarrow D_s (K(1460) \rightarrow K^*(892) \pi)$	21.2 ± 5.6	20.4 ± 3.8	16.9 ± 3.6	21.5 ± 5.8		25.4 ± 6.4	18.6 ± 5.1	22.0 ± 4.5
$B_s \rightarrow D_s (K(1460) \rightarrow K \rho(770))$								
$B_s \rightarrow D_s (K(1460) \rightarrow K \sigma)$								
$B_s \rightarrow D_s (K^*(1680) \rightarrow K^*(892) \pi)$		0.9 ± 0.5						
$B_s \rightarrow D_s (K^*(1680) \rightarrow K \rho(770))$		2.9 ± 2.0						
$b \rightarrow u$			1.9 ± 1.2					
$B_s \rightarrow D_s (K_2(1770) \rightarrow K^*(892) \pi)$								
$B_s \rightarrow (D_s \pi)_S K^*(892)$								
$B_s \rightarrow (D_s \pi)_P K^*(892)$	34.0 ± 9.7	18.4 ± 6.2	17.7 ± 4.6	26.8 ± 14.0	15.1 ± 7.2	41.0 ± 14.2		22.1 ± 7.1
$B_s [P] \rightarrow (D_s \pi)_P K^*(892)$								
$B_s [D] \rightarrow (D_s \pi)_P K^*(892)$								
$B_s \rightarrow (D_s K)_S \sigma$	0.1 ± 0.2							
$B_s \rightarrow (D_s K)_P \sigma$								
$B_s \rightarrow (D_s K)_S f_0(980)$	0.0 ± 0.1							
$B_s \rightarrow (D_s K)_S f_2(1270)$	0.3 ± 0.3							
$B_s \rightarrow (D_s K)_P f_2(1270)$								
$B_s \rightarrow (D_s K)_S f_0(1370)$								
$B_s \rightarrow (D_s K)_S \rho(770)$								
$B_s \rightarrow (D_s K)_P \rho(770)$	10.7 ± 2.7	9.2 ± 2.9	11.5 ± 3.9		10.8 ± 6.0		18.0 ± 5.3	11.5 ± 3.6
$B_s [P] \rightarrow (D_s K)_P \rho(770)$								
$B_s [D] \rightarrow (D_s K)_P \rho(770)$								
Sum	136.22 ± 10.51	130.46 ± 12.34	142.42 ± 12.82	126.45 ± 10.70	153.02 ± 18.86	113.38 ± 10.28	162.01 ± 41.78	130.00 ± 12.19
$m_{K_1}(1400)$ [MeV]	1391.27 ± 9.25	1397.57 ± 6.33	1394.93 ± 8.20	1393.59 ± 7.19	1403.29 ± 8.58	1395.22 ± 9.04	1317.87 ± 6.33	1391.38 ± 7.22
$\Gamma_{K_1(1400)}$ [MeV]	214.03 ± 14.78	220.70 ± 12.71	231.66 ± 16.22	216.71 ± 16.50	247.44 ± 14.61	204.52 ± 15.63	268.86 ± 18.02	220.23 ± 15.44
$m_{K^*(1410)}$ [MeV]	1418.20 ± 10.95	1400.00 ± 24.66	1414.48 ± 10.92	1420.61 ± 12.24	1427.26 ± 10.17	1421.39 ± 11.40	1434.97 ± 12.69	1424.12 ± 11.89
$\Gamma_{K^*(1410)}$ [MeV]	346.46 ± 22.97	400.00 ± 61.76	343.15 ± 21.51	343.25 ± 23.44	345.02 ± 24.03	339.87 ± 24.08	341.72 ± 23.38	343.04 ± 22.77
r	0.01 ± 0.04	0.02 ± 0.05	-0.01 ± 0.04	-0.01 ± 0.04	-0.08 ± 0.03	-0.02 ± 0.04	-0.07 ± 0.03	-0.02 ± 0.05
κ	-0.02 ± 0.05	0.08 ± 0.06	-0.02 ± 0.07	-0.03 ± 0.05	-0.22 ± 0.09	-0.10 ± 0.08	-0.12 ± 0.10	-0.12 ± 0.07
$\delta [^\circ]$	0.36 ± 14.93	3.72 ± 15.26	6.60 ± 17.24	-4.30 ± 15.61	2.30 ± 23.04	-10.27 ± 15.61	-8.69 ± 21.31	-3.14 ± 15.85
$\gamma - 2\beta_s [^\circ]$	7.48 ± 18.07	4.20 ± 15.79	-0.98 ± 17.39	5.73 ± 17.13	-2.08 ± 18.51	2.09 ± 21.13	10.22 ± 19.05	0.68 ± 16.09

Table 11.3: Systematic uncertainties on the fit parameters of the fit to $B_s \rightarrow D_s\pi\pi\pi$ data in units of statistical standard deviations.

Fit Parameter	Fit-bias	Acceptance	Resolution	Asymmetries	Background	Mult.-Cand.	Mom./z-Scale	Total
p_0^{OS} Run-I	0.04	0.00	0.99	0.01	0.04	0.00		0.99
p_1^{OS} Run-I	0.01	0.00	1.03	0.00	0.05	0.00		1.03
Δp_0^{OS} Run-I	0.03	0.00	0.02	0.15	0.02	0.00		0.16
Δp_1^{OS} Run-I	0.02	0.00	0.03	0.16	0.02	0.00		0.16
ϵ_{tag}^{OS} Run-I	0.02	0.00	0.00	0.01	0.09	0.00		0.09
$\Delta \epsilon_{tag}^{OS}$ Run-I	0.03	0.00	0.07	0.01	0.02	0.00		0.07
p_0^{SS} Run-I	0.01	0.00	0.55	0.00	0.03	0.00		0.55
p_1^{SS} Run-I	0.04	0.00	0.60	0.01	0.03	0.00		0.60
Δp_0^{SS} Run-I	0.00	0.00	0.00	0.10	0.01	0.00		0.10
Δp_1^{SS} Run-I	0.07	0.00	0.01	0.12	0.03	0.00		0.15
ϵ_{tag}^{SS} Run-I	0.02	0.00	0.00	0.01	0.01	0.00		0.03
$\Delta \epsilon_{tag}^{SS}$ Run-I	0.04	0.00	0.05	0.01	0.02	0.00		0.07
p_0^{OS} Run-II	0.01	0.01	1.65	0.00	0.10	0.00		1.65
p_1^{OS} Run-II	0.01	0.00	1.37	0.00	0.10	0.00		1.38
Δp_0^{OS} Run-II	0.05	0.00	0.06	0.00	0.03	0.00		0.08
Δp_1^{OS} Run-II	0.02	0.00	0.03	0.00	0.04	0.00		0.05
ϵ_{tag}^{OS} Run-II	0.02	0.00	0.00	0.00	0.04	0.00		0.05
$\Delta \epsilon_{tag}^{OS}$ Run-II	0.01	0.00	0.21	0.00	0.04	0.00		0.22
p_0^{SS} Run-II	0.00	0.00	1.06	0.00	0.03	0.00		1.06
p_1^{SS} Run-II	0.07	0.00	1.22	0.00	0.03	0.00		1.22
Δp_0^{SS} Run-II	0.00	0.00	0.02	0.00	0.03	0.00		0.04
Δp_1^{SS} Run-II	0.07	0.00	0.03	0.00	0.03	0.00		0.08
ϵ_{tag}^{SS} Run-II	0.00	0.00	0.00	0.00	0.04	0.00		0.04
$\Delta \epsilon_{tag}^{SS}$ Run-II	0.02	0.00	0.05	0.00	0.02	0.00		0.06
A_P Run-II	0.10	0.00	0.10	0.01	0.03	0.00		0.14
Δm_s	0.01	0.00	0.15	0.03	0.06	0.00	0.61	0.63

Table 11.4: Systematic uncertainties on the fit parameters of the phase-space integrated fit to $B_s \rightarrow D_s K\pi\pi$ data in units of statistical standard deviations.

Fit Parameter	Fit bias	Acceptance	Resolution	Δm_s	Asymmetries	Background	Total
C	0.02	0.04	0.07	0.06	0.03	0.09	0.14
D	0.04	0.26	0.00	0.02	0.05	0.11	0.29
\bar{D}	0.05	0.26	0.01	0.02	0.05	0.16	0.32
S	0.01	0.02	0.03	0.24	0.03	0.15	0.29
\bar{S}	0.04	0.03	0.06	0.23	0.03	0.13	0.27

Table 11.5: Systematic uncertainties on the fit parameters of the full time-dependent amplitude fit to $B_s \rightarrow D_s K\pi\pi$ data in units of statistical standard deviations.

Fit Parameter	Fit bias	Time-Acc.	Resolution	Δm_s	Asymmetries	Background	Lineshapes	Resonances m, Γ	Form-Factors	Phsp-Acc.	Amp. Model	Total
$B_s \rightarrow D_s(K_1(1270) \rightarrow K^*(892)\pi)$ Mag	0.04	0.17	0.01	0.01	0.02	0.15	0.42	0.22	0.54	0.00		0.76
$B_s \rightarrow D_s(K_1(1270) \rightarrow K^*(892)\pi)$ Phase	0.08	0.20	0.03	0.01	0.10	0.06	0.29	0.27	0.34	0.88		1.05
$B_s \rightarrow D_s(K_1(1270) \rightarrow K_0^*(1430)\pi)$ Mag	0.07	0.17	0.02	0.01	0.07	0.25	0.15	0.14	0.20	2.17		2.21
$B_s \rightarrow D_s(K_1(1270) \rightarrow K_0^*(1430)\pi)$ Phase	0.24	0.16	0.02	0.01	0.12	0.15	0.31	0.15	0.50	1.72		1.86
$B_s \rightarrow D_s(K_1(1400) \rightarrow K^*(892)\pi)$ Mag($b \rightarrow c$)	0.08	0.13	0.02	0.03	0.29	0.27	0.14	0.20	0.28	1.19		1.32
$B_s \rightarrow D_s(K_1(1400) \rightarrow K^*(892)\pi)$ Phase($b \rightarrow c$)	0.07	0.24	0.01	0.03	0.09	0.28	0.18	0.24	0.43	0.59		0.88
$B_s \rightarrow D_s(K_1(1400) \rightarrow K^*(892)\pi)$ Mag($b \rightarrow u$)	0.21	0.19	0.02	0.04	0.04	0.19	0.13	0.20	0.63	2.56		2.67
$B_s \rightarrow D_s(K_1(1400) \rightarrow K^*(892)\pi)$ Phase($b \rightarrow u$)	0.01	0.16	0.04	0.10	0.09	0.36	0.27	0.21	0.29	1.01		1.18
$B_s \rightarrow D_s(K^*(1410) \rightarrow K^*(892)\pi)$ Mag($b \rightarrow c$)	0.32	0.13	0.03	0.05	0.07	0.18	0.22	0.11	0.32	0.02		0.57
$B_s \rightarrow D_s(K^*(1410) \rightarrow K^*(892)\pi)$ Phase($b \rightarrow c$)	0.25	0.23	0.01	0.01	0.13	0.10	0.29	0.20	0.74	0.66		1.12
$B_s \rightarrow D_s(K^*(1410) \rightarrow K\rho(770))$ Mag	0.49	0.20	0.01	0.01	0.08	0.17	0.34	0.10	0.31	0.11		0.74
$B_s \rightarrow D_s(K^*(1410) \rightarrow K\rho(770))$ Phase	0.23	0.22	0.01	0.01	0.06	0.13	0.19	0.11	0.31	1.47		1.56
$B_s \rightarrow D_s(K(1460) \rightarrow K^*(892)\pi)$ Mag($b \rightarrow u$)	0.03	0.24	0.02	0.03	0.15	0.22	0.14	0.17	0.27	2.40		2.45
$B_s \rightarrow D_s(K(1460) \rightarrow K^*(892)\pi)$ Phase($b \rightarrow u$)	0.02	0.30	0.03	0.04	0.09	0.21	0.28	0.40	0.39	0.61		0.96
$B_s \rightarrow (D_s\pi)_P K^*(892)$ Mag($b \rightarrow c$)	0.15	0.16	0.02	0.02	0.25	0.24	0.16	0.13	0.46	0.72		0.97
$B_s \rightarrow (D_s\pi)_P K^*(892)$ Phase($b \rightarrow c$)	0.01	0.20	0.01	0.01	0.13	0.47	0.21	0.18	0.42	0.49		0.88
$B_s \rightarrow (D_s\pi)_P K^*(892)$ Mag($b \rightarrow u$)	0.15	0.14	0.04	0.03	0.33	0.13	0.17	0.17	0.26	0.71		0.89
$B_s \rightarrow (D_s\pi)_P K^*(892)$ Phase($b \rightarrow u$)	0.01	0.26	0.05	0.03	0.56	0.28	0.30	0.21	0.58	0.39		1.04
$B_s \rightarrow (D_sK)_P \rho(770)$ Mag($b \rightarrow u$)	0.45	0.24	0.01	0.05	0.34	0.49	0.35	0.30	0.59	0.14		1.10
$B_s \rightarrow (D_sK)_P \rho(770)$ Phase($b \rightarrow u$)	0.31	0.31	0.02	0.03	0.10	0.66	0.39	0.35	0.69	1.70		2.07
$m_{K_1(1400)}$	0.04	0.18	0.02	0.01	0.24	0.17	0.16	0.12	0.41	0.56		2.48
$\Gamma_{K_1(1400)}$	0.05	0.22	0.02	0.01	0.19	0.13	0.36	0.10	0.42	0.25		1.32
$m_{K^*(1410)}$	0.08	0.19	0.01	0.01	0.34	0.11	0.30	0.05	1.45	0.53		0.90
$\Gamma_{K^*(1410)}$	0.30	0.17	0.01	0.01	0.07	0.18	0.14	0.05	1.64	0.30		0.89
r	0.07	0.19	0.05	0.10	0.18	0.29	0.11	0.22	0.22	0.99		1.16
δ	0.02	0.17	0.04	0.05	0.03	0.10	0.11	0.03	0.13	0.31		0.51
$\gamma - 2\beta_s$	0.01	0.11	0.05	0.07	0.18	0.25	0.13	0.03	0.08	0.47		0.67

1030 A Stripping and Trigger cuts

1031 The following text describes variables which are used in Table 1.1 and might be ambiguous,
 1032 or which benefits are not straight forward. Where noted, different cut values are applied
 1033 for Run-I and Run-II data. In Table 1.1, DOCA is the abbreviation for distance of closest
 1034 approach. This variable is used to ensure that all D_s and $X_{s,d}$ daughters originate from
 1035 the same vertex. DIRA is the abbreviation for the cosine of the angle θ between the
 hadron's flight direction \vec{x} and it's corresponding momentum vector \vec{p} , $\cos \theta_{\vec{x}-\vec{p}}$.

Table 1.1: Summary of the stripping selections for $B_s^0 \rightarrow D_s K \pi \pi$ decays. The requirements for Run-II are only given if they have been changed.

Variable	Stripping Cut (Run-I)	Stripping Cut (Run-II)
Track χ^2/nDoF	< 3	
Track p	$> 1000 \text{ MeV}/c$	
Track p_T	$> 100 \text{ MeV}/c$	
Track IP χ^2	> 4	
Track ghost-prob.	< 0.4	
D_s mass	$m_{D_s} \pm 100 \text{ MeV}$	$m_{D_s} \pm 80 \text{ MeV}$
D_s Daughter p_T	$\sum_{i=1}^3 p_{t,i} > 1800 \text{ MeV}/c$	
D_s Daughter DOCA	$< 0.5 \text{ mm}$	
D_s Vertex χ^2/nDoF	< 10	
D_s χ^2 -separation from PV	> 36	
D_s daughter PID(π)	< 20	
D_s daughter PID(K)	> -10	
$X_{s,d}$ mass	$< 4000 \text{ MeV}$	$< 3500 \text{ MeV}$
$X_{s,d}$ Daughter p	$> 2 \text{ GeV}/c$	
$X_{s,d}$ Daughter DOCA	$< 0.4 \text{ mm}$	
$X_{s,d}$ Daughter p_T	$\sum_{i=1}^3 p_{t,i} > 1250 \text{ MeV}/c$	
$X_{s,d}$ Vertex χ^2/nDoF	< 8	
$X_{s,d}$ χ^2 -separation from PV	> 16	
$X_{s,d}$ DIRA	> 0.98	
$X_{s,d}$ $\Delta\rho$	$> 0.1 \text{ mm}$	
$X_{s,d}$ Δz	$> 2.0 \text{ mm}$	
$X_{s,d}$ daughter PID(π)	< 10	
X_s daughter PID(K)	> -2	> 4
B_s^0 mass	$[4750, 7000] \text{ MeV}/c^2$	$[5000, 6000] \text{ MeV}/c^2$
B_s^0 DIRA	> 0.98	> 0.99994
B_s^0 min IP χ^2	< 25	< 20
B_s^0 Vertex χ^2/nDoF	< 10	< 8
$B_s^0 \tau_{B_s^0}$	$> 0.2 \text{ ps}$	

1036

1037 Table 1.2 summarizes the trigger requirements imposed by the Hlt1 line used in this
 1038 analysis for Run-I. At least one of the six decay particles must pass the listed requirements
 1039 in order for the event to be stored for further analysis. For Run-II, this trigger line was
 1040 updated and uses a multivariate classifier which takes the variables listed in Table 1.2 as
 1041 input, rather than directly cutting on them.

1042 The Hlt2 2, 3 and 4-body topological lines use a Boosted Decision Tree based on the
 1043 b-hadron p_T , its flight distance χ^2 from the nearest PV and the sum of the B_s^0 and D_s
 1044 vertex χ^2 divided by the sum of their number of degrees of freedom. Table 1.3 summarizes
 1045 the cuts applied by the inclusive ϕ trigger, which requires that a $\phi \rightarrow KK$ candidate can
 be formed out of two tracks present in the event.

Table 1.2: Summary of the cuts applied by the Hlt1TrackAllL0 trigger for Run-I. At least one of the six decay particles must pass this requirements, in order for the event to be accepted.

Quantity	Hlt1TrackAllL0 requirement
Track IP [mm]	> 0.1
Track IP χ^2	> 16
Track χ^2/nDoF	< 2.5
Track p_T	> 1.7 GeV/c
Track p	> 10 GeV/c
Number VELO hits/track	> 9
Number missed VELO hits/track	< 3
Number OT+IT $\times 2$ hits/track	> 16

Table 1.3: Summary of the cuts applied by the Hlt2 inclusive ϕ trigger. A $\phi \rightarrow KK$ candidate, formed by two tracks in the event, must pass this requirements in order for the event to be accepted.

Quantity	Hlt2IncPhi requirement
ϕ mass	$m_\phi \pm 12$ MeV/ c^2 of PDG value
ϕp_T	> 2.5 GeV/c
ϕ vertex χ^2/nDoF	< 20
ϕ IP χ^2 to any PV	> 5

1046

B Details of multivariate classifier

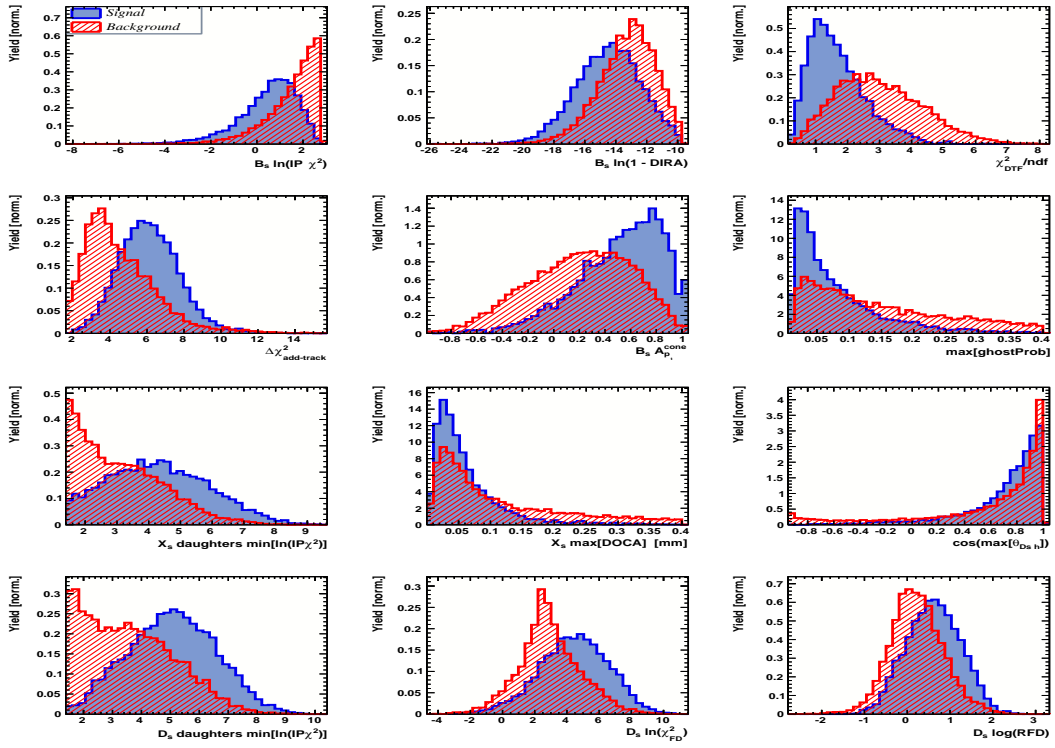


Figure A.1: Variables used to train the BDTG for category [Run-I,L0-TOS].

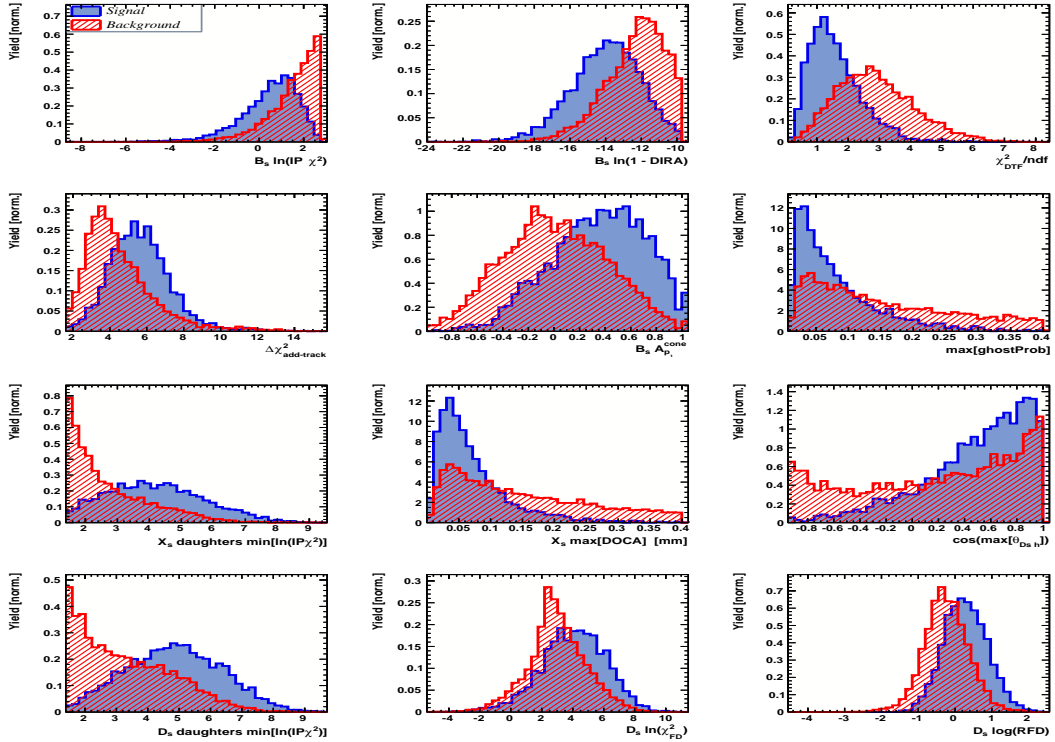


Figure A.2: Variables used to train the BDTG for category [Run-I,L0-TIS].

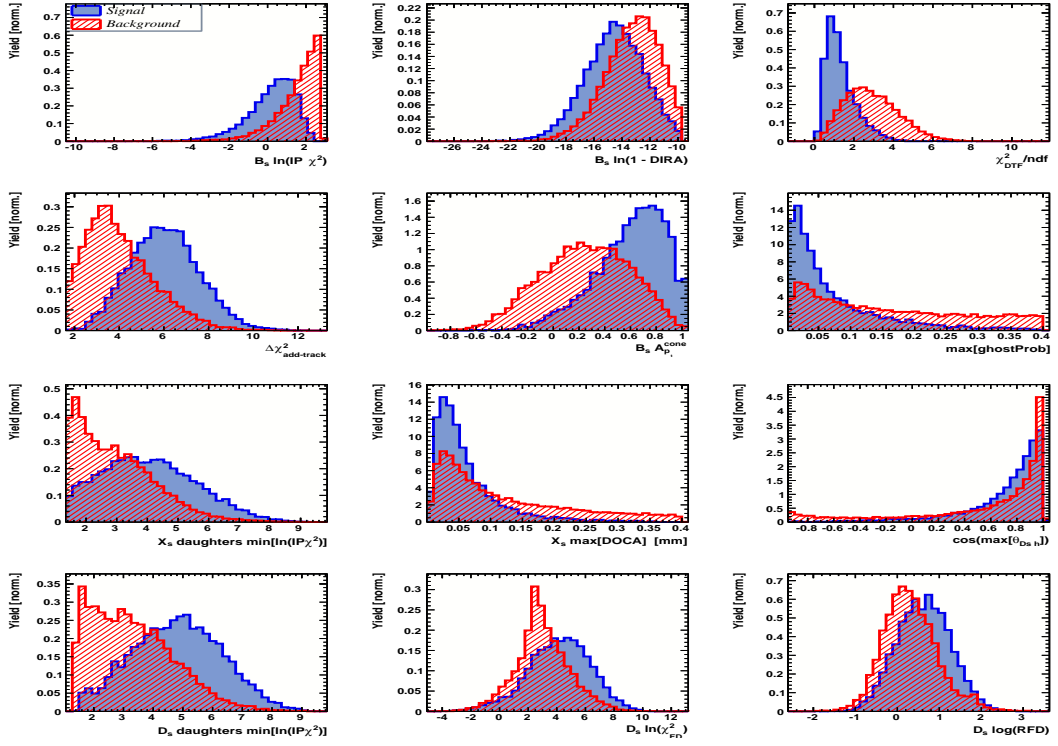


Figure A.3: Variables used to train the BDTG for category [Run-II,L0-TOS].

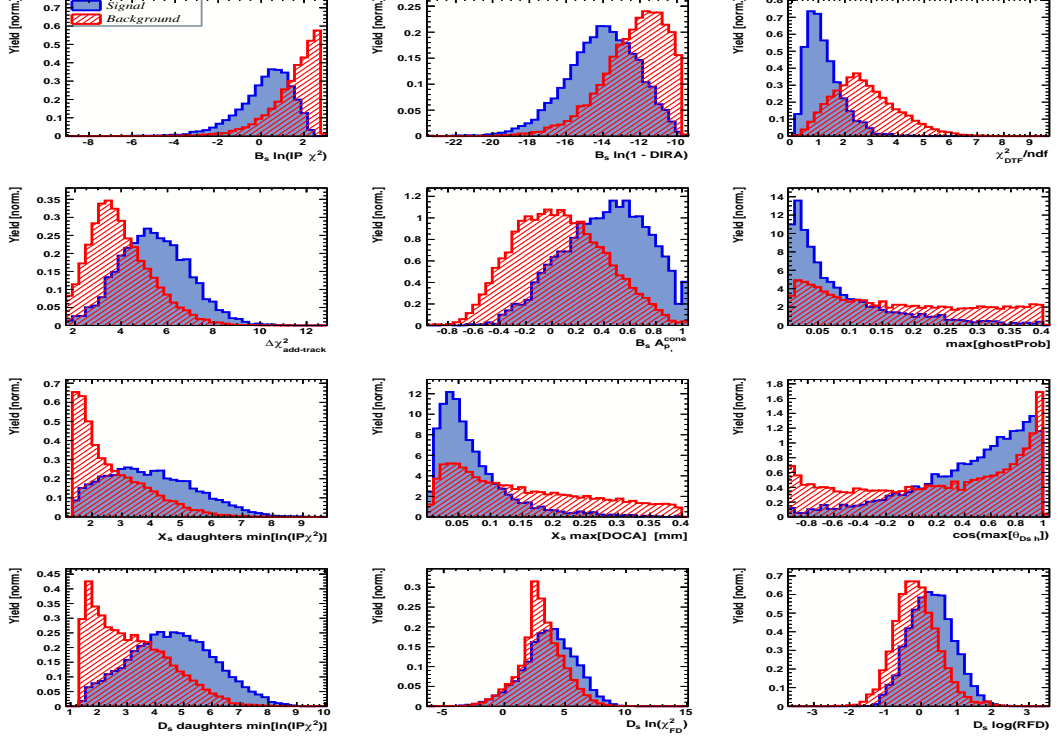


Figure A.4: Variables used to train the BDTG for category [Run-II,L0-TIS].

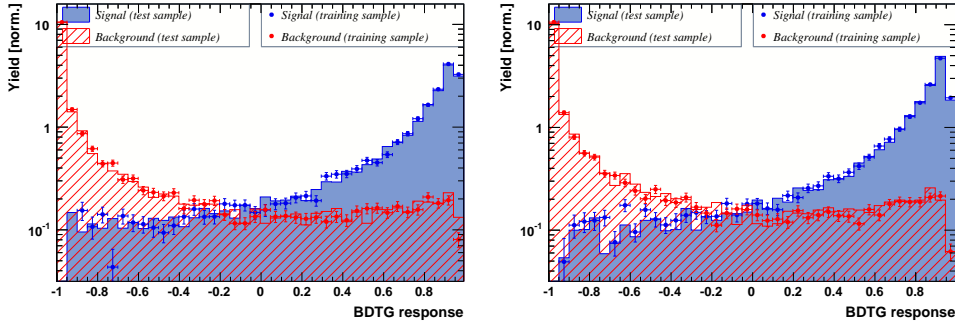


Figure A.5: Response of the classifier trained on the even and tested on the odd sample (left) and trained on the odd and tested on the even sample (right) for category [Run-I,L0-TOS].

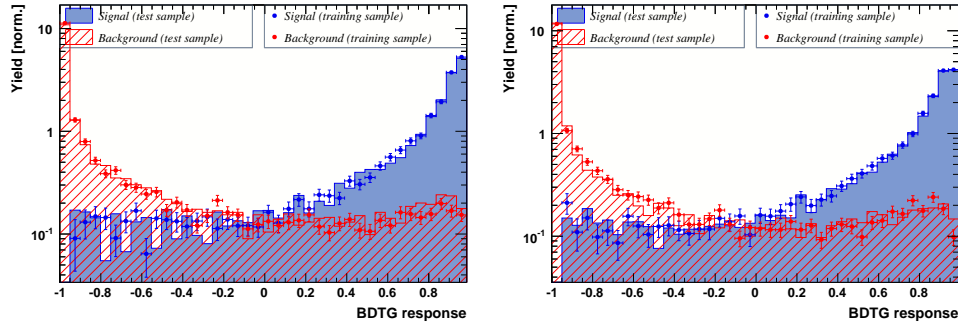


Figure A.6: Response of the classifier trained on the even and tested on the odd sample (left) and trained on the odd and tested on the even sample (right) for category [Run-I,L0-TIS].

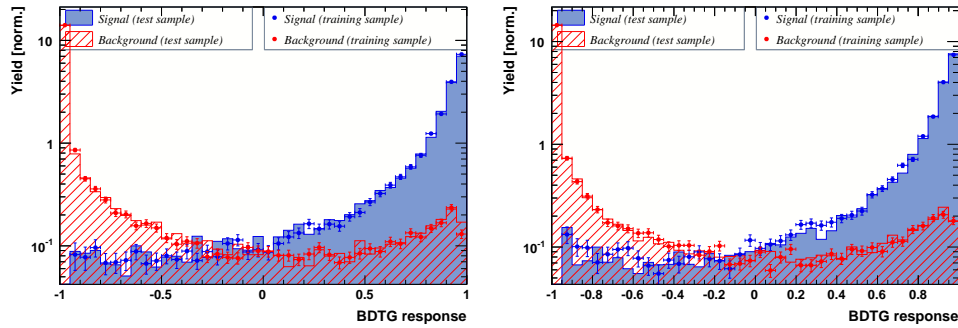


Figure A.7: Response of the classifier trained on the even and tested on the odd sample (left) and trained on the odd and tested on the even sample (right) for category [Run-II,L0-TOS].

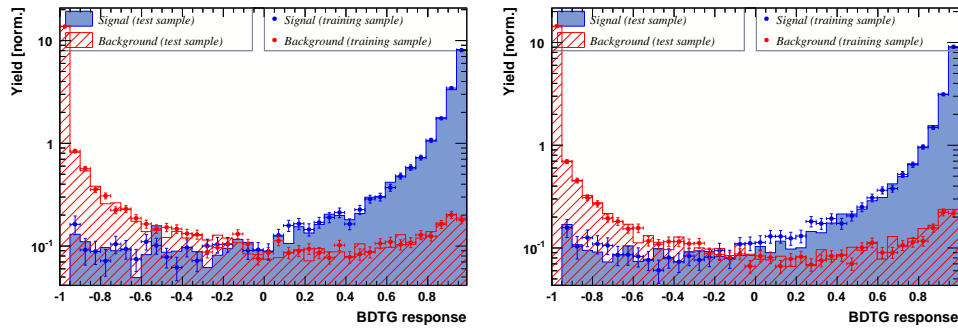


Figure A.8: Response of the classifier trained on the even and tested on the odd sample (left) and trained on the odd and tested on the even sample (right) for category [Run-II,L0-TIS].

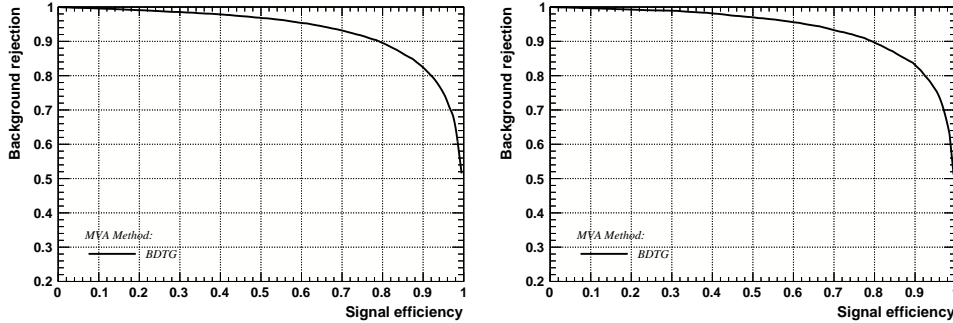


Figure A.9: Signal efficiency versus background rejection for the BDT trained on the even (left) and odd (right) sample for category [Run-I,L0-TOS].

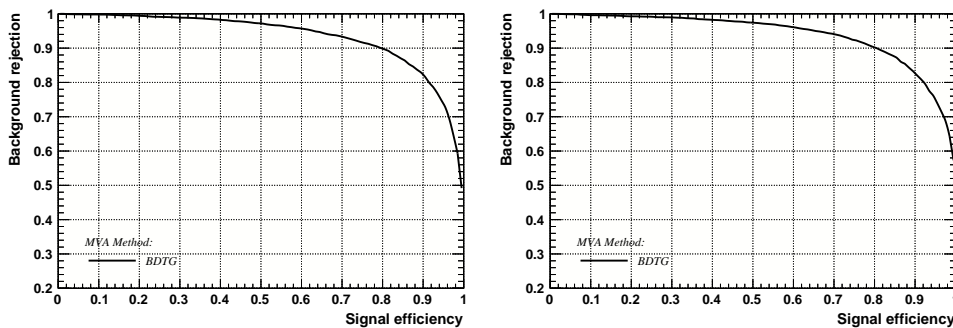


Figure A.10: Signal efficiency versus background rejection for the BDT trained on the even (left) and odd (right) sample for category [Run-I,L0-TIS].

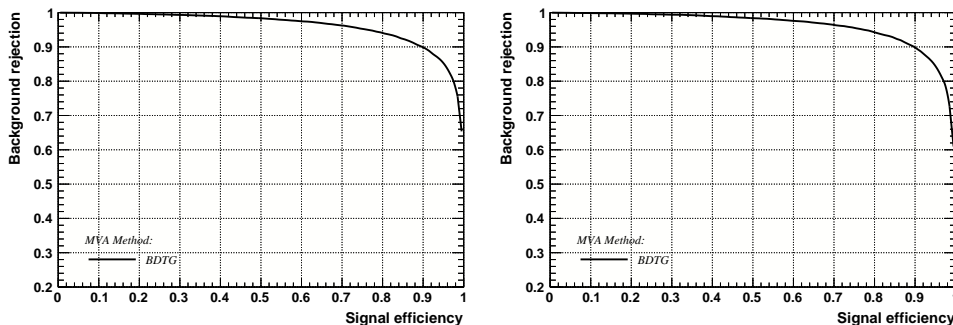


Figure A.11: Signal efficiency versus background rejection for the BDT trained on the even (left) and odd (right) sample for category [Run-II,L0-TOS].

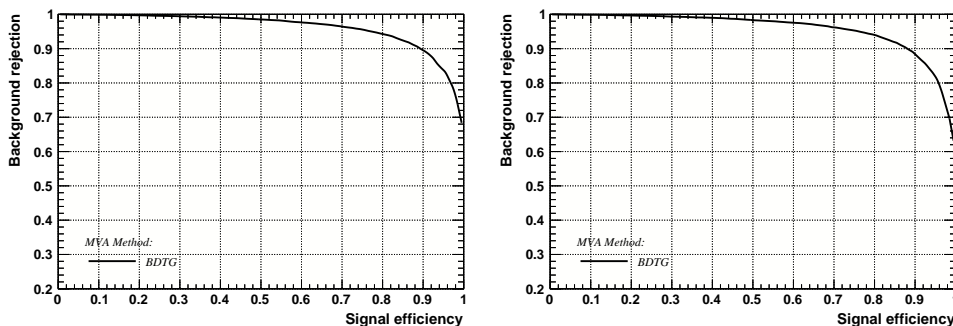


Figure A.12: Signal efficiency versus background rejection for the BDT trained on the even (left) and odd (right) sample for category [Run-II,L0-TIS].

1048 C Detailed mass fits

1049 In this section, all fits to the mass distribution of $B_s^0 \rightarrow D_s\pi\pi\pi$ and $B_s^0 \rightarrow D_sK\pi\pi$
 1050 candidates are shown. The fits are performed simultaneously in run period (Run-I, Run-
 1051 II), D_s final state ($D_s \rightarrow KK\pi$ non-resonant, $D_s \rightarrow \phi\pi$, $D_s \rightarrow K^*K$, or $D_s \rightarrow \pi\pi\pi$) and
 1052 L0 trigger category.

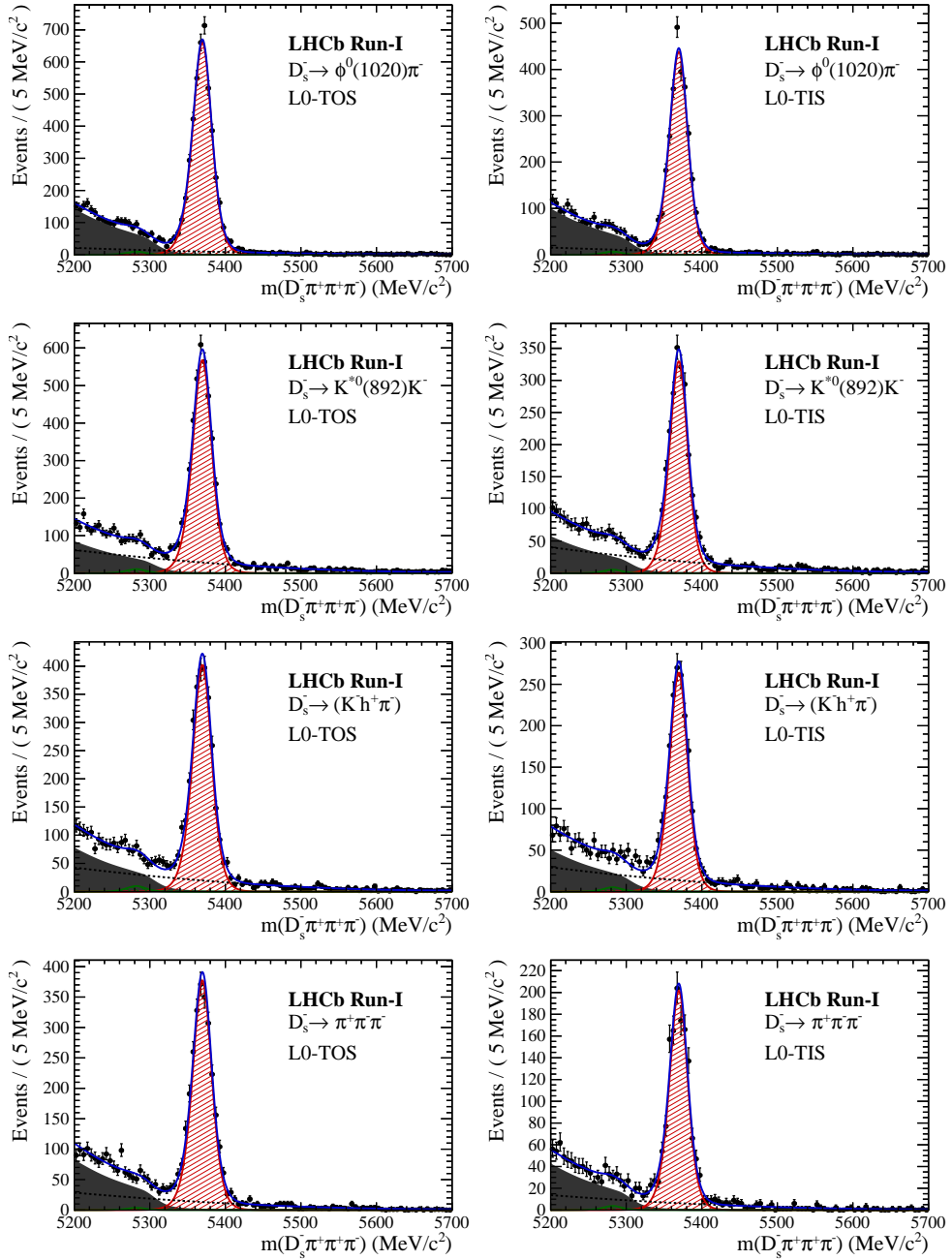


Figure B.1: Invariant mass distributions of $B_s^0 \rightarrow D_s\pi\pi\pi$ candidates for Run-I data.

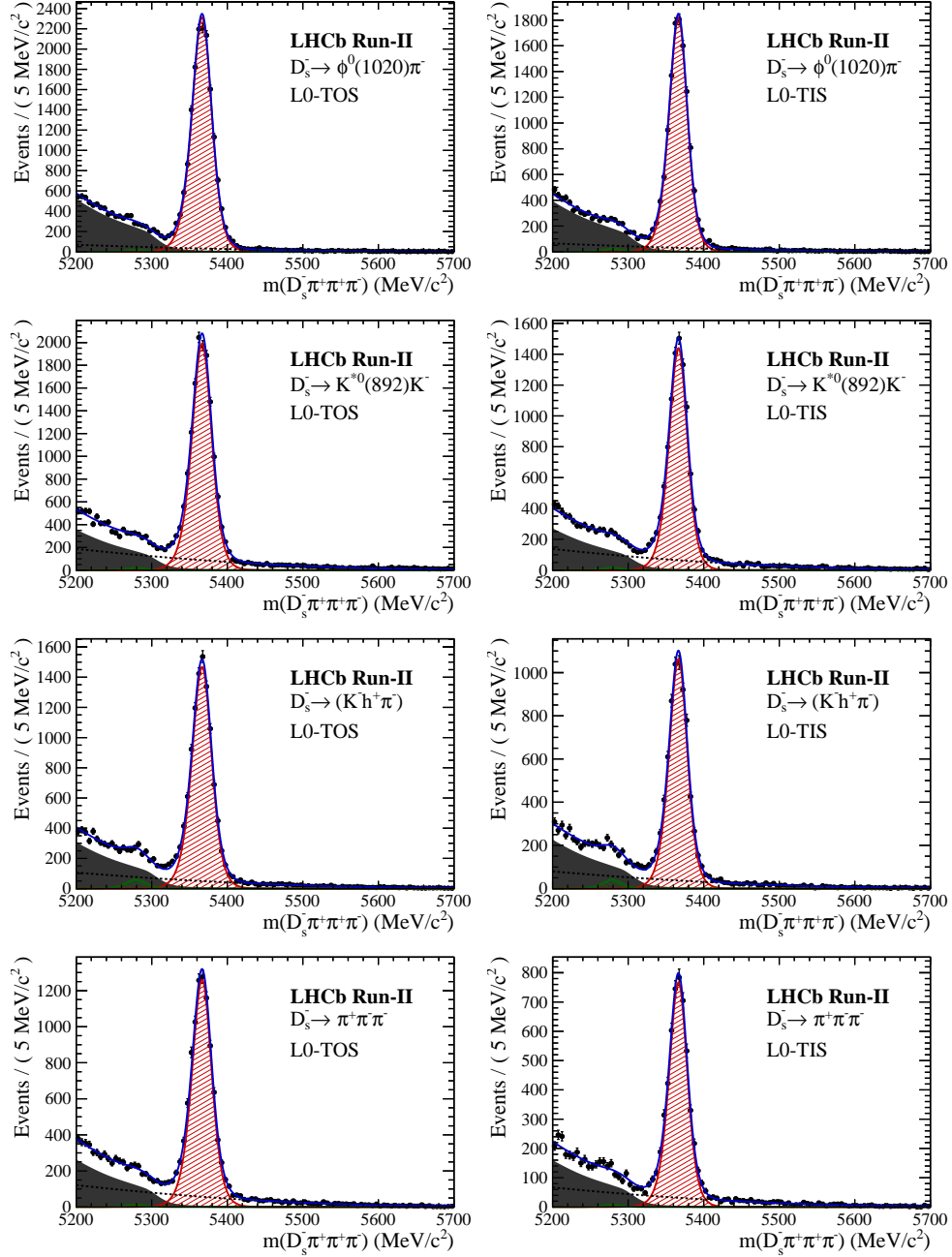


Figure B.2: Invariant mass distributions of $B_s^0 \rightarrow D_s\pi\pi\pi$ candidates for Run-II data.

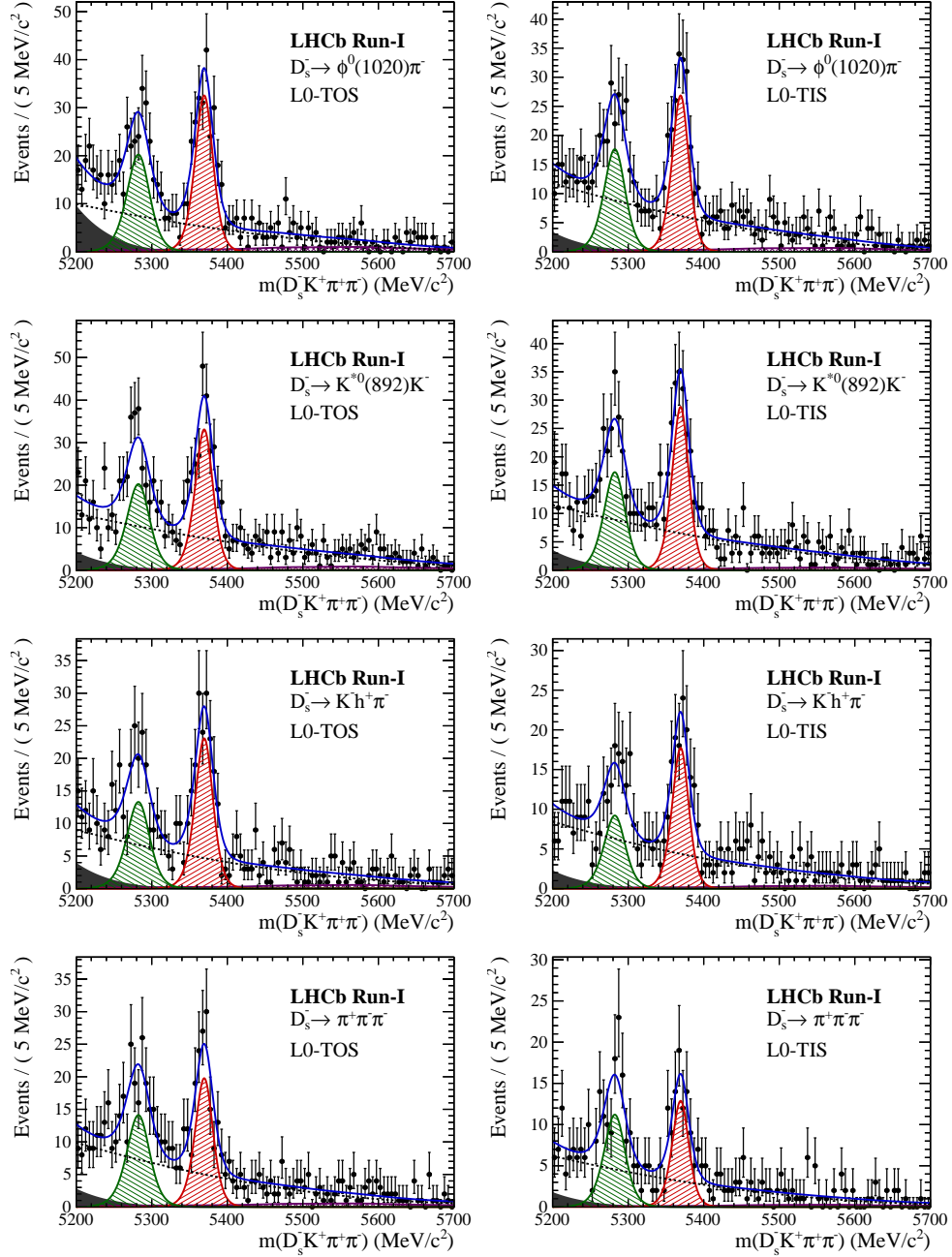


Figure B.3: Invariant mass distributions of $B_s^0 \rightarrow D_s K \pi \pi$ candidates for Run-I data.

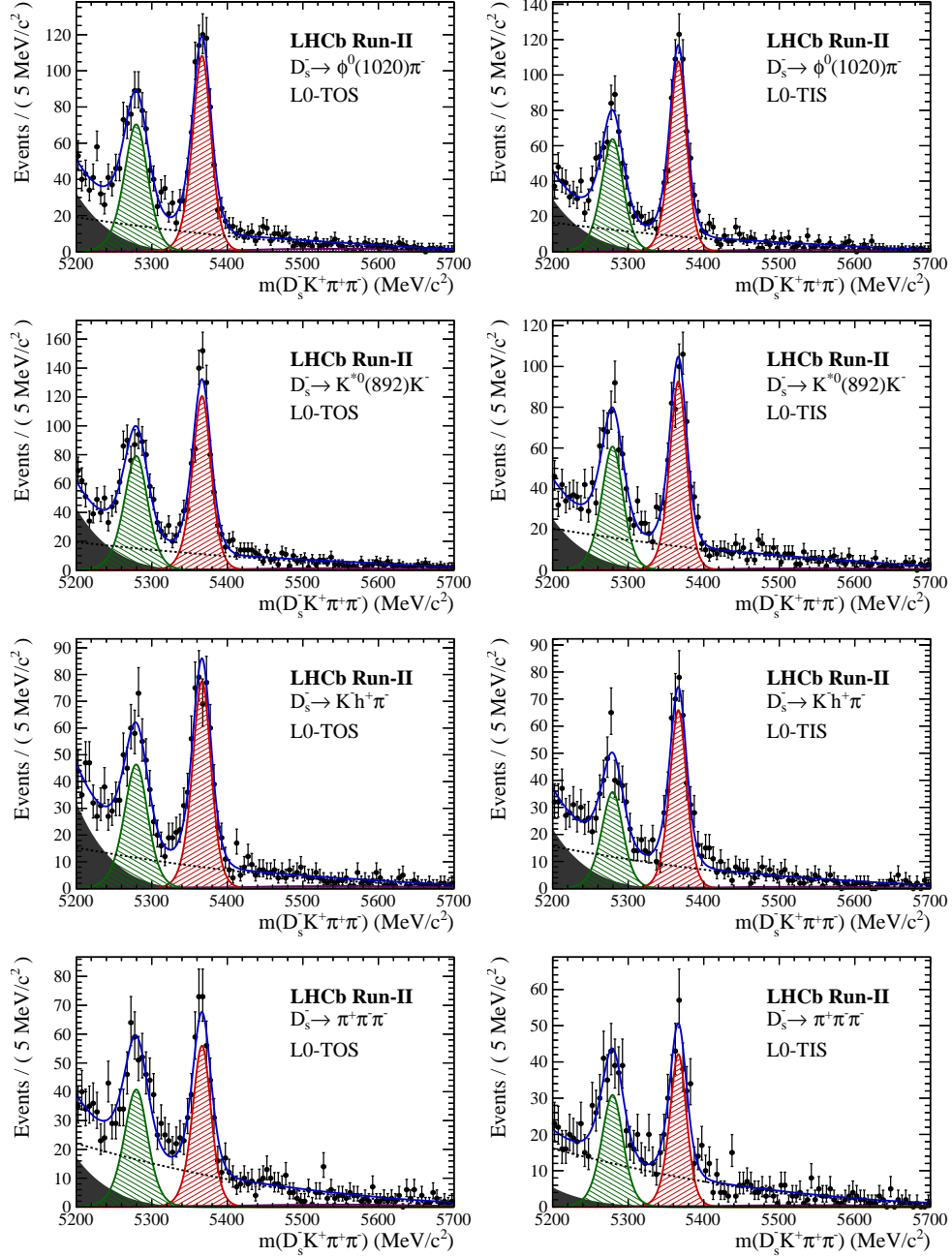


Figure B.4: Invariant mass distributions of $B_s^0 \rightarrow D_s K \pi \pi$ candidates for Run-II data.

1053 D Decay-time Resolution fits

1054 This section contains all fits to the distributions of the decay time difference Δt between
 1055 the true and the reconstructed decay time of the truth-matched B_s^0 candidates on MC.
 1056 The fits are performed in bins of the decay time error σ_t , where an adaptive binning
 1057 scheme is used to ensure that approximately the same number of events are found in each
 1058 bin.

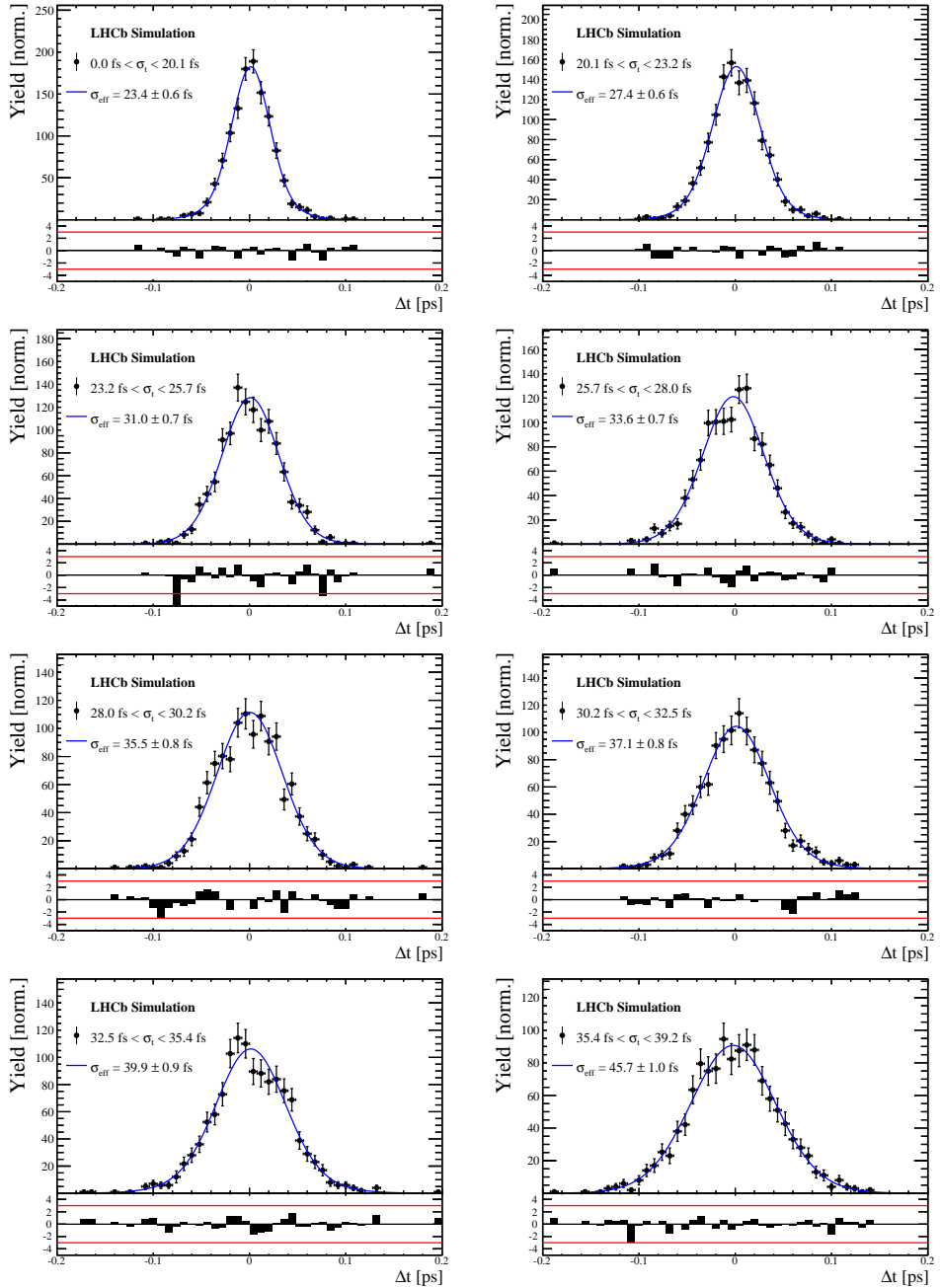


Figure C.1: Difference of the true and measured decay time of $B_s^0 \rightarrow D_s K \pi \pi$ MC candidates in bins of the per-event decay time error estimate..

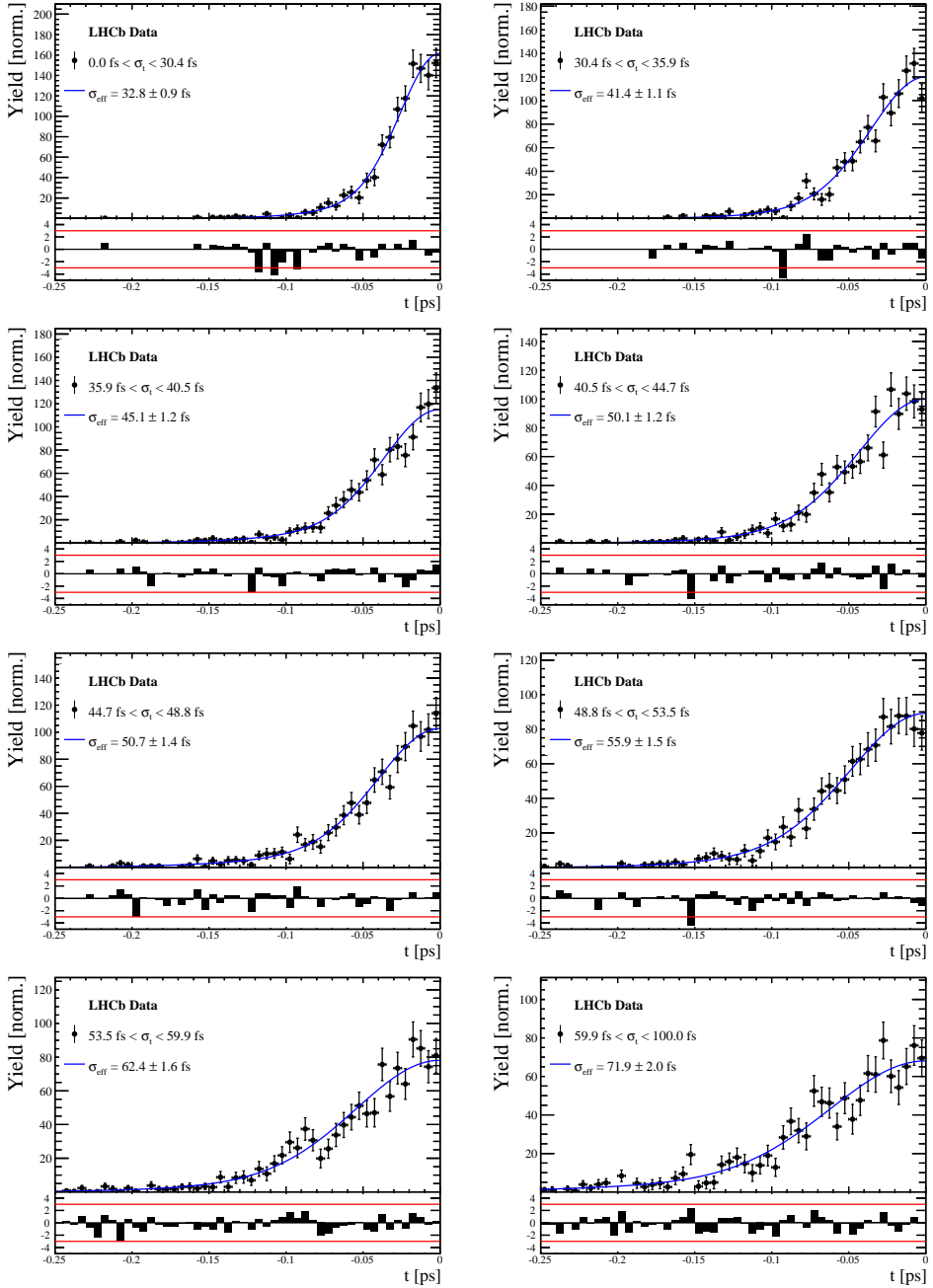


Figure C.2: Decay-time distribution for fake B_s candidates from promptly produced D_s candidates, combined with random prompt $K\pi\pi$ bachelor tracks, for bins in the per-event decay time error estimate.

σ_t Bin [fs]	σ_1 [fs]	σ_2 [fs]	f_1	D	σ_{eff} [fs]
0.0 - 20.1	19 ± 0.675	33.8 ± 1.77	0.75 ± 0	0.917 ± 0.00406	23.4 ± 0.599
20.1 - 23.2	23.4 ± 0.86	37.4 ± 1.95	0.75 ± 0	0.888 ± 0.00477	27.4 ± 0.621
23.2 - 25.7	28.1 ± 1.02	38.7 ± 2.32	0.75 ± 0	0.86 ± 0.00563	31 ± 0.671
25.7 - 28.0	30.1 ± 1.12	43.2 ± 2.56	0.75 ± 0	0.837 ± 0.00651	33.6 ± 0.734
28.0 - 30.2	32.4 ± 1.12	44.2 ± 2.59	0.75 ± 0	0.819 ± 0.00694	35.5 ± 0.756
30.2 - 32.5	32.6 ± 1.38	49.2 ± 3.04	0.75 ± 0	0.805 ± 0.00792	37.1 ± 0.841
32.5 - 35.4	34.4 ± 1.19	54.7 ± 2.85	0.75 ± 0	0.778 ± 0.0086	39.9 ± 0.879
35.4 - 39.2	41.9 ± 1.8	56.9 ± 4.18	0.75 ± 0	0.719 ± 0.00997	45.7 ± 0.962
39.2 - 44.7	42.2 ± 1.56	68.1 ± 4.01	0.75 ± 0	0.687 ± 0.0114	48.8 ± 1.08
44.7 - 120.0	55.5 ± 2.59	83 ± 14.7	0.75 ± 0	0.546 ± 0.0521	62 ± 4.89

Table 4.1: Measured time resolution for $B_s \rightarrow D_s K\pi\pi$ MC in bins of the per-event decay time error estimate.

σ_t Bin [fs]	σ_1 [fs]	σ_2 [fs]	f_1	D	σ_{eff} [fs]
0.0 - 30.4	25.4 ± 1.03	50.7 ± 2.77	0.75 ± 0	0.844 ± 0.00822	32.8 ± 0.942
30.4 - 35.9	34.5 ± 1.46	60.2 ± 3.48	0.75 ± 0	0.763 ± 0.0108	41.4 ± 1.08
35.9 - 40.5	35.6 ± 1.35	71.3 ± 3.84	0.75 ± 0	0.726 ± 0.0121	45.1 ± 1.18
40.5 - 44.7	42.3 ± 1.65	73.3 ± 4.21	0.75 ± 0	0.673 ± 0.0132	50.1 ± 1.24
44.7 - 48.8	39.6 ± 1.64	84.8 ± 5.07	0.75 ± 0	0.666 ± 0.0145	50.7 ± 1.36
48.8 - 53.5	47.6 ± 1.94	82.4 ± 5.48	0.75 ± 0	0.611 ± 0.0157	55.9 ± 1.46
53.5 - 59.9	53 ± 2.15	95.3 ± 6.84	0.75 ± 0	0.541 ± 0.0174	62.4 ± 1.63
59.9 - 100.0	60.5 ± 2.8	125 ± 14	0.75 ± 0	0.443 ± 0.0204	71.9 ± 2.03

Table 4.2: Measured time resolution for prompt- D_s data in bins of the per-event decay time error estimate.

1059 E Comparison of time-acceptance in subsamples

1060 Figure C.1 shows the spline coefficients obtained by fitting the decay-time distribution of
 1061 $B_s^0 \rightarrow D_s\pi\pi\pi$ data candidates in different subsamples. Sufficient agreement is observed
 1062 within a given data-taking period, while the acceptance shapes for Run-I and Run-II
 1063 data differ significantly. The fitted splines for the different D_s final states are in a good
 1064 agreement. The largest deviations are observed between the different L0 categories.

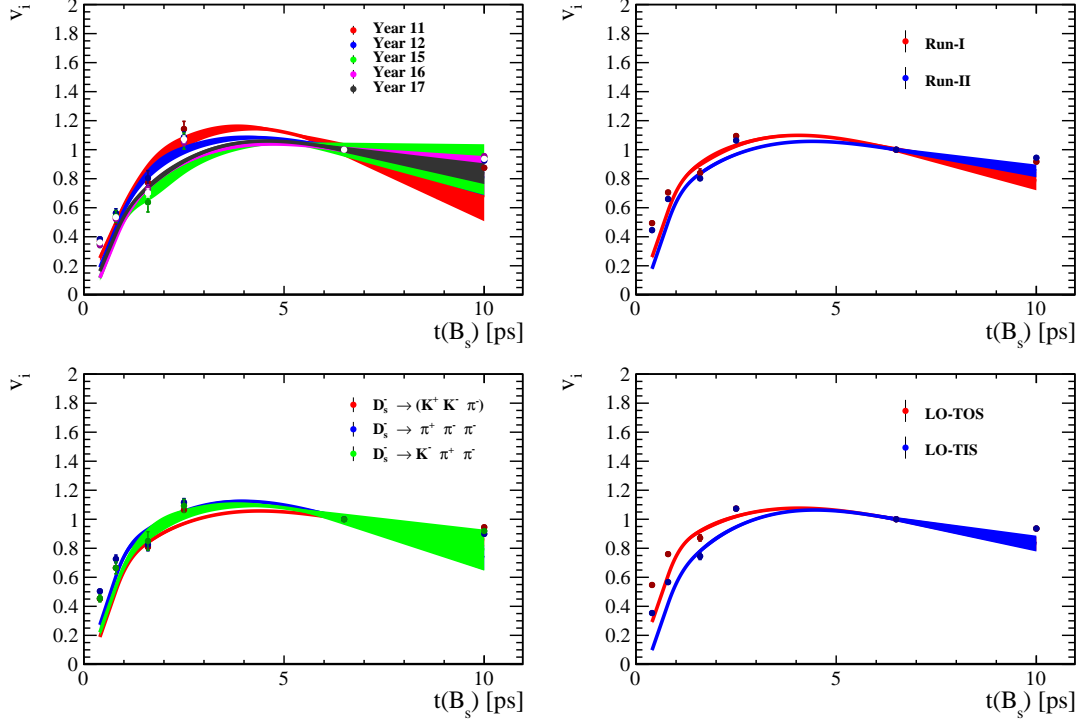


Figure C.1: Comparison of the spline coefficients (point with error bars) obtained from time-dependent fits to the $B_s^0 \rightarrow D_s\pi\pi\pi$ decay-time for different subsamples: (top-left) different years of data-taking; (top-right) different data-taking periods; (bottom-left) different D_s final states; (bottom-right) different trigger categories. The interpolated splines are overlaid.

1065 **F Spin Amplitudes**

1066 The spin factors used for $B \rightarrow P_1 P_2 P_3 P_4$ decays are given in Table 6.1.

Table 6.1: Spin factors for all topologies considered in this analysis. In the decay chains, S , P , V , A , T and PT stand for scalar, pseudoscalar, vector, axial vector, tensor and pseudotensor, respectively. If no angular momentum is specified, the lowest angular momentum state compatible with angular momentum conservation and, where appropriate, parity conservation, is used.

Number	Decay chain	Spin amplitude
1	$B \rightarrow (P P_1)$, $P \rightarrow (S P_2)$, $S \rightarrow (P_3 P_4)$	1
2	$B \rightarrow (P P_1)$, $P \rightarrow (V P_2)$, $V \rightarrow (P_3 P_4)$	$L_{(1)\alpha}(P) L_{(1)}^\alpha(V)$
3	$B \rightarrow (A P_1)$, $A \rightarrow (V P_2)$, $V \rightarrow (P_3 P_4)$	$L_{(1)\alpha}(B) P_{(1)}^{\alpha\beta}(A) L_{(1)\beta}(V)$
4	$B \rightarrow (A P_1)$, $A[D] \rightarrow (P_2 V)$, $V \rightarrow (P_3 P_4)$	$L_{(1)\alpha}(B) L_{(2)}^{\alpha\beta}(A) L_{(1)\beta}(V)$
5	$B \rightarrow (A P_1)$, $A \rightarrow (S P_2)$, $S \rightarrow (P_3 P_4)$	$L_{(1)\alpha}(B) L_{(1)}^\alpha(A)$
6	$B \rightarrow (A P_1)$, $A \rightarrow (T P_2)$, $T \rightarrow (P_3 P_4)$	$L_{(1)\alpha}(B) L_{(1)\beta}(A) L_{(2)}^{\alpha\beta}(T)$
7	$B \rightarrow (V_1 P_1)$, $V_1 \rightarrow (V_2 P_2)$, $V_2 \rightarrow (P_3 P_4)$	$L_{(1)\mu}(B) P_{(1)}^{\mu\alpha}(V_1) \epsilon_{\alpha\beta\gamma\delta} L_{(1)}^\beta(V_1) p_{V_1}^\gamma L_{(1)}^\delta(V_2)$
8	$B \rightarrow (PT P_1)$, $PT \rightarrow (V P_2)$, $V \rightarrow (P_3 P_4)$	$L_{(2)\alpha\beta}(B) P_{(2)}^{\alpha\beta\gamma\delta}(PT) L_{(1)\gamma}(PT) L_{(1)\delta}(V)$
9	$B \rightarrow (PT P_1)$, $PT \rightarrow (S P_2)$, $S \rightarrow (P_3 P_4)$	$L_{(2)\alpha\beta}(B) L_{(2)}(PT)^{\alpha\beta}$
10	$B \rightarrow (PT P_1)$, $PT \rightarrow (T P_2)$, $T \rightarrow (P_3 P_4)$	$L_{(2)\alpha\beta}(B) P_{(2)}^{\alpha\beta\gamma\delta}(PT) L_{(2)\gamma\delta}(T)$
11	$B \rightarrow (T P_1)$, $T \rightarrow (V P_2)$, $V \rightarrow (P_3 P_4)$	$L_{(2)\mu\nu}(B) P_{(2)}^{\mu\nu\rho\alpha}(T) \epsilon_{\alpha\beta\gamma\delta} L_{(2)\rho}^\beta(T) p_T^\gamma P_{(1)}^{\delta\sigma}(T) L_{(1)\sigma}(V)$
12	$B \rightarrow (T_1 P_1)$, $T_1 \rightarrow (T_2 P_2)$, $T_2 \rightarrow (P_3 P_4)$	$L_{(2)\mu\nu}(B) P_{(2)}^{\mu\nu\rho\alpha}(T_1) \epsilon_{\alpha\beta\gamma\delta} L_{(1)}^\beta(T_1) p_{T_1}^\gamma L_{(2)\rho}^\delta(T_2)$
13	$B \rightarrow (S_1 S_2)$, $S_1 \rightarrow (P_1 P_2)$, $S_2 \rightarrow (P_3 P_4)$	1
14	$B \rightarrow (V S)$, $V \rightarrow (P_1 P_2)$, $S \rightarrow (P_3 P_4)$	$L_{(1)\alpha}(B) L_{(1)}^\alpha(V)$
15	$B \rightarrow (V_1 V_2)$, $V_1 \rightarrow (P_1 P_2)$, $V_2 \rightarrow (P_3 P_4)$	$L_{(1)\alpha}(V_1) L_{(1)}^\alpha(V_2)$
16	$B[P] \rightarrow (V_1 V_2)$, $V_1 \rightarrow (P_1 P_2)$, $V_2 \rightarrow (P_3 P_4)$	$\epsilon_{\alpha\beta\gamma\delta} L_{(1)}^\alpha(B) L_{(1)}^\beta(V_1) L_{(1)}^\gamma(V_2) p_B^\delta$
17	$B[D] \rightarrow (V_1 V_2)$, $V_1 \rightarrow (P_1 P_2)$, $V_2 \rightarrow (P_3 P_4)$	$L_{(2)\alpha\beta}(B) L_{(1)}^\alpha(V_1) L_{(1)}^\beta(V_2)$
18	$B \rightarrow (T S)$, $T \rightarrow (P_1 P_2)$, $S \rightarrow (P_3 P_4)$	$L_{(2)\alpha\beta}(B) L_{(2)}^{\alpha\beta}(T)$
19	$B \rightarrow (V T)$, $T \rightarrow (P_1 P_2)$, $V \rightarrow (P_3 P_4)$	$L_{(1)\alpha}(B) L_{(2)}^{\alpha\beta}(T) L_{(1)\beta}(V)$
20	$B[D] \rightarrow (TV)$, $T \rightarrow (P_1 P_2)$, $V \rightarrow (P_3 P_4)$	$\epsilon_{\alpha\beta\delta\gamma} L_2^{\alpha\mu}(B) L_{2\mu}^\beta L_{(1)}^\gamma(V) p_B^\delta$
21	$B \rightarrow (T_1 T_2)$, $T_1 \rightarrow (P_1 P_2)$, $T_2 \rightarrow (P_3 P_4)$	$L_{(2)\alpha\beta}(T_1) L_{(2)}^{\alpha\beta}(T_2)$
22	$B[P] \rightarrow (T_1 T_2)$, $T_1 \rightarrow (P_1 P_2)$, $T_2 \rightarrow (P_3 P_4)$	$\epsilon_{\alpha\beta\gamma\delta} L_{(1)}^\alpha(B) L_{(2)}^{\beta\mu}(T_1) L_{(2)\mu}^\gamma(T_2) p_B^\delta$
23	$B[D] \rightarrow (T_1 T_2)$, $T_1 \rightarrow (P_1 P_2)$, $T_2 \rightarrow (P_3 P_4)$	$L_{(2)\alpha\beta}(B) L_{(2)}^{\alpha\gamma}(T_1) L_{(2)\gamma}^\beta(T_2)$

1067 G Considered Decay Chains

1068 The various decay channels considered in the model building are listed in Table 7.1.

Table 7.1: Decays considered in the LASSO model building.

Decay channel
$B_s \rightarrow D_s^- [K_1(1270)^+ [S, D] \rightarrow \pi^+ K^*(892)^0]$
$B_s \rightarrow D_s^- [K_1(1270)^+ \rightarrow \pi^+ K^*(1430)^0]$
$B_s \rightarrow D_s^- [K_1(1270)^+ [S, D] \rightarrow K^+ \rho(770)^0]$
$B_s \rightarrow D_s^- [K_1(1270)^+ [S, D] \rightarrow K^+ \omega(782)]$
$B_s \rightarrow D_s^- [K_1(1400)^+ [S, D] \rightarrow \pi^+ K^*(892)^0]$
$B_s \rightarrow D_s^- [K_1(1400)^+ [S, D] \rightarrow K^+ \rho(770)^0]$
$B_s \rightarrow D_s^- [K(1460)^+ \rightarrow \pi^+ \kappa]$
$B_s \rightarrow D_s^- [K(1460)^+ \rightarrow K^+ \sigma]$
$B_s \rightarrow D_s^- [K(1460)^+ \rightarrow \pi^+ K^*(892)^0]$
$B_s \rightarrow D_s^- [K(1460)^+ \rightarrow K^+ \rho(770)^0]$
$B_s \rightarrow D_s^- [K^*(1410)^+ \rightarrow \pi^+ K^*(892)^0]$
$B_s \rightarrow D_s^- [K^*(1410)^+ \rightarrow K^+ \rho(770)^0]$
$B_s \rightarrow D_s^- [K_2^*(1430)^+ \rightarrow \pi^+ K^*(892)^0]$
$B_s \rightarrow D_s^- [K_2^*(1430)^+ \rightarrow K^+ \rho(770)^0]$
$B_s \rightarrow D_s^- [K^*(1680)^+ \rightarrow \pi^+ K^*(892)^0]$
$B_s \rightarrow D_s^- [K^*(1680)^+ \rightarrow K^+ \rho(770)^0]$
$B_s \rightarrow D_s^- [K_2(1770)^+ \rightarrow \pi^+ K^*(892)^0]$
$B_s \rightarrow D_s^- [K_2(1770)^+ \rightarrow K^+ \rho(770)^0]$
$B_s \rightarrow \sigma^0(D_s^- K^+)_S$
$B_s [S, P, D] \rightarrow \sigma^0(D_s^- K^+)_V$
$B_s \rightarrow \rho(770)^0(D_s^- K^+)_S$
$B_s [S, P, D] \rightarrow \rho(770)^0(D_s^- K^+)_V$
$B_s \rightarrow K^*(892)^0(D_s^- \pi^+)_S$
$B_s [S, P, D] \rightarrow K^*(892)^0(D_s^- \pi^+)_V$
$B_s \rightarrow (D_s^- K^+)_S (\pi^+ \pi^-)_S$

H Data-simulation comparisson

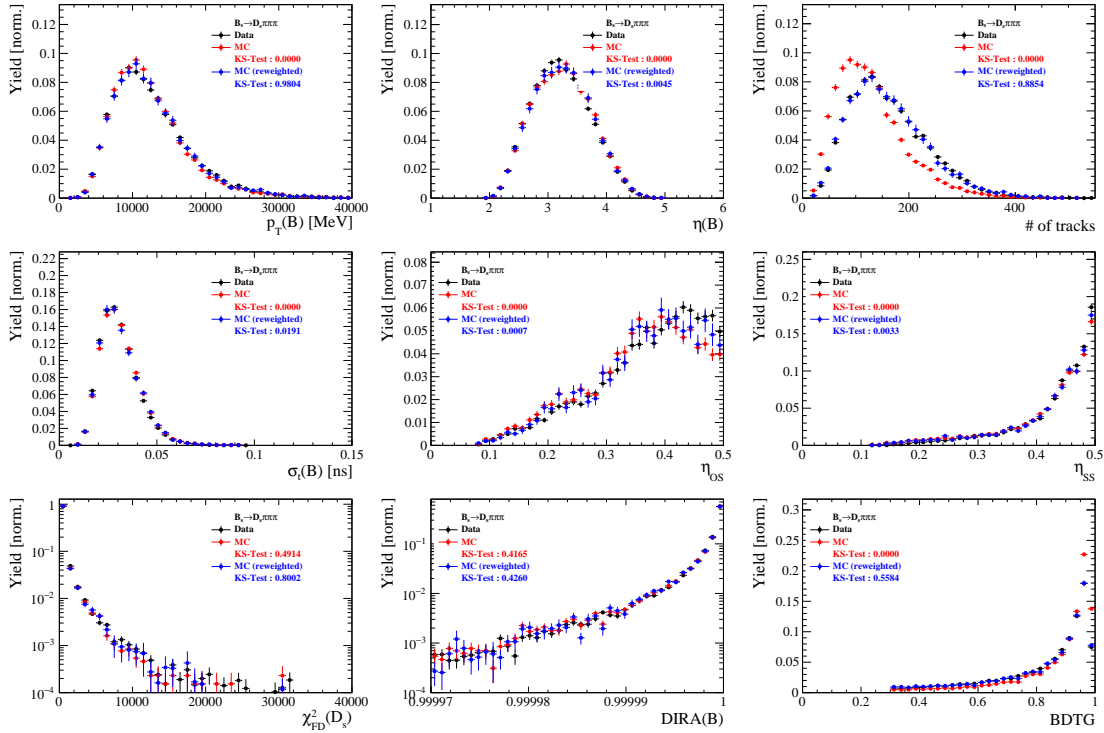


Figure C.1: Comparison between data and MC of selected variables for $B_s \rightarrow D_s \pi\pi\pi$ decays.

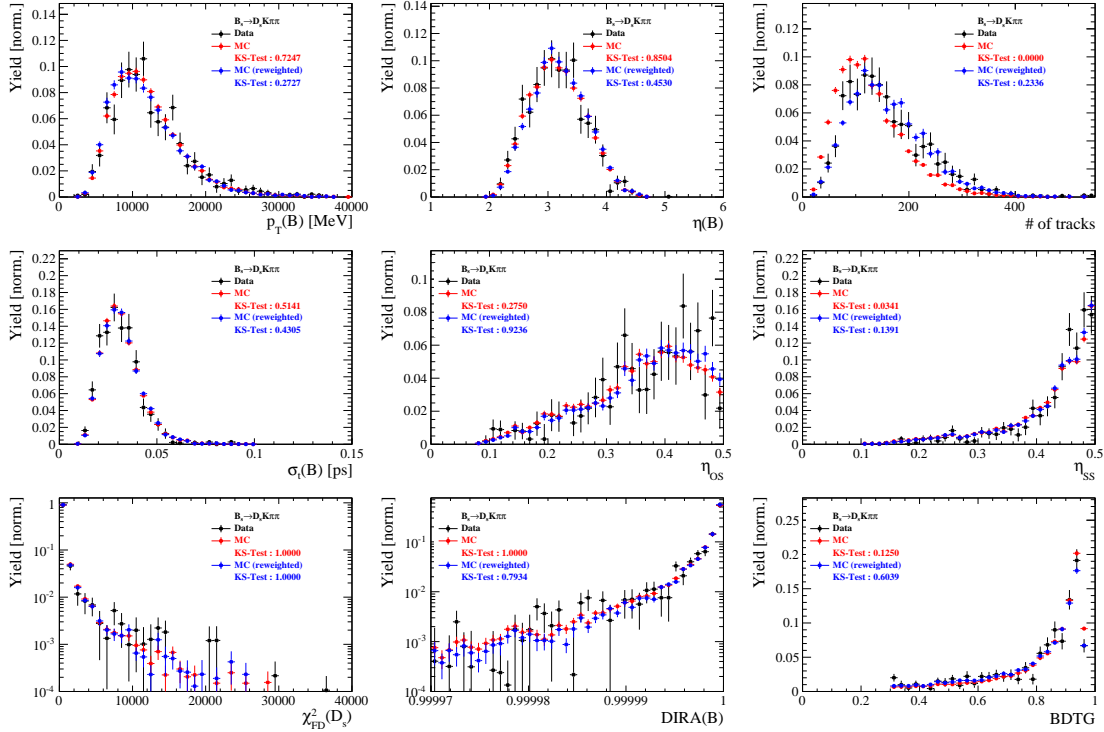


Figure C.2: Comparison between data and MC of selected variables for $B_s \rightarrow D_s K \pi\pi$ decays.

1070 I Data distributions

1071 I.1 Comparison of signal and calibration channels

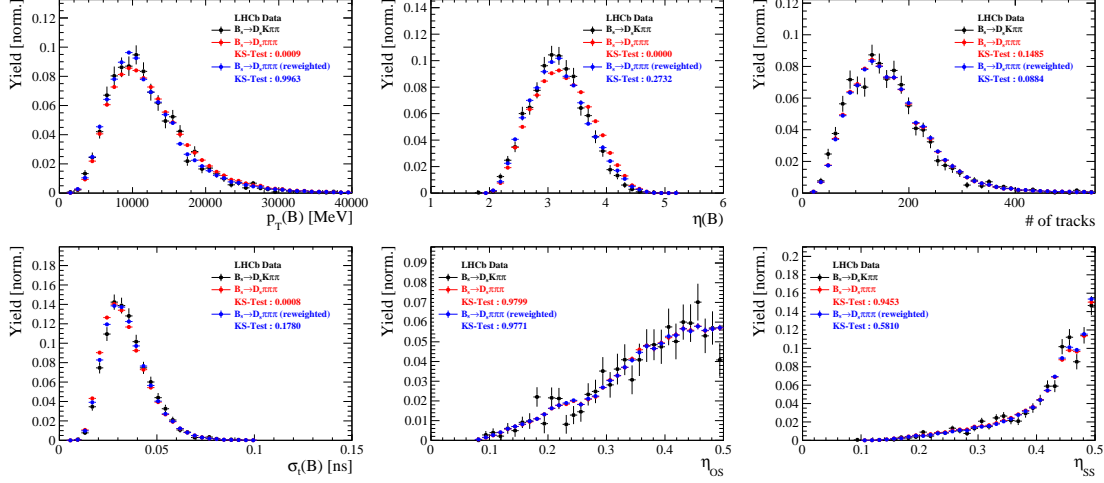


Figure C.1: Comparison between $B_s \rightarrow D_s K\pi\pi$ and $B_s \rightarrow D_s \pi\pi\pi$ decays for selected variables.

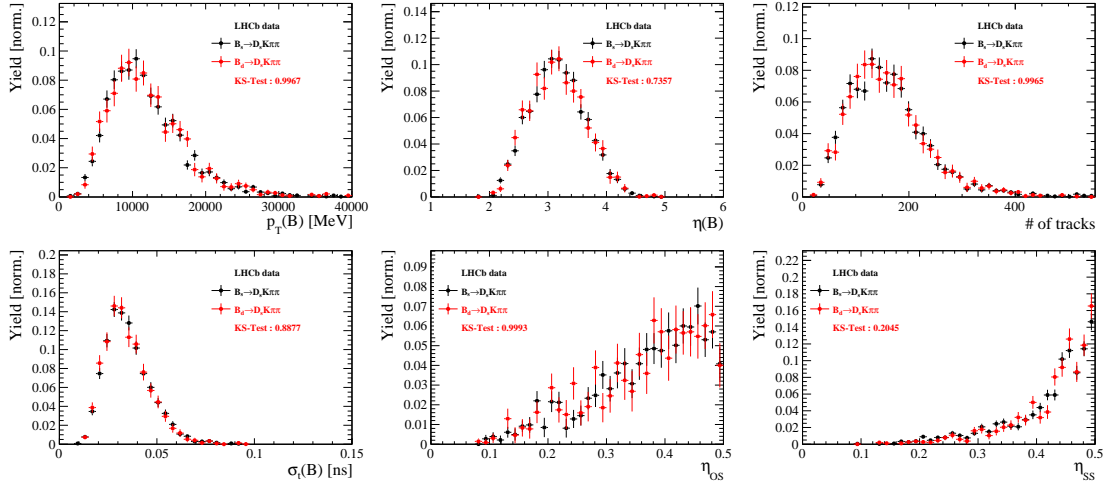


Figure C.2: Comparison between $B_s \rightarrow D_s K\pi\pi$ and $B_d \rightarrow D_s K\pi\pi$ decays for selected variables.

I.2 Comparison of data taken in 2016 and 2017

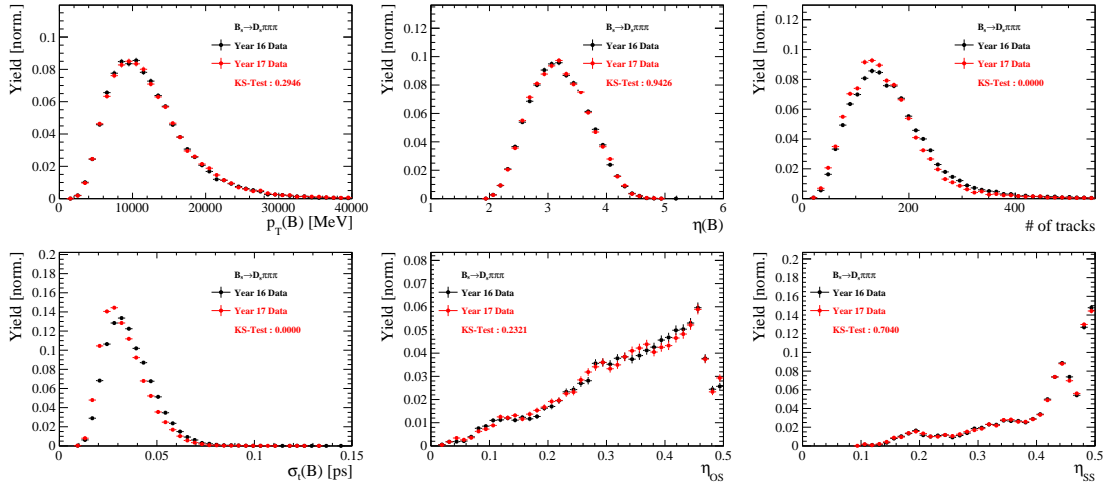


Figure C.3: Comparison of selected variables for $B_s \rightarrow D_s \pi\pi\pi$ data taken in 2016 and 2017.

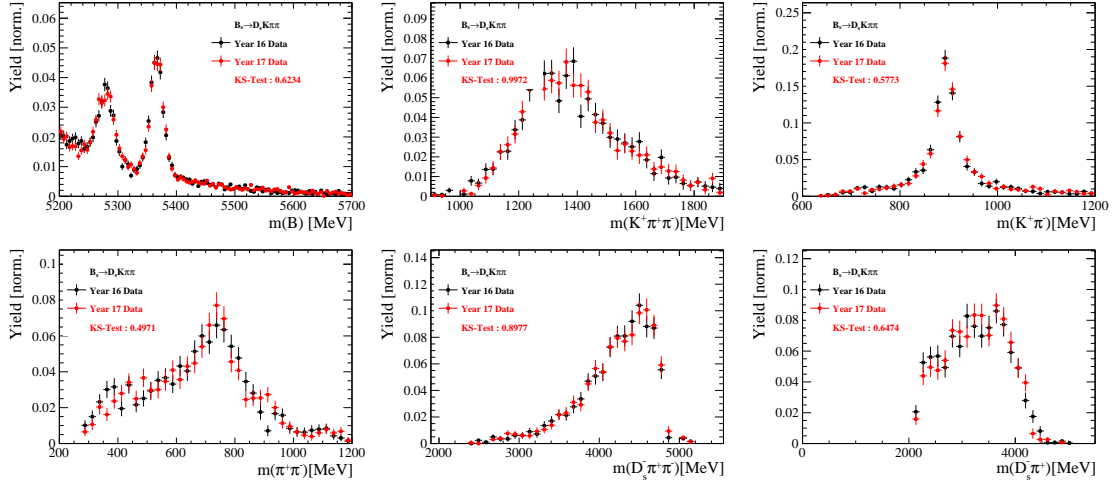


Figure C.4: Comparison of selected variables for $B_s \rightarrow D_s K\pi\pi$ data taken in 2016 and 2017.

1073 I.3 Comparison of Run-I and Run-II data

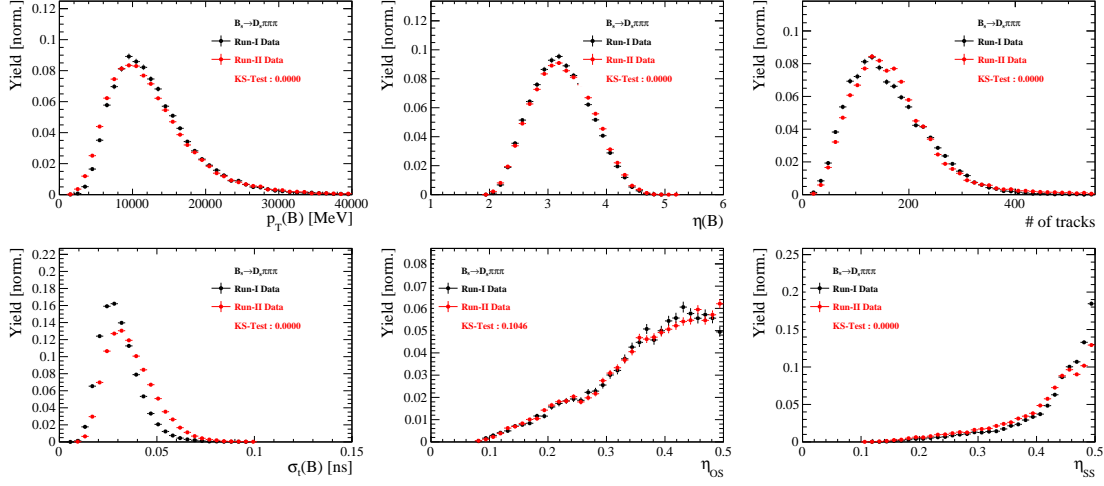


Figure C.5: Comparison of selected variables for Run-I and Run-II data.

1074 I.4 Comparison of D_s final states

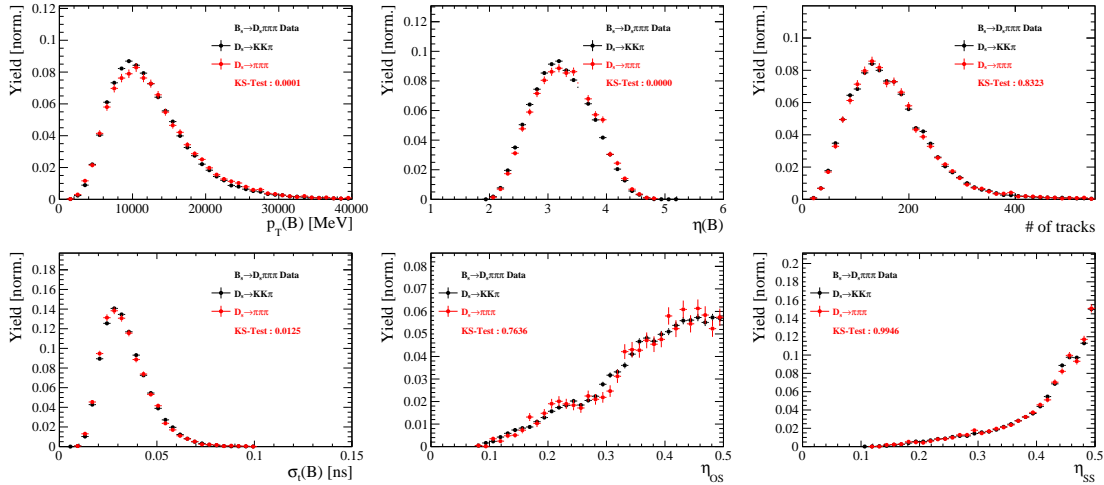


Figure C.6: Comparison of selected variables for different D_s final states.

1075 I.5 Comparison of trigger categories

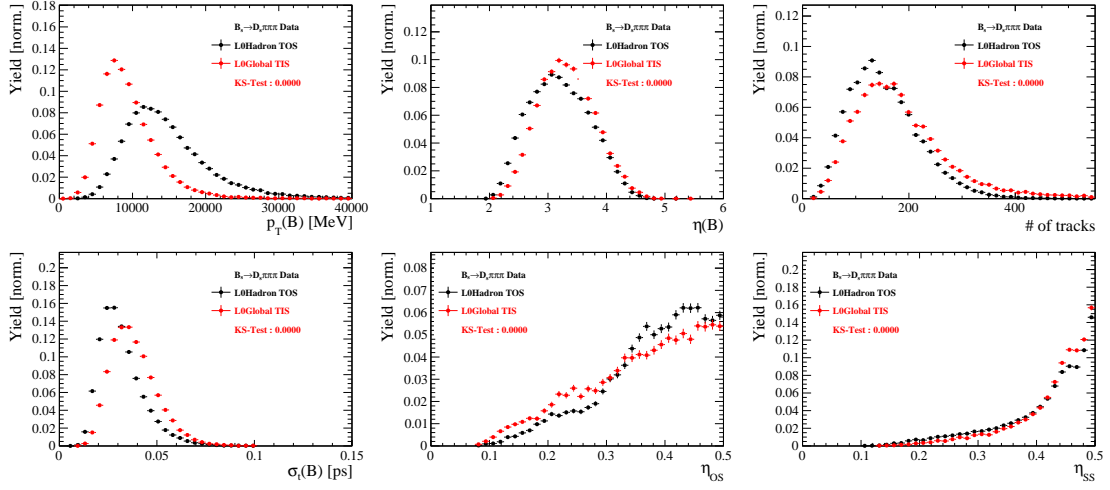


Figure C.7: Comparison of selected variables for different trigger categories.

1076 **References**

- 1077 [1] S. Blusk, *First observations and measurements of the branching fractions for the*
 1078 *decays $\bar{B}_s^0 \rightarrow D_s^+ K^- \pi^+ \pi^-$ and $\bar{B}^0 \rightarrow D_s^+ K^- \pi^+ \pi^-$,* .
- 1079 [2] LHCb, S. Blusk, *Measurement of the CP observables in $\bar{B}_s^0 \rightarrow D_s^+ K^-$ and first obser-*
 1080 *vation of $\bar{B}_{(s)}^0 \rightarrow D_s^+ K^- \pi^+ \pi^-$ and $\bar{B}_s^0 \rightarrow D_{s1}(2536)^+ \pi^-$,* 2012. [arXiv:1212.4180](#).
- 1081 [3] R. Fleischer, *New strategies to obtain insights into CP violation through $B_s \rightarrow$*
 1082 *$D_s^\pm K^\mp, D_s^{*\pm} K^\mp, \dots$ and $B_d \rightarrow D^\pm \pi^\mp, D^{*\pm} \pi^\mp, \dots$ decays,* Nucl. Phys. **B671** (2003) 459,
 1083 [arXiv:hep-ph/0304027](#).
- 1084 [4] K. De Bruyn *et al.*, *Exploring $B_s \rightarrow D_s^{(*)\pm} K^\mp$ Decays in the Presence of a Sizable*
 1085 *Width Difference $\Delta\Gamma_s$,* Nucl. Phys. **B868** (2013) 351, [arXiv:1208.6463](#).
- 1086 [5] E. Byckling and K. Kajantie, *Particle Kinematics*, John Wiley & Sons, 1973.
- 1087 [6] S. Mandelstam, J. E. Paton, R. F. Peierls, and A. Q. Sarker, *Isobar approximation*
 1088 *of production processes*, Annals of Physics **18** (1962), no. 2 198 .
- 1089 [7] D. J. Herndon, P. Söding, and R. J. Cashmore, *Generalized isobar model formalism*,
 1090 Phys. Rev. D **11** (1975) 3165.
- 1091 [8] J. J. Brehm, *Unitarity and the isobar model: Two-body discontinuities*, Annals of
 1092 Physics **108** (1977), no. 2 454 .
- 1093 [9] P. d'Argent *et al.*, *Amplitude Analyses of $D^0 \rightarrow \pi^+ \pi^- \pi^+ \pi^-$ and $D^0 \rightarrow K^+ K^- \pi^+ \pi^-$*
 1094 *Decays*, JHEP **05** (2017) 143, [arXiv:1703.08505](#).
- 1095 [10] F. von Hippel and C. Quigg, *Centrifugal-barrier effects in resonance partial decay*
 1096 *widths, shapes, and production amplitudes*, Phys. Rev. D **5** (1972) 624.
- 1097 [11] J. D. Jackson, *Remarks on the phenomenological analysis of resonances*, Il Nuovo
 1098 Cimento Series 10 **34** (1964), no. 6 1644.
- 1099 [12] Particle Data Group, C. Patrignani *et al.*, *Review of Particle Physics*, Chin. Phys.
 1100 **C40** (2016), no. 10 100001.
- 1101 [13] D. V. Bugg, *The mass of the σ pole*, Journal of Physics G Nuclear Physics **34** (2007)
 1102 151, [arXiv:hep-ph/0608081](#).
- 1103 [14] G. J. Gounaris and J. J. Sakurai, *Finite-width corrections to the vector-meson-*
 1104 *dominance prediction for $\rho \rightarrow e^+ e^-$* , Phys. Rev. Lett. **21** (1968) 244.
- 1105 [15] M. S. et al. *Search for CP violation in the $D^0 \rightarrow KK\pi\pi$ decay through a full*
 1106 *amplitude analysis*, LHCb-ANA-2017-064.
- 1107 [16] S. M. Flatté, *Coupled-channel analysis of the $\pi\eta$ and KK systems near KK threshold*,
 1108 Physics Letters B **63** (1976), no. 2 224 .
- 1109 [17] BES Collaboration, M. Ablikim *et al.*, *Resonances in $J/\psi \rightarrow \phi \pi^+ \pi^-$ and $\phi K^+ K^-$* ,
 1110 Phys. Lett. **B607** (2005) 243, [arXiv:hep-ex/0411001](#).

- [18] W. Dunwoodie, Fits to $K\pi$ $I = \frac{1}{2}$ S -wave amplitude and phase data.
- [19] D. Aston *et al.*, *A Study of $K^-\pi^+$ Scattering in the Reaction $K^-p \rightarrow K^-\pi^+n$ at $11\text{GeV}/c$* , Nucl. Phys. **B296** (1988) 493.
- [20] BaBar, B. Aubert *et al.*, *Dalitz-plot analysis of the decays $B^\pm \rightarrow K^\pm\pi^\mp\pi^\pm$* , Phys. Rev. **D72** (2005) 072003, arXiv:hep-ex/0507004, [Erratum: Phys. Rev.D74,099903(2006)].
- [21] LHCb, R. Aaij *et al.*, *Studies of the resonance structure in $D^0 \rightarrow K^\mp\pi^\pm\pi^\pm\pi^\mp$ decays*, Eur. Phys. J. **C78** (2018), no. 6 443, arXiv:1712.08609.
- [22] C. Zemach, *Use of angular momentum tensors*, Phys. Rev. **140** (1965) B97.
- [23] W. Rarita and J. Schwinger, *On a theory of particles with half integral spin*, Phys. Rev. **60** (1941) 61.
- [24] S. U. Chung, *General formulation of covariant helicity-coupling amplitudes*, Phys. Rev. D **57** (1998) 431.
- [25] B. S. Zou and D. V. Bugg, *Covariant tensor formalism for partial wave analyses of ψ decay to mesons*, Eur. Phys. J. **A16** (2003) 537, arXiv:hep-ph/0211457.
- [26] V. Filippini, A. Fontana, and A. Rotondi, *Covariant spin tensors in meson spectroscopy*, Phys. Rev. **D51** (1995) 2247.
- [27] J.-J. Zhu, *Explicit expressions of spin wave functions*, arXiv:hep-ph/9906250.
- [28] M. Williams, *Numerical Object Oriented Quantum Field Theory Calculations*, Comput. Phys. Commun. **180** (2009) 1847, arXiv:0805.2956.
- [29] D. J. Lange, *The EvtGen particle decay simulation package*, Nucl. Instrum. Meth. **A462** (2001) 152.
- [30] M. Karbach and M. Kenzie, *Gammacombo package*, <http://gammacombo.hepforge.org/web/HTML/index.html>, 2014.
- [31] A. Hoecker *et al.*, *TMVA: Toolkit for Multivariate Data Analysis*, PoS **ACAT** (2007) 040, arXiv:physics/0703039.
- [32] N. L. Johnson, *Systems of frequency curves generated by methods of translation*, Biometrika **36** (1949), no. 1/2 149.
- [33] Particle Data Group, K. A. Olive *et al.*, *Review of Particle Physics*, Chin. Phys. **C38** (2014) 090001.
- [34] LHCb collaboration, R. Aaij *et al.*, *LHCb detector performance*, Int. J. Mod. Phys. **A30** (2015) 1530022, arXiv:1412.6352.
- [35] LHCb, R. Aaij *et al.*, *Measurement of CP asymmetry in $B_s^0 \rightarrow D_s^\mp K^\pm$ decays*, Submitted to: JHEP (2017) arXiv:1712.07428.

- 1145 [36] LHCb collaboration, L. Zhang, *Measurements of CP violation in $B_s^0 \rightarrow J/\psi K^+ K^-$*
 1146 *decays in the low $K^+ K^-$ mass range with 13 TeV data*, LHCb-ANA-2017-028.
- 1147 [37] A. Poluektov, *Correction of simulated particle identification response in LHCb using*
 1148 *kernel density estimation*, LHCb-INT-2017-007.
- 1149 [38] Heavy Flavor Averaging Group, Y. Amhis *et al.*, *Averages of b-hadron, c-hadron, and*
 1150 *τ -lepton properties as of summer 2014*, arXiv:1412.7515, updated results and plots
 1151 available at <http://www.slac.stanford.edu/xorg/hfag/>.
- 1152 [39] T. M. Karbach, G. Raven, and M. Schiller, *Decay time integrals in neutral meson*
 1153 *mixing and their efficient evaluation*, arXiv:1407.0748.
- 1154 [40] LHCb Collaboration, R. Aaij *et al.*, *Measurement of angular and cp asymmetries*
 1155 *in $D^0 \rightarrow \pi^+ \pi^- \mu^+ \mu^-$ and $D^0 \rightarrow K^+ K^- \mu^+ \mu^-$ decays*, Phys. Rev. Lett. **121** (2018)
 1156 091801.
- 1157 [41] LHCb collaboration, R. Aaij *et al.*, *Opposite-side flavour tagging of B mesons at the*
 1158 *LHCb experiment*, Eur. Phys. J. **C72** (2012) 2022, arXiv:1202.4979.
- 1159 [42] LHCb, R. Aaij *et al.*, *A new algorithm for identifying the flavour of B_s^0 mesons at*
 1160 *LHCb*, JINST **11** (2016), no. 05 P05010, arXiv:1602.07252.
- 1161 [43] LHCb, R. Aaij *et al.*, *Measurement of B^0 , B_s^0 , B^+ and Λ_b^0 production asymmetries in 7*
 1162 *and 8 TeV proton-proton collisions*, Phys. Lett. **B774** (2017) 139, arXiv:1703.08464.
- 1163 [44] H. Gordon, R. W. Lambert, J. van Tilburg, and M. Vesterinen, *A Measurement of*
 1164 *the $K\pi$ Detection Asymmetry*, Tech. Rep. LHCb-INT-2012-027. CERN-LHCb-INT-
 1165 2012-027, CERN, Geneva, Feb, 2013.
- 1166 [45] A. Davis *et al.*, *Measurement of the instrumental asymmetry for $K^- \pi^+$ -pairs at LHCb*
 1167 *in Run 2*, Tech. Rep. LHCb-PUB-2018-004. CERN-LHCb-PUB-2018-004, CERN,
 1168 Geneva, Mar, 2018.
- 1169 [46] I. I. Y. Bigi and H. Yamamoto, *Interference between Cabibbo allowed and doubly*
 1170 *forbidden transitions in $D \rightarrow K(S)$, $K(L) + \pi$'s decays*, Phys. Lett. **B349** (1995)
 1171 363, arXiv:hep-ph/9502238.
- 1172 [47] M. Pivk and F. R. Le Diberder, *sPlot: A statistical tool to unfold data distributions*,
 1173 Nucl. Instrum. Meth. **A555** (2005) 356, arXiv:physics/0402083.
- 1174 [48] R. Tibshirani, *Regression shrinkage and selection via the Lasso*, Journal of the Royal
 1175 Statistical Society, Series B **58** (1994) 267.
- 1176 [49] B. Guegan, J. Hardin, J. Stevens, and M. Williams, *Model selection for amplitude*
 1177 *analysis*, JINST **10** (2015), no. 09 P09002, arXiv:1505.05133.
- 1178 [50] G. Schwarz, *Estimating the dimension of a model*, Ann. Statist. **6** (1978) 461.
- 1179 [51] CLEO Collaboration, M. Artuso *et al.*, *Amplitude analysis of $D^0 \rightarrow K^+ K^- \pi^+ \pi^-$* ,
 1180 Phys. Rev. **D85** (2012) 122002, arXiv:1201.5716.

- 1181 [52] T. Skwarnicki, *A study of the radiative cascade transitions between the Upsilon-prime*
 1182 *and Upsilon resonances*, PhD thesis, Institute of Nuclear Physics, Krakow, 1986,
 1183 DESY-F31-86-02.
- 1184 [53] D. Hill, M. John, and P. Gandini, *A study of partially reconstructed $B^\pm \rightarrow D^{*0} h^\pm$*
 1185 *decays using the $D^0 \rightarrow K\pi, KK, \pi\pi$ final states*, .
- 1186 [54] G. H. Golub and C. F. Van Loan, *Matrix Computations (3rd Ed.)*, Johns Hopkins
 1187 University Press, Baltimore, MD, USA, 1996.
- 1188 [55] L. collaboration, *Precision measurement of the B_s oscillation frequency with the decay*
 1189 $B_s \rightarrow D_s\pi$, LHCb-ANA-2012-053.
- 1190 [56] BaBar, P. del Amo Sanchez *et al.*, *Measurement of $D0$ -anti $D0$ mixing parameters*
 1191 *using $D0 \rightarrow K(S)0 \pi^+ \pi^-$ and $D0 \rightarrow K(S)0 K^+ K^-$ decays*, Phys. Rev. Lett. **105**
 1192 (2010) 081803, [arXiv:1004.5053](https://arxiv.org/abs/1004.5053).
- 1193 [57] LHCb, R. Aaij *et al.*, *Studies of the resonance structure in $D^0 \rightarrow K_S^0 K^\pm \pi^\mp$ decays*,
 1194 Phys. Rev. **D93** (2016), no. 5 052018, [arXiv:1509.06628](https://arxiv.org/abs/1509.06628).